Thermodynamics and experimental investigation of the internal oxidation of Fe-Cr-Al-(Y) alloys

Zur Erlangung des akademischen Grades eines

DOKTORS DER INGENIEURWISSENSCHAFTEN (Dr.-Ing.)

von der KIT-Fakultät für Maschinenbau des

Karlsruher Instituts für Technologie (KIT)

angenommene

DISSERTATION

von

M.Sc. (with Honours) Seyedhossein Miran

Tag der mündlichen Prüfung:	20.12.2023
Hauptreferent:	Prof. Dr. Martin Heilmaier
Korreferentin:	Prof. Dr. Bronislava Gorr

This document is licensed under a Creative Commons

Attribution-NonCommercial-NoDerivatives 4.0 International License (CC BY-NC-ND 4.0):
https://creativecommons.org/licenses/by-nc-nd/4.0/deed.en

To my dear wife and daughter

تقدیم به همسر و فرزندم

Acknowledgement

I extend my profound appreciation to Mr. Prof. Dr. Heilmaier for his meticulous revision and thorough evaluation of the dissertation. I am sincerely grateful to Ms. Prof. Dr. Gorr for her insightful assessment of the work as the second reviewer. A special acknowledgment goes to Mr. Prof. Dr. Maas, who served as the head of the examination committee, for his invaluable contributions. Mr. Prof. Dr. Seifert is appreciated for the scientific supervision of this project. Special thanks to Mr. Dr. Franke for his cooperation and valuable discussions in this work. His extensive knowledge in thermodynamic and kinetic modelling helped me to find the right orientation for this work.

I gratefully also acknowledge Mr. Prof. Dr. Möslang for the guidance in the field of ODS steels and Mr. Dr. Hoffmann for his assistance in TEM photos and EBSD analysis, and Mr. Dr. Rieth for the collaboration in mechanical testing and the discussions in this part. Furthermore, I would like to thank Mr. Dr. Bergfeldt and the analytical chemistry group for the ICP measurements and Ms. Stegmaier and Ms. Severloh for their assistance in metallographic preparation and SEM analysis of the samples. Mr. Besser in Laser group is appreciated for the preparation of tensile specimens.

The financial support by the German Helmholtz Association in the frame of LIMTECH Alliance and holding several Ph.D. workshops in Karlsruhe, Dresden, Hannover, Illmenau and Freiberg is highly regarded. All the assistance of my colleagues in the institute for applied materials – applied materials physics (IAM - AWP), especially thermophysics and thermodynamics group at Karlsruhe Institute of Technology (KIT) are kindly recognized.

Lastly, I would like to deeply thank my parents for their sincere support throughout my entire life. My lovely thanks to my wife and daughter, Bahar and Delnavaz, for their heartily encouragement in all challenging times.

Karlsruhe, 2023

S. Miran

Abstract

Reduced activation ferritic-martensitic (RAFM) steels are named as one of the primary candidates for structural materials in fusion reactors. Low creep and fatigue resistance of RAFM steels limit the usability of these alloys for this purpose, and massive international research is ongoing to overcome this issue and develop Oxide Dispersion Strengthened (ODS) steels. This type of steels is being developed as advanced materials for fusion and other elevated temperature applications.

The production of ODS steels is typically carried out using a powder metallurgy route, which involves mechanical alloying, hot isostatic pressing, hot extrusion or rolling, and subsequent heat treatment steps. This route is commonly regarded as the primary manufacturing method for ODS steels, but it is also considered a costly and complex process. An intriguing alternative for producing ODS alloys would be internal oxidation, which has the potential to make the production process less complex and more cost-effective.

In this study, the internal oxidation of Fe-Cr-Al-(Y) alloys was investigated to assess the feasibility of the selective oxidation of Al-(Y) in Cr-steels. The first step of this work involved the study of the oxidation behavior of Fe as the base component, Cr as an alloying element, Al and/or Y as oxide-forming elements. Thermodynamic and diffusion calculations were performed using Thermo-Calc and DICTRA software in the iron-rich side of the phase diagram. Due to the requirement of extremely low oxygen activity for internal oxidation in this system, several oxygen buffer systems were considered, including Cr/Cr_2O_3, Fe/FeO, V_2O/VO, and VO/V_2O_3 equilibrium mixtures.

The later oxidation experiments using VO/V_2O_3 powder mixture with direct contact with the alloys and the buffer system resulted in the successful formation of an internal oxidation zone (IOZ) with approximately 2000 µm of depth, consisting of Al-O based particles, in Fe-16Cr-0.2Al alloys. The same experiment with VO/V_2O_3 for Fe-16Cr-0.2Al-0.05Y alloy also showed an IOZ with a similar depth of approximately 2000 µm.

To evaluate the tensile strength of the produced alloys, mechanical testing was carried out on internally oxidized samples of Fe-16Cr-0.2Al and Fe-16Cr-0.2Al-0.05Y alloys. The highest recorded tensile strengths for these alloys were approximately 205 MPa.

The achieved ultimate tensile strength (UTS) values in this study were about 17% to 31% of the typical UTS values for conventional ODS steels at room temperature. It should be noted that the minimum size of oxides observed in this study was approximately 600 nm, whereas the reported size of oxide particles in conventional ODS steels was much finer, typically less than 100 nm. Another aspect that should be considered is the absence of additional alloying elements such as Ni, W and Ti in the studied alloys in this work. Taking these two points into account (size of oxide particles and lack of additional alloying elements), the deviation in the mechanical properties of the produced alloys compared to conventional ODS steels could be explained. This study leads to the conclusion that the selective oxidation of Al-(Y) in the examined Cr-steels is indeed viable, and internal oxidation might be considered as an alternative production route for ODS steels.

Kurzfassung

Reduced activation ferritic-martensitic (RAFM) Stähle werden als eine der Hauptkandidaten für Strukturwerkstoffe in Fusionsreaktoren bezeichnet. Die geringe Kriech- und Ermüdungsbeständigkeit von RAFM-Stählen begrenzt jedoch die Verwendbarkeit dieser Legierungen für diesen Zweck. Daher läuft eine umfangreiche internationale Forschung, um dieses Problem zu überwinden und Oxid-Dispersion-verfestigte (ODS) Stähle zu entwickeln. Diese Art von Stählen wird als fortgeschrittenes Material für Fusion und andere Anwendungen bei erhöhten Temperaturen entwickelt.

ODS-Stähle werden in der Regel durch den Einsatz der Pulvermetallurgie-Methode hergestellt, die verschiedene Schritte wie mechanisches Legieren, Heiß-Isostatisches Pressen, heißes Extrudieren oder Walzen sowie anschließende Wärmebehandlung umfasst. Dieser Weg gilt allgemein als die Hauptmethode zur Herstellung von ODS-Stählen, ist jedoch auch als kostenintensiv und komplex anzusehen. Eine interessante Alternative zur Herstellung von ODS-Legierungen wäre die innere Oxidation, die das Herstellungsverfahren weniger komplex und kosteneffektiver gestalten könnte.

In dieser Studie wurde die innere Oxidation von Fe-Cr-Al-(Y)-Legierungen untersucht, um die Durchführbarkeit der selektiven Oxidation von Al-(Y) in Cr-Stählen zu bewerten. Der erste Schritt dieser Arbeit bestand darin, das Oxidationsverhalten von Fe als Basiskomponente, Cr als Legierungselement sowie Al und/oder Y als oxidbildende Elemente zu untersuchen. Thermodynamische und diffusionskinetische Berechnungen wurden unter Verwendung der Software Thermo-Calc und DICTRA auf der eisenreichen Seite des Phasendiagramms durchgeführt. Aufgrund der Anforderung äußerst niedriger Sauerstoffaktivität für die innere Oxidation in diesem System wurden mehrere Sauerstoffpuffer-Systeme in Betracht gezogen, darunter Cr/Cr_2O_3, Fe/FeO, V_2O/VO, and VO/V_2O_3 Gleichgewichtsmischungen.

Die späteren Oxidationsversuche unter Verwendung einer VO/V_2O_3-Pulvermischung mit direktem Kontakt zu den Legierungen und dem Puffersystem führten zur erfolgreichen Bildung einer inneren Oxidationszone (IOZ) mit einer Tiefe von etwa 2000 µm in Fe-16Cr-0.2Al Legierungen. Diese Zone bestand aus Al-O-basierten Partikeln. Das gleiche

Experiment mit VO/V_2O_3 für die Fe-16Cr-0.2Al-0.05Y Legierung zeigte ebenfalls eine IOZ mit einer ähnlichen Tiefe von etwa 2000 µm.

Um die Zugfestigkeit der hergestellten Legierungen zu bewerten, wurden mechanische Tests an inneroxidierten Proben der Fe-16Cr-0.2Al- und Fe-16Cr-0.2Al-0.05Y-Legierungen durchgeführt. Die höchsten gemessenen Zugfestigkeiten für diese Legierungen betrugen etwa 205 MPa. Die erzielten Werte für die Zugfestigkeit (Ultimate Tensile Strength, UTS) in dieser Studie entsprachen etwa 17% bis 31% der typischen UTS-Werte für konventionelle ODS-Stähle bei Raumtemperatur. Es sollte beachtet werden, dass die minimale Größe der beobachteten Oxide in dieser Studie etwa 600 nm betrug, während die berichtete Größe der Oxidpartikel in konventionellen ODS-Stählen wesentlich feiner war, typischerweise weniger als 100 nm. Ein weiterer Aspekt, der berücksichtigt werden sollte, ist das Fehlen zusätzlicher Legierungselemente wie Ni, W und Ti in den untersuchten Legierungen in dieser Arbeit. Unter Berücksichtigung dieser beiden Punkte (Größe der Oxidpartikel und Fehlen zusätzlicher Legierungselemente) lässt sich die Abweichung der mechanischen Eigenschaften der hergestellten Legierungen im Vergleich zu konventionellen ODS-Stählen erklären. Daher lässt sich nach Abschluss dieser Studie feststellen, dass die selektive Oxidation von Al-(Y) in den untersuchten Cr-Stählen möglich ist und die innere Oxidation als alternative Herstellungsmethode für ODS-Stähle betrachtet werden könnte.

Table of Contents

Acknowledgement ..... **IV**
Abstract ..... **V**
Kurzfassung ..... **VII**
List of Figures ..... **XII**
List of Tables ..... **XX**
Chapter 1. Introduction **1**
1.1 Fusion reactors 1
1.2 Materials selection for fusion reactors 3
1.3 ODS steels 5
1.3.1 Dispersion hardening 6
1.3.2 The production of ODS steels 7
1.3.3 The status of alternative routes to produce ODS steels 8
1.4 Objectives of the current work 9
Chapter 2. Theoretical basis **10**
2.1 Internal oxidation 10
2.1.1 Classical theory of Wagner for internal oxidation 10
2.1.2 Parabolic growth law for internal oxidation 14
2.2 Technical examples for the application of internal oxidation 15
2.2.1 Practical applications of internal oxidation for engineering materials 16
2.2.2 The status of the usage of internal oxidation to produce ODS steels 16
2.3 Computational thermodynamics and kinetics 19
2.3.1 CALPHAD 19
2.3.2 The background of the computational work in the current research 21
Chapter 3. Experimental Procedure **28**
3.1 Methods 28
3.1.1 Arc melting 28
3.1.2 Inductively coupled plasma-optical emission spectroscopy (ICP-OES) 29
3.1.3 Carrier gas hot extraction analysis (CGHE) 29
3.1.4 Metallographic preparation 30
3.1.5 Scanning electron microscopy (SEM) 30

3.1.6 Transmission electron microscopy (TEM) 31
3.1.7 Electron backscatter diffraction analysis (EBSD) 31
3.2 Produced materials 32
3.3 Oxidation experiment 34
3.3.1 First set of experiments 34
3.3.2 Second set of experiments 36
3.4 Mechanical testing 39
Chapter 4. Results and Discussion 41
4.1 As-cast alloys 41
4.2 Oxidation in evacuated quartz glass ampoules 43
4.2.1 Cr/Cr_2O_3 oxygen buffer results for Fe-16Cr-0.5Al and Fe-9Cr-0.5Al alloys 43
4.2.2 Fe/FeO oxygen buffer results for Fe-16Cr-0.2Al and Fe-9Cr-0.2Al alloys 53
4.2.3 V_2O/VO oxygen buffer results for Fe-16Cr-0.2Al and Fe-9Cr-0.2Al alloys 59
4.3 Oxidation in high temperature furnace by embedding Fe-Cr-Al alloy into oxygen buffer system 63
4.3.1 V_2O/VO oxygen buffer results for Fe-16Cr-0.2Al alloy 64
4.3.2 Oxidation of Fe-16Cr-0.2Al alloy with Cr/Cr_2O_3 oxygen buffer 67
4.3.3 Oxidation of Fe-16Cr-0.2Al alloy with VO/V_2O_3 oxygen buffer 72
4.4 Oxidation in high temperature furnace by embedding of Fe-Cr-Al-Y alloy into oxygen buffer system 87
4.4.1 Solubility of Y in iron-based alloys 88
4.4.2 Oxidation of Fe-16Cr-0.2Al-0.05Y alloy with VO/V_2O_3 oxygen buffer 89
4.5 Tensile tests 93
Chapter 5. Conclusions and Outlook 99
Appendix 102
A1. Publications 102
A2. Posters 102
A3. Presentations 103
A4. Published MSIT (Materials Science International Team) database 103
A5. Calculated oxygen activity versus temperature in Fe-O system 104
A6. Calculated Standard Gibbs energy of formation for relevant equilibria in V-O system 104
A7. The results of EDX analyses for impurities 105

A8. The interstitial diffusion coefficients in Fe 106
A9. The substitutional diffusion coefficients in bcc-iron 106
A10. The reliability of buffer system for the distribution of non-metallic particles on steel matrix 107
A11. TiC-Fe phase diagram 113
References 114

List of Figures

Fig. 1 Schematic representation of ITER fusion reactor [4]. 3

Fig. 2 Powder metallurgy route and its parameters to produce ODS steels. 7

Fig. 3 A schematic representation of concentration profiles of oxygen and less-noble alloying element (B) for A-B alloy in the case of internal oxidation. 11

Fig. 4 The reported result for depth of internal oxidation in Ag-3at.%Sn for atmospheric pressure for two selected temperatures in the work of Xu et al. 2015 [61]. The data points have been digitized from the original work and re-plotted. 15

Fig. 5 The calculated oxygen activity versus temperature for different metal/oxide equilibria using databases TCFE7 [88], Kjellqvist et al. [89], TCBIN [90] and Swamy et al. [91]. (a_{O_2} are unitless values). 22

Fig. 6 The calculated Y-O phase diagram in the work of Swamy et al. [91]. 24

Fig. 7. The phase diagram of V-O system based on the assessment of Yang et al. [92]. In order to show the most relevant oxides in this system up to 0.62 mole fraction of oxygen is presented in this phase diagram. 25

Fig. 8 Calculated Fe-Cr phase diagram in the iron-rich side using the database developed by Kjellqvist et al. [89]. 33

Fig. 9 The schematic illustration of the oxidation experiments in the first set of this work using evacuated and sealed quartz glass ampoule. 35

Fig. 10 The schematic illustration of the oxidation experiments in the second set of this work. In this set, a high temperature furnace under argon atmosphere was used. The alloy and power mixtures were in direct contact. 37

Fig. 11 The production route of sheet from as-cast button: (a) heating of the button with flame, (b) forging of the heated button to make a coin-shape sample, (c) rasping of the forged sample to remove the oxide scales from the surface, (d) the prepared sample for cold rolling, (e) the

rolling of the sample, (f) further rolling of the sample to the desired thickness of ~ 400 µm for this work, (g) the obtained sheets after cutting to smaller parts.....39

Fig. 12 The produced tensile sample from arc-melting buttons with a thickness of ~ 400 µm.....40

Fig. 13 Calculated partial isothermal section of Fe-Cr-Al system at 1000 ˚C and 1300 °C with alloy compositions indicated.....42

Fig. 14 Backscattered-micrograph of Fe-16Cr-0.5Al using SEM method after annealing at 1000 ˚C after 7 days with Cr/Cr_2O_3 buffer mixture. The arrows show the particles along the grain boundaries. 43

Fig. 15 A typical selected area for EDX area analysis shown by a white square (Fe-16Cr-0.5Al, annealed at 1000 ˚C for 7 days with the presence of Cr/Cr_2O_3 buffer mixture).....44

Fig. 16 Al-fraction values, their box-whisker-plot and the normal distribution for as-cast and annealed alloys. 45

Fig. 17 The investigation of Fe-16Cr-0.5Al alloy annealed with presence of Cr/Cr_2O_3 buffer mixture at 1000 ˚C after 7 days inside quartz glass ampoule: (a) A typical particle (HAADF image), (b) its elemental distribution profile along the indicated line. 46

Fig. 18 A typical individual elemental distribution maps for Fe, Cr, O, Al and N found in Fe-16Cr-0.5Al alloy annealed with presence of Cr/Cr_2O_3 buffer mixture at 1000 ˚C after 7 days inside quartz glass ampoule. 47

Fig. 19 The calculated standard Gibbs energy of formation of AlN (kJ/mol N_2) and Al_2O_3 (kJ/mol O_2) using TCBIN database [90]. 48

Fig. 20 Cross-section backscattered-micrograph of Fe-16Cr-0.5Al using SEM method after annealing at 1000 ˚C after 7 days inside evacuated quartz glass. No oxygen buffer system was used. The formation of AlN was not seen. 49

Fig. 21 Calculated partial isothermal section of Fe-Cr-Al-O-N system at 1000 ˚C. The Cr and Al contents of the system were fixed to 16.8 wt.% and 0.385 wt.%, respectively. 50

Fig. 22 Calculated partial isothermal section of Fe-Cr-Al-O-N system at 1000 ˚C. The Cr and Al contents of the system were fixed to 16.8 wt.% and 0.2 wt.%, respectively. 52

Fig. 23 Cross-section backscattered-micrograph of Fe-16Cr-0.2Al (A01) using SEM method after oxidation at 1000 ˚C after 7 days in presence of Fe/FeO buffer mixture. 53

Fig. 24 EDX analysis of Fe-16Cr-0.2Al (A01) after oxidation at 1000 ˚C after 7 days in presence of Fe/FeO buffer: (a) A higher magnification of the scale formed via secondary electrons-micrograph and indicated path for line scan, (b) the corresponding composition profile. 54

Fig. 25 Cross-section backscattered-micrograph of Fe-9Cr-0.2Al using SEM method after oxidation at 1000 ˚C after 7 days using Fe/FeO buffer. 55

Fig. 26 EDX analysis of Fe-9Cr-0.2Al after oxidation at 1000 ˚C after 7 days in presence of Fe/FeO buffer: (a) Cross-section secondary electrons-micrograph showing the formation of two layers in outer regions and indicated path for line scan, (b) the corresponding composition profile. 56

Fig. 27 Calculated partial isothermal section of the system Fe-Cr-Al-O under the oxygen activity of $10^{-14.9}$ at 1000 ˚C with alloy compositions indicated. 57

Fig. 28 The equilibrium oxygen activity for the exposure atmospheres and relevant oxides in the work of Zurek et al. (2011) [113]. 58

Fig. 29 The oxidation result of Fe-16Cr-0.2Al (A01) at 1000 ˚C after 7 days in presence of V_2O/VO oxygen buffer: (a) Cross-section backscattered-micrograph in outer regions (SEM method), (b) secondary electrons-micrograph, a higher magnification image showed the formed particles (SEM method). 59

Fig. 30 EDX analysis for the formed particles in Fe-16Cr-0.2Al (A01) at 1000 ˚C after 7 days in presence of V_2O/VO oxygen buffer: (a) Secondary electrons-micrograph and indicated path for line scan (SEM method), (b) the corresponding composition profile. 59

Fig. 31 The solubility of oxygen in bcc-matrix (Fe-16Cr) at 1000 ˚C. The data was calculated using the database developed by Kjellqvist et al. [89]. 61

Fig. 32 Calculated IOZ depth at 1000 ˚C for Fe-16Cr-0.2Al alloy in presence of V_2O/VO oxygen buffer. 62

Fig. 33 The oxidation result of Fe-16Cr-0.2Al (A01) after oxidation at 1300 ˚C for 20 hours in V_2O/VO mixture. The specimen was in the form of a small cube with a few millimeters size. The images were backscattered-micrographs using SEM method: (a) the micrograph of the external surface of the sample, (b) cross-section approximately through the middle of sample, showed a few oxide particles left on the surface (the cubic sample was ground 2 mm from one side). 64

Fig. 34 Calculated IOZ depth at 1300 ˚C for Fe-16Cr-0.2Al alloy in presence of V_2O/VO oxygen buffer. 65

Fig. 35 Calculated phase diagram of the system Fe-Cr-Al-O with V_2O/VO oxygen buffer (a) at 1000 ˚C and oxygen activity of $10^{-24.5}$, (b) at 1300 ˚C and oxygen activity of $10^{-18.7}$. Alloy compositions were shown in both diagrams and the oxygen activity for each temperature was fixed. Some tie-lines were illustrated by dashed-lines in two phase regions. 66

Fig. 36 The internal oxidation of Fe-Ni-Cr alloys after 8 hours at 1150 °C in H_2/H_2O mixture with the ratio of 1.36, (a) $\frac{N_{Fe}}{N_{Fe}+N_{Ni}} = 0.8 \text{ and } N_{Cr} = 0.02$, (b) $\frac{N_{Fe}}{N_{Fe}+N_{Ni}} = 0.8 \text{ and } N_{Cr} = 0.075$ [121]. 67

Fig. 37 Calculated partial isothermal section of Fe-Cr-Al-O-N system at 1300 ˚C. The Cr and Al contents of the system were fixed to 16.0 wt.% and 0.2 wt.%, respectively. 68

Fig. 38 The oxidation result of Fe-16Cr-0.2Al (A02) after oxidation at 1300 ˚C for 20 hours Cr/Cr_2O_3 mixture. The specimen was in the form of a small cube with a few millimeters size. The SEM images were backscattered-micrographs using SEM mthod: (a) the micrograph of the external surface of the sample, (b) cross-section approximately through the middle of sample, showed a few oxide particles left on the surface (after 2 mm grinding from one side). 68

Fig. 39 Calculated IOZ depth at 1300 ˚C for Fe-16Cr-0.2Al alloy in presence of Cr/Cr_2O_3 oxygen buffer. 70

Fig. 40 The simulated diffusion profile of Cr into Fe-16Cr-0.2Al (A02) at 1300 ˚C after 2 h, 20 h and 200 h, respectively (15.7 wt.% in the diagram was the Cr concentration of as-cast alloy measured by ICP-OES. See again Table 3). 70

Fig. 41 An obtained EDX line scan from the surface of Fe-16Cr-0.2Al (A02) into the middle of the cubic sample (after 2 mm grinding from one side) after the experiment at 1300 ˚C for 20h oxidation with Cr/Cr_2O_3 buffer mixture. 71

Fig. 42 An obtained Al EDX line scan from the surface of Fe-16Cr-0.2Al (A02) into the middle of the cubic sample (after 2 mm grinding from one side) after the experiment at 1300 ˚C for 20h oxidation with Cr/Cr_2O_3 buffer mixture. 71

Fig. 43 The internally oxidized zone Fe-16Cr-0.2Al (A02) with VO/V_2O_3 buffer for 20 hours on a section approximately through the middle of the cubic sample (after 2 mm grinding from one side). The images were backscattered-micrographs using SEM method: (a) at 1300 ˚C, (b) at 1450 ˚C. 73

Fig. 44 The cumulative size distribution of particles in Fe-16Cr-0.2Al (wt.%) after oxidation with (VO/V_2O_3) buffer for 20 h at 1450 ˚C. 73

Fig. 45 Variation of particles spacing with their standard error within oxidation zone for Fe-16Cr-0.2Al after intern oxidation at 1450 ˚C. 74

Fig. 46 A typical EDX region scan obtained from the produced particles in Fe-16Cr-0.2Al (A02) after oxidation experiment with VO/V_2O_3 buffer for 20 hours. 75

Fig. 47 The solubility of oxygen in bcc-matrix (Fe-16Cr) at 1300 ˚C. The data was calculated with the database developed by Kjellqvist et al. [89]. 76

Fig. 48 The calculated solubility of oxygen in Fe-16Cr at 1450 °C. 77

Fig. 49 The calculated IOZ depth for Fe-16Cr-0.2Al alloy oxidized with VO/V_2O_3 buffer system at 1300 °C and 1450 °C based on Wagner's theory of internal oxidation. 78

Fig. 50 The formation of oxide particles within the grains (light optical microscopy). The grain boundaries are highlighted with black arrows. 80

Fig. 51 Calculated phase diagram of the system Fe-Cr-Al-O with a VO/V_2O_3 oxygen buffer at fixed oxygen activities (some tie-lines were illustrated by dashed-lines): (a) at 1300 ˚C, (b) at 1450 ˚C. 81

Fig. 52 Cr atomic percentage (at.%) as a function of position in the spherical cell [119]. 82

Fig. 53 The radius of the oxide particle as a function of time [119]. 83

Fig. 54 The schematic comparison of the chemical potentials of metallic element in an oxide-oxide mixture (MO/ M_2O_3) with a metal-oxide mixture (M/MO).....84

Fig. 55 The calculated diffusion profile of V from (VO/V_2O_3) powder mixture into Fe-16Cr-0.2Al at 1450 ˚C for 2 h, 20 h and 200 h. 85

Fig. 56 FSD image with EBSD point analysis of different corundum precipitates. One pattern was shown prior to indexing to give an impression of the low pattern quality. 86

Fig. 57 The correlation of CI (confidence Index) and the probability of correct solution [132]. This image was graphically edited and represented. 87

Fig. 58 The phase diagram of Fe-Y phase diagram, (a) the complete composition range, (b) the enlarged section of Fe side [133]. 88

Fig. 59 Fe-12.3Cr-0.4Y (wt.%) alloy: (a) as-cast, (b) after annealing at 1200 °C for 10 days. The formation of $Fe_{17}Y_2$ or Fe-Y-Cr intermetallic phase for both conditions was seen (SEM method). 88

Fig. 60 The internally oxidized zone of Fe-16Cr-0.2Al-0.05Y alloy with (VO/V_2O_3) buffer for 20 h at 1450 ˚C on a surface approximately through the middle of sample (after 2 mm grinding from one side of cubic sample). The SEM images were cross-section backscattered-micrographs. The coarser oxide particles near the surface and finer oxide particles in the inner regions could be seen. 89

Fig. 61 The cumulative size distribution of particles in Fe-16Cr-0.2Al-0.05Y (wt.%) after oxidation with (VO/V_2O_3) buffer for 20 h at 1450 ˚C. 90

Fig. 62 Variation of particles spacing and the standard error within oxidation zone for Fe-16Cr-0.2Al-0.05Y after intern oxidation at 1450 ˚C. 91

Fig. 63 A typical EDX analysis for the coarser formed particles in Fe-16Cr-0.2Al-0.05Y at 1450 ˚C in outer regions of the sample after 20 h embedded in (VO/V_2O_3) oxygen buffer: (a) secondary electrons micrograph and indicated path for line scan, (b) the corresponding composition profile using 15 kV acceleration voltage showed the formation of aluminum-oxide particle. 91

Fig. 64 A typical EDX analysis for the finer formed particles in Fe-16Cr-0.2Al-0.05Y at 1450 ˚C located mainly in inner regions of the sample after 20 h embedded in (VO/V_2O_3) oxygen buffer: (a) secondary electrons-micrograph and indicated path for line scan, (b) the corresponding composition profile using 15 kV acceleration voltage showing mixed aluminum-yttrium oxide particle. 92

Fig. 65 The microstructure of Fe-16Cr-0.2Al alloy: (a) after rolling, (b) after annealing at 1000 °C for 3 hours.....93

Fig. 66 The comparison of the mechanical testing for both Fe-16Cr-0.2Al and Fe-16Cr-0.2Al-0.05Y after internal oxidation at 1450 °C for 5 hours with VO/V_2O_3 buffer. 94

Fig. 67 Particle numbers per unit volume (mm^{-3}) and their standard error as a function of distance within the internal oxidation zone (Δx) for Fe-16Cr-0.2Al and Fe-16Cr-0.2Al-0.05Y alloys after internal oxidation at 1450 °C. 95

Fig. 68 The calculated maximum solubility of Ti in iron in molar fraction shown as X(bcc, Ti) at different temperatures using the database developed by Hu et al. [141]. 97

Fig. 69 The calculated oxygen activity versus temperature in Fe-O system using the database developed by Kjellqvist et al. [89]. 104

Fig. 70 Calculated standard Gibbs energy of formation for relevant equilibria in this work using the database of Yang et al. [92]. 104

Fig. 71 A typical EDX spectrum for as-cast alloys. 105

Fig. 72 The reported data for interstitial diffusion coefficients in Fe after Heumann et al. [128]106

Fig. 73 The reported substitutional diffusion coefficients in Fe after H. Oikawa [129]. 106

Fig. 74 The agglomeration of particles on steel matrix (SE micrograph using SEM method). ..108

Fig. 75 The segregated phase on steel matrix: (a) SE-micrograph using SEM method, (b) an EDX line scan profile. This result was included in a conference paper (2016) presented in Italy [146].....108

Fig. 76 The segregated phases in other spots of the sample: (a) A SE-micrograph for segregated phases and indicated path for EDX scan (SEM method), (b) The recorded profile suggested the formation of MnS (Manganese sulfide).....109

Fig. 77 The calculated phase diagram of stainless steel-TiN up to 2 wt.% TiN. To calculate the phase diagram only the metallic elements (Fe-base, Cr 16.503 wt.%, Ni 12.380 wt.%, Mn 0.075 wt.%, Mo 2.629 wt.%) in stainless steel were considered.....110

Fig. 78 The calculated phase diagram up to 2 wt.% TiN. To calculate the phase diagram, all the elements present in the datasheet were considered (see Table 15).....111

Fig. 79 The calculated TiC-Fe phase diagram using TCFE7 [88] database.....113

List of Tables

Table 1. The standard nominal composition for some well-known RAFM steels.

Table 2. The included elements in MOBFE2 provided by Thermo-Calc company.

Table 3. Prepared alloys in this work and their chemical composition.

Table 4. Buffer compositions for oxidation experiments in the first set of experiments.

Table 5. Buffer compositions of the buffers for oxidation experiments in the second set of experiments.

Table 6. The parameters of the oxidation experiments in this work.

Table 7. EDX spot analyses of as-cast Fe-16Cr-0.2Al (A01) in different regions for metallic elements.

Table 8. The comparison of the chemical composition of the annealed alloy (Fe-16Cr-0.5Al) with and without oxygen buffer system (including reported standard deviations).

Table 9. The nitrogen content measured by CGHE method for Cr and Cr_2O_3 powder.

Table 10. The oxygen and nitrogen activity for Fe-16Cr-0.5Al alloy, in which the phases of AlN and Al_2O_3 and ferrite were in equilibrium with each other at 1000 °C.

Table 11. The composition of prepared alloys after cold rolling for the tensile tests.

Table 12. The summary of recorded UTS values for a reference sample and internally oxidized samples.

Table 13. The reported UTS values of ODS steels produced with powder metallurgy route in the literature.

Table 14. The quantitative results of EDX analyses for impurities.

Table 15. The chemical composition of the used steel powder.

Table 16. Sigma, CHI_A12 and fcc#2 and their constituents.

Table 17. Region IDs and the corresponding phases in shown in Fig. 78.

Table 18. The present phases in Table 17 with their SGTE notations and their constituents.

Chapter 1. Introduction

Large-scale electricity generation is driven by the global energy demand and to meet this demand partially, power generation by nuclear fusion technology is certainly one possibility. The use of high-performance structural materials in fusion reactors for high efficiency and safety issues is therefore crucial. Consequently, the development of such materials in fusion reactors has become a significant area of research in materials science and engineering. The first chapter of this work introduces the fusion reactors and the candidate materials for this type of reactors. The current research focuses on a special type of steel and its method of production, which is employed as structural materials in fusion reactors.

The second chapter aims to provide the necessary background knowledge essential for a comprehensive understanding of the research work. It also outlines the fundamental plan and approach undertaken to achieve the objectives of this study. The third chapter describes the experimental procedures and the methods used in this project. The observed results are shown and discussed in the fourth chapter. Finally, the conclusions and outlooks are highlighted in the fifth chapter.

1.1 Fusion reactors

A large amount of energy in nuclear fusion systems is released by the deuterium-tritium reaction, which is described as:

$$ {}^{2}_{1}\mathrm{D} + {}^{3}_{1}\mathrm{T} \rightarrow {}^{4}_{2}\mathrm{He} + {}^{1}_{0}\mathrm{n} + 17.6\ \mathrm{MeV} \quad (1) $$

Deuterium (D) and tritium (T) are isotopes of hydrogen known as hydrogen-2 and hydrogen-3, respectively. According to the above reaction, helium, neutron and a vast amount of energy (17.6 MeV) are generated when hydrogen isotopes fuse together despite their repellent positive nucleus charges. The amount of the released energy in the fusion reaction is several times the amount obtained from nuclear fission, and this would be a cleaner, more efficient and more abundant source of power. The energy in fusion reactors is absorbed as heat in the walls of the vessel, and the heat is removed by the coolant. The heated coolant is then circulated and used to produce steam and electricity by generators and turbines. To highlight the extent of generated energy in

fusion reactors, it is worth mentioning that during fusion to form 1 kg of helium, about 120 million kWh energy is released, corresponding to 12 million kilograms of coal [1].

The advancement of the quality, the reduction of uncertainties and risks, the acceleration of the analyses, and the facilitation of integrated modelling of complex fusion systems are among the international efforts for fusion systems [2]. Two significant milestones must be accordingly accomplished before commercial fusion plants can be realized as follows [3]:

1) The construction of a demonstration power plant known as DEMO (demonstration power station) which provides all the relevant experience and research for a prototype fusion reactor for industrial scale.
2) The realization of the ITER (International thermonuclear experimental reactor)

The DEMO reactor is currently under active global discussion, with anticipation that several DEMO reactors will be built in different countries to accelerate the commercialization of fusion power.

ITER project is among the greatest international energy projects, which has involved thousands of engineers and scientists from around the world. The construction of the ITER began in southern France in 2010 and will be the world's largest tokamak with twice the size of the largest machine currently in operation and ten times higher the plasma chamber volume. Deuterium-Tritium operation in ITER is planned to be begun in 2035 and is designed to generate 500 MW of fusion power from 50 MW of input energy.

For a better illustration, a schematic representation of the ITER fusion reactor and its key relevant components are shown in Fig. 1 on the next page. The cryostat shown in this figure is approximately 30 meters in height and 30 meters in width. It is an ultra-cool chamber that surrounds a vacuum vessel and the superconducting magnets.

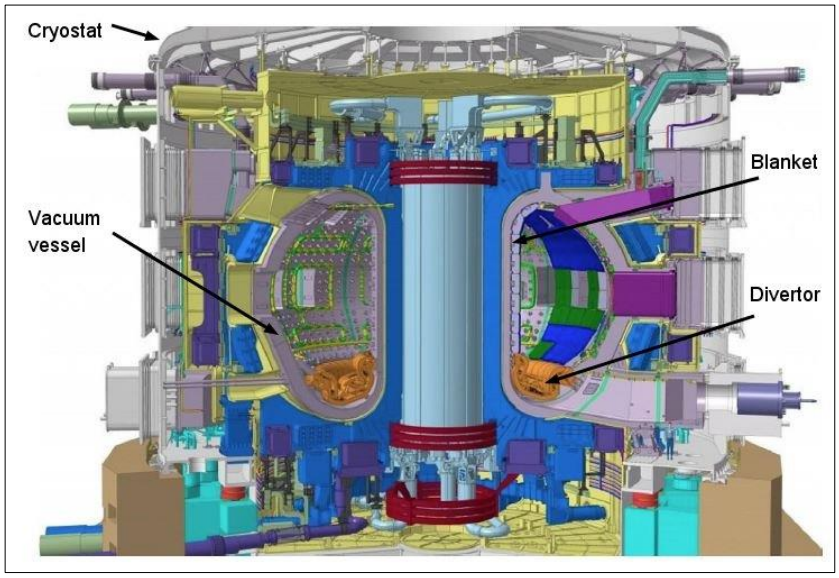

Fig. 1 Schematic representation of ITER fusion reactor [4].

The fusion reaction occurs inside the vacuum vessel (see Fig. 1), and the generated energy is captured and transferred via blanket region to a coolant for electrical power generation. The ITER vacuum vessel with an interior volume of 1600 m^3 provides support for the blanket and divertor, which are the main components that directly face the hot plasma.

The generated high-energy neutrons from fusion reactions damage the blanket alloy through the atomic displacements, which may leave vacancies or interchange of dissimilar atoms in the structure of materials. Additionally, due to the influence of irradiation, transmutations of nuclei to near-neighbors nuclei according to the Karlsruhe Nuclide Chart [5] might occur. These interactions can finally cause volumetric swelling and loss in strength of the structural materials [6, 7]. Considering this issue, the materials development, characterization and qualification for the structural applications in fusion reactors is a matter of importance and therefore a research topic. The following presents the proposed candidate materials for this type of reactors.

1.2 Materials selection for fusion reactors

The basic principle of choosing the structural materials for fusion reactors is using low activation materials. Radioactivity in fusion reactors is the consequence of neutron interactions with the structural materials of the reactor [8]. The safety and environmental

attractiveness of fusion power systems using low activation materials can be significantly enhanced compared to the usage of conventional structural materials [9]. The main promising candidate materials for this purpose can be divided into three groups: vanadium alloys, SiC/SiC composites, and reduced activation ferritic-martensitic (RAFM) steels [10, 11]. These three groups of materials have an optimum performance concerning parameters like high tritium breeding, high net thermal efficiency, and high power density [12].

For vanadium alloys, the focus is on V-Cr-Ti system with approximately 3-9 wt.% Cr, and about 3-10 wt.% Ti and the alloy of V-4Cr-4Ti (in wt.%), as the reference composition, has been selected [13, 14]. Muroga [15] in his publication titled 'Vanadium for nuclear systems' highlights the progress of vanadium alloys for fusion applications.

SiC/SiC composites appear to be another promising option. Several future fusion reactor design concepts, like the TAURO blanket of the European Union, the ARIESAS concept of the US and the DREAM concept of Japan, consider SiC/SiC composites as potential structural materials [16]. Katoh et al. report on the international scientific and technological achievements of SiC/SiC composites for fusion and broader engineering applications [17].

Another attractive candidate for fusion systems is RAFM steels, which have been developed based on massive industrial experiences on ferritic/martensitic steels [18]. RAFM steels have promising properties such as low sensitivity to irradiation-induced swelling and helium embrittlement [12], good structural stability and high thermal conductivity [19].

The primary metallurgical approach to obtain RAFM steels is to tailor alloying elements of the Cr-steels. Co, Ni, Cu, Nb and Mo elements must be especially restricted for this purpose [20], and W and Ta are the most important alternative alloying elements used in RAFM steels [21-23]. F82H, EUROFER 97 and JFL-1 are among the well-known developed RAFM steels for fusion reactors.

Table 1 presents the standard nominal composition of the above steels.

Table 1. The standard nominal composition for some well-known RAFM steels.

Steel name	Nominal composition (in wt.%)
F82H [24]	Fe-0.1C-8Cr-2W-0.2V-0.04Ta
EUROFER 97 [25]	Fe-0.11C-9Cr-1.1W-0.2V-0.07Ta
JFL-1 [26]	Fe-0.1C-9Cr-2W-0.19V-0.07Ta

9Cr-2WVTa [27], RUFER [28], CLAM [29] are additionally developed RAFM steels for fusion power plants which have similar compositions to F82H, EUROFER 97 and JFL-1.

RAFM steels are appealing structural materials but their high-temperature strength is limited, and the Oxide Dispersion Strengthening (ODS) method is one of the practical approaches to solve this issue [30]. The nano-sized oxide particles with high number density can act as pinning points to dislocation movement [31], and they prevent grain growth and primary recrystallization as well [32]. Dispersed nano-sized oxides may provide many trap sites for transmutant helium and radiation-induced defects [33]. Furthermore, they mitigate the embrittlement of in-vessel components in fusion reactors [34].

If the conventional high-chromium ferritic/martensitic steels for a fusion power plant first-wall and blanket structure were used, the upper operating temperature would be limited to 550-600 °C [35]. In contrast, ODS steels have the potential to expand the upper operating temperature to 650 °C or even 750 °C [12]. The improved creep resistance and fatigue strength at high temperatures are other advantages of ODS steels [36].

1.3 ODS steels

In this part, a brief overview of the strengthening mechanism through particle dispersion is provided. The standard production method for ODS steels is then explained, and the status of alternative production routes for this class steel class is also commented.

1.3.1 Dispersion hardening

The metal-based alloys are strengthened by a specific number of methods like grain refining for applications at low temperatures (Hall-Petch effect), solid-solution hardening (or alloying), and dispersion hardening with fine particles [37]. The dispersion hardening, as a strengthening mechanism which is applied for ODS alloys, is reviewed in this section. The dispersion of hard particles in the matrix is a common mechanism of strengthening for engineering alloys. Dispersion-strengthened alloys are usually for the applications with high service temperatures chosen since they have usable strength up to 80-90 percent of the melting point of the base alloy [38].

In dispersion-hardened systems, there is generally no atomic matching (coherency) between the second-phase particles and the matrix. The degree of strengthening with this method depends on the distribution of particles in the ductile matrix, the shape of particles, the average particle diameter, and mean interparticle spacing. Rods and plates strengthen approximately twice relative to spherical particles at equal volume fractions. The finer particles with higher volume fractions enhance the strength additionally [39].

The dislocation gliding in the matrix leaves loops around particles either by bowing between the particles or by cross-slipping around them. The stress necessary to expand the loop of dislocation between the precipitates, known as the Orowan stress, is given by [40]:

$$\tau = \alpha \mu b / L \quad (2)$$

where α is constant, μ is the shear modulus, b is Burgers vector and L is the spacing of the particles. All these dislocations spread out from the particle (as strain proceeds) and by intersecting the primary glide plane, hinder primary dislocation motion and lead to intense work hardening [40].

One more contribution to the work hardening apart from bowing and slipping of dislocations might be the frictional drag of jogs in dislocation climb. Jogs may be defined as short lengths of dislocations not lying in the same planes as the main dislocations but having the same Burgers vectors [41]. This contribution must be considered since

dislocation climb depends on the movement of vacancies (a thermally activated process) [42], which might occur in ODS steels at elevated temperatures.

1.3.2 The production of ODS steels

A typical powder metallurgical route to produce ODS alloys is shown in Fig. 2. This involves the mechanical alloying of pre-alloyed powders with Y_2O_3 powders using high-energy milling with a speed of usually 300 rpm to 600 rpm for up to 100 hours [43]. The choice of Y_2O_3 is based on the higher stability of this oxide. The equilibrium oxygen activity of Y_2O_3 and some other relevant oxides are reviewed in the Ellingham diagram in chapter 2. The input oxides (Y_2O_3) are dispersed finely throughout the matrix [44] and J. S. Benjamin first developed this technique in 1970 [45].

The next step in the production route of ODS steels is Hot Isostatic Pressing (HIP). In the HIP process, the simultaneous application of high pressure at elevated temperatures in a constructed vessel is executed for the hot compaction of the powders. In the HIP process, the recrystallisation of powder particles is enhanced through plastic deformation. The consolidation of metallic and oxide powders to higher densities, a more homogeneous material and near-net shapes will also be possible with HIP process [46]. The pressure inside the HIP chamber is usually generated by purified argon gas and it is between 100 to 200 MPa. The process temperature ranges from 950 °C to 1150 °C and a holding time of usually 1 to 4 hours [47-49].

In the later steps, the deformed powders are thermo-mechanically worked either with hot extrusion or hot rolling for the required shape. The process temperature here is usually between 1000 °C to 1150 °C [43]. The produced alloys might be heat treated according to the finally defined purposes.

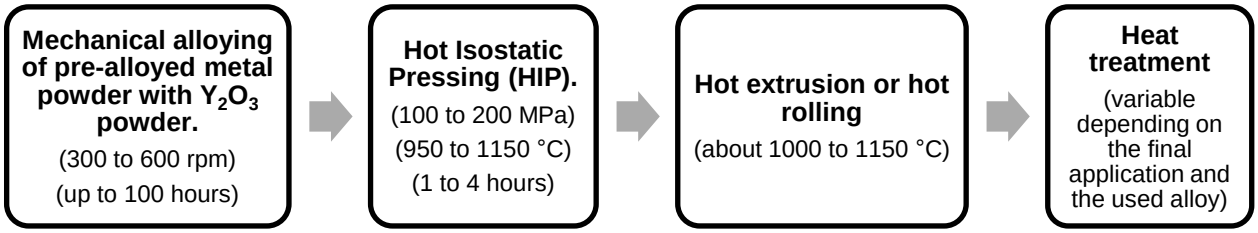

Fig. 2 Powder metallurgy route and its parameters to produce ODS steels.

Although the powder metallurgy route for ODS steels is well documented, it is considered a complex and costly fabrication technique [50, 51]. In the following section, some alternative production routes for this class of steels are provided.

1.3.3 The status of alternative routes to produce ODS steels

In this section, some alternative methods for producing ODS steels are presented, and their respective advantages and disadvantages compared to the powder metallurgy route are briefly discussed.

Guo et al. [52] reported a chemical processing (EDTA-citrate complex method) to deposit Y_2O_3 particles on the surface of the pre-alloyed steel powder, followed by hot isostatic pressing (HIP), forging and heat treatment. This method could drop the high-energy milling step, but it still needed the subsequent steps of the powder metallurgy route.

Sun et al. [53] prepared a ferritic steel powder (14Cr-ODS steel) by using the sol-gel method followed by chemical reduction in the mixture of hydrogen and argon. This method could provide ODS powders with relatively high purity, but it was not wholly independent of the powder metallurgy route. The produced ODS powders in this work were then processed using spark plasma sintering to make tensile samples.

Chen et al. [54] explored a new synthesis method to produce Fe/Y_2O_3 powder without mechanical alloying. They produced first Fe_2O_3/Y_2O_3 powder by using a concentrated solution of nitrates of iron and yttrium as the oxidizer, and malic acid. Fe/Y_2O_3 powder was then obtained by selective reduction under a hydrogen atmosphere. This method was very interesting but the addition of the other alloying elements (Cr, W,…) into the steel would add further complexities to this method. The further steps after mechanical alloying (HIP, extrusion, rolling, etc.) were still needed to process the obtained powders to achieve ODS bulk alloy.

The application of a contactless electromagnetically induced cavitation to disperse nanoparticles in the molten steel investigated by Sarma et al. [55] might be an interesting method for the production of ODS steels. However, in this work, an entirely successful dispersion of oxide particles on the steel matrix was not achieved, but it provided insight for additional investigations for this route.

1.4 Objectives of the current work

The ODS steels and their applications in fusion reactors were introduced in earlier parts. It was mentioned that the production of this type of steels using the powder metallurgy route was costly and complex; therefore, alternative routes remain a matter of research. Some alternative proposed methods and their advantages and disadvantages were reviewed in section 1.3.3 as well.

According to the above introductory part, the main objectives of this work are noted as:

1. In the internal oxidation method, an oxidizing medium is provided to oxidize selectively only the less-noble alloying elements and not the main elements in steels (i.e. Fe and Cr). This work evaluates how successful this hypothesis would be for the selected steels. The potential usage of this process as an alternative production route for ODS steels is then explored and how feasible this route might be is assessed. This makes the primary goal of the current work.
2. The next objective of this work is to analyze the type, size and spacing of oxides, which might be obtained through internal oxidation in the alloys.
3. The tensile properties of the steels produced using the internal oxidation method must be reported and compared to conventionally produced ODS steels with powder metallurgy.
4. To pursue the goal of this research, computational thermodynamics and kinetics are applied as essential tools. The computational work involves calculating Ellingham diagrams for different metal/oxide equilibria, determining various phase diagrams in the Fe-Cr-Al-(Y)-O system at different temperatures and oxygen activities and comparing these to the attained results. The estimation of the internal oxidation depth using classical internal oxidation's theory (Wagner's theory), the comparison to the observed experiments, and the calculation of diffusion profiles are among the other aspects of the computational work.

Chapter 2. Theoretical basis

The phenomenon of the internal oxidation process is explained and mathematically described in detail in this chapter. Later, the status of internal oxidation as a production method for different alloy systems, especially for ODS steels is considered. The Ellingham diagram, which serves as a key concept in this work for selected metal/oxide equilibria, is also presented.

2.1 Internal oxidation

Internal oxidation is the selective oxidation of the interior of an alloy. This phenomenon may occur at elevated temperatures in dilute solid solution alloys [56], in which oxygen diffuses into an alloy and oxide of less-noble alloying element is formed. The main criteria for such oxidation would be that the solute metal builds a more stable oxide than the base metal, and atomic oxygen has significant solubility and diffusivity in the matrix of the solvent metal at the temperature of oxidation. In addition, the concentration of less-noble alloying element is below the critical concentration for the transition from internal to external oxidation [57, 58]. In the following, the classical analytical description of internal oxidation is represented.

2.1.1 Classical theory of Wagner for internal oxidation

The mathematical description of internal oxidation based on the work of Wagner [59] is reviewed here and it is assumed that no external scale on the surface of the alloy exists. During the exposure of an alloy system to an atmosphere that contains oxygen, the dissolved oxygen diffuses towards the interior of the alloy and it reacts to less-noble alloying element in the system, and finally the oxide precipitates are formed. In the case of a binary alloy (A-B) to explain the internal oxidation model, it is considered that A is the base element and B is the less-noble alloying element. This is a prerequisite for this type of oxidation as mentioned earlier. By assuming that the formation of BO_ν oxide is a diffusion-based process and diffusion coefficients are constant and independent of concentrations, the differential equation for the concentration of B and oxygen in one dimension x, using Fick's second law is given by [59, 60]:

$$\frac{\partial C_i}{\partial t} = D_i \frac{\partial^2 C_i}{\partial x^2} \qquad (3)$$

In the above equation, C is the concentration of element i (i=O or B), t is time, D is the diffusion coefficient of diffusing element and x is the distance. By assuming the constant molar volume of the alloy (V_m) and by using ($C_i = N_i/V_m$), equation (3) can be converted to equation 4. N_i here represents the mole fraction of each element.

$$\frac{\partial N_i}{\partial t} = D_i \frac{\partial^2 N_i}{\partial x^2} \qquad (4)$$

The schematic concentration profiles of oxygen and B element are shown in Fig. 3.

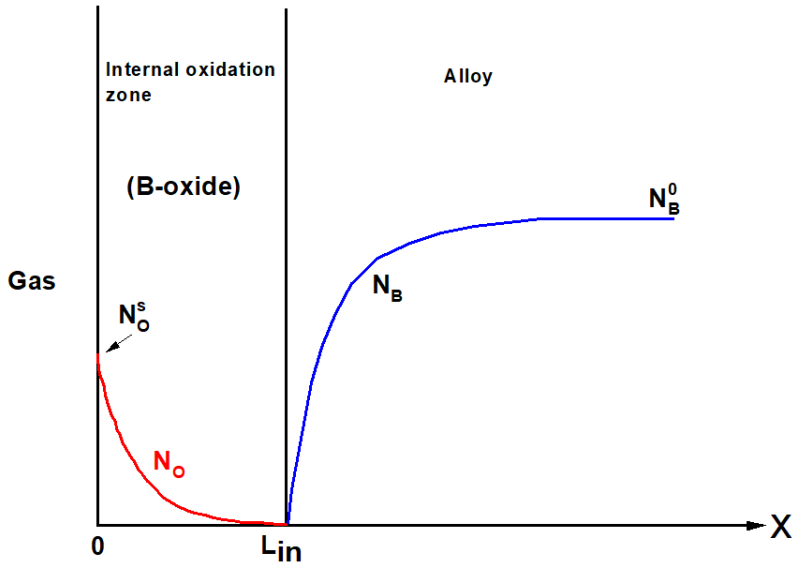

Fig. 3 A schematic representation of concentration profiles of oxygen and less-noble alloying element (B) for A-B alloy in the case of internal oxidation.

According to the concentration profiles in Fig. 3, four boundary conditions to solve equation (4) can be made [59, 60]:

$$N_O = N_O^s \quad \text{for } x = 0, t > 0 \qquad (5)$$

$$N_O = 0 \quad \text{for } x \geq L_{in}, t > 0 \qquad (6)$$

$$N_B = N_B^0 \quad \text{for } x \geq 0, t = 0 \qquad (7)$$

$$N_B = 0 \quad \text{for } x \leq L_{in}, t > 0 \qquad (8)$$

where N_O is the mole fraction of oxygen, N_O^s is the mole fraction of dissolved oxygen at the surface of alloy, x is the distance from the surface of alloy, t is time, L_{in} is the depth of internal oxidation zone, N_B is the mole fraction of less-noble element (B) and N_B^0 is the initial mole fraction of element B within the alloy before the internal oxidation. The

mole fraction of oxygen (N_O) is assumed to be zero outside the internal oxygen zone ($x \geq L_{in}$) since the oxygen is consumed fully inside this zone. In infinite time, at a fixed distance from the surface inside the internally oxide zone, oxygen concentration becomes theoretically equal to N_O^s. The solutions to (4) can be written as [59, 60]:

$$N_O = N_O^s \left[1 - \frac{\operatorname{erf}\left(\frac{x}{2\sqrt{D_O t}}\right)}{\operatorname{erf}(\gamma)} \right] \qquad (9)$$

$$N_B = N_B^0 \left[1 - \frac{\operatorname{erfc}\left(\frac{x}{2\sqrt{D_B t}}\right)}{\operatorname{erfc}\left(\gamma\sqrt{D_O/D_B}\right)} \right] \qquad (10)$$

where γ is a dimensionless time-independent kinetic parameter, “erf” and “erfc” are the mathematical functions defined as:

$$\operatorname{erf}(z) = \frac{2}{\sqrt{\pi}} \int_0^z e^{-t^2}\, dt \qquad (11)$$

$$\operatorname{erfc}(z) = 1 - \operatorname{erf}(z) = \frac{2}{\sqrt{\pi}} \int_z^\infty e^{-t^2}\, dt \qquad (12)$$

At the reaction front of the internal oxidation zone (x= L_{in}), oxygen flux must be equivalent to the flux of B atoms coming from the bulk of the alloy. Therefore, it is written [59, 60]:

$$\lim_{\delta \to 0} \left[-D_O \left(\frac{\partial N_O}{\partial x}\right)_{x=L_{in}-\delta} - \nu D_B \left(\frac{\partial N_B}{\partial x}\right)_{x=L_{in}+\delta} \right] = 0 \qquad (13)$$

In (13), δ is an exceedingly small increment in x at both sides of the internal oxidation front and ν is the O/B ratio of the oxide. By substituting (9) and (10) into (13), the following equation is obtained [59, 60]:

$$\frac{N_O^s}{\nu N_B^0} = \frac{\exp(\gamma^2)\ \operatorname{erf}(\gamma)}{\left(\frac{D_O}{D_B}\right)^{\frac{1}{2}}\ \exp\left(\gamma^2\ \frac{D_O}{D_B}\right)\ \operatorname{erfc}\left(\gamma\ \left(\frac{D_O}{D_B}\right)^{\frac{1}{2}}\right)} \qquad (14)$$

According to (14), the unknown parameter γ can be solved [59, 60]. In this equation, all the other parameters (ν, N_O^s, N_B^0, D_O,D_B) are known.

Two limiting conditions are especially interesting to be considered:

1. If $\gamma \ll 1$ and $\gamma \left(\frac{D_O}{D_B}\right)^{\frac{1}{2}} \gg 1$, then in (14) it can be approximated [59, 60]:

$$\mathrm{erf}(\gamma) \cong \frac{2}{\sqrt{\pi}}\gamma \qquad (15)$$

$$\mathrm{erfc}\left(\gamma \left(\frac{D_O}{D_B}\right)^{\frac{1}{2}}\right) \cong \frac{\exp\left(-\gamma^2 \frac{D_O}{D_B}\right)}{\gamma\sqrt{\pi \frac{D_O}{D_B}}} \qquad (16)$$

By replacing (15) and (16) into (14), it leads to:

$$\gamma \cong \left(\frac{N_O^s}{2\nu N_B^0}\right)^{\frac{1}{2}} \qquad (17)$$

Based on the assumed conditions: $\gamma \ll 1$ and $\gamma \left(\frac{D_O}{D_B}\right)^{\frac{1}{2}} \gg 1$, it can be concluded that:

$$\frac{D_B}{D_O} \ll \frac{N_O^s}{N_B^0} \ll 1 \qquad (18)$$

The product of the diffusion coefficient and the concentration (in mole fraction) of the element concerned is defined as permeability. In other words, this limiting condition becomes valid when the oxygen permeability $(N_O^s\, D_O)$ is much higher than the permeability of the alloying element B $(N_B^0\, D_B)$. As earlier mentioned, the concentration of oxygen at the boundary of the internal oxidation zone is zero:

$$x = L_{in} \rightarrow N_O = 0 \qquad (19)$$

Using (9), the depth of the internal oxidation (L_{in}) for this condition can be found as:

$$L_{in}^2 \cong 2\,\frac{D_O N_O^s}{\nu N_B^0}\,t \qquad (20)$$

By setting $K_{in} = \frac{D_O N_O^s}{\nu N_B^0}$,(20) comes to a shorter form as $L_{in}^2 = 2K_{in}\,t$ known as the parabolic law of internal oxidation. K_{in} is defined as an internal oxidation constant, a practical constant for internal oxidation studies.

The second limiting condition is written as [59, 60]:

2. If $\gamma \ll 1$ and $\gamma \left(\frac{D_O}{D_B}\right)^{\frac{1}{2}} \ll 1$, then based on (14) and (15), the γ parameter is:

$$\gamma \cong \left(\frac{\pi D_O}{D_B}\right)^{\frac{1}{2}} \left(\frac{N_O^s}{2\nu N_B^0}\right) \quad (21)$$

The limiting conditions are satisfied when:

$$D_O{}^{\frac{1}{2}} N_O^s \ll D_B{}^{\frac{1}{2}} N_B^0 \qquad (22)$$

The initial assumption and (22) both lead to the following inequality:

$$\frac{N_O^s}{N_B^0} \ll \frac{D_B}{D_O} \ll 1 \qquad (23)$$

For the depth of internal oxidation under this condition, it is therefore obtained as:

$$L_{in}^2 \cong \frac{(D_O N_O^s)^2\, \pi}{(\nu N_B^0)^2\, D_B}\, t \quad (24)$$

The solved differential equations for the concentration of oxygen and less-noble alloying element and achieved internal oxidation depths (L_{in}), were presented in this part. These equations are then utilized in chapter 4 and the theoretical calculations are compared to experimentally observed results.

2.1.2 Parabolic growth law for internal oxidation

Several studies have been conducted to assess the validity of Wagner's theory in various alloys. This section will present a few of the published internal oxidation studies and kinetic calculations. One instance of the internal oxidation in a binary alloy is illustrated in the work of Xu et al. (2015) [61] on the system of Ag-3at.%Sn alloys under two conditions: in air atmosphere ($p_{O_2} = 0.21$ bar) or in a pressurized furnace with pure oxygen ($p_{O_2} = 3.04$ bar). The experimental relationship between oxidation depth square (L_{in}^2) and oxidation time (t) for both pressures followed the parabolic growth rate. The reported results for ($p_{O_2} = 0.21$ bar), at two temperatures (973 K and 1073 K) were digitized and replotted in Fig. 4.

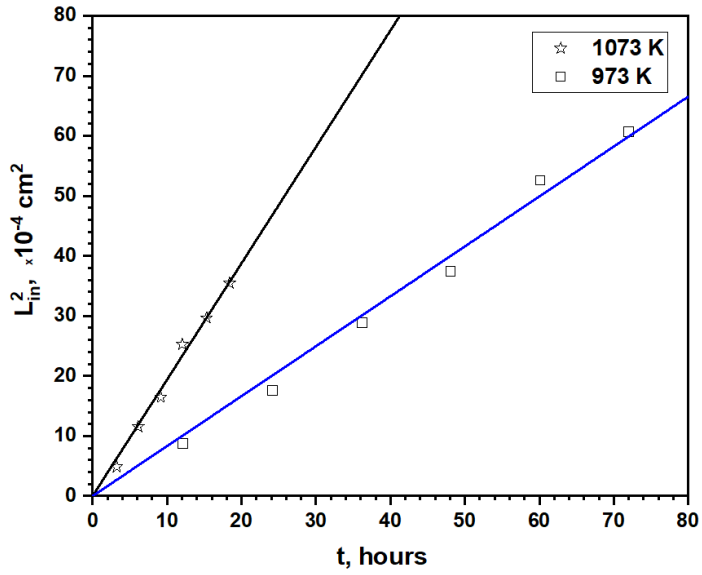

Fig. 4 The reported result for depth of internal oxidation in Ag-3at.%Sn for atmospheric pressure for two selected temperatures in the work of Xu et al. 2015 [61]. The data points have been digitized from the original work and re-plotted.

When dealing with multiple phases in the microstructure, Mertel et al. (2016) [62] studied the internal oxidation of five ternary alloys consisting of a base metal (Fe, Co, Ni, Cu) and two reactive metals (Zr+Y or Ce+Gd). In their work, internal oxidation depths versus the square root of time for produced alloys also followed parabolic kinetics. In principle, Wagner's theory would be applicable to the phenomena of nitridation and carburization in metallic alloys as well. Allen et al. (1999) [63] observed the parabolic behavior of internal nitridation for Ni-2V, Ni-5V, Ni-12V and Ni-3Nb (in wt.%) alloys for temperature ranges of 700 °C to 900 °C. Christ et al. (2003) [64] reported that the internal nitridation kinetics for nickel-base alloys of the system Ni-Cr-Ti generally obey a parabolic rate law. Udyavar et al. (2000) [65] studied the carburization and nitridation of model Fe-Ni-Cr alloys and noted that the internal precipitation (carbides and nitrides) rate was parabolic as well.

2.2 Technical examples for the application of internal oxidation

Some practical applications of internal oxidation to produce engineering materials are given here. Afterwards, the status of the usage of internal oxidation in the field of ODS steels is presented.

2.2.1 Practical applications of internal oxidation for engineering materials

Silver/metal-oxide has found extensive application in the electrical and electronics industries [66], and the most common materials in this area are based on Ag-CdO, Ag-SnO_2 and Ag-ZnO [67]. One technique to produce such composites (silver/metal-oxide) is the usage of internal oxidation [68, 69]. Another application of internal oxidation is the production of Cu-Al_2O_3 materials (alumina-dispersion-strengthened copper composites) [70, 71].

Many of the published results for producing such composites (silver/metal oxide, copper/alumina) are based on the internal oxidation of powders, followed by subsequent thermo-mechanical processing of the powders to fabricate the bulk composites. However, Ren et al. (2015) [72] used the internal oxidation method for Cu-Al alloy sheets, processed further by hot extrusion to produce Cu-Al_2O_3 bulk composites. In the next section, the status of the usage of internal oxidation for ODS steels is highlighted.

2.2.2 The status of the usage of internal oxidation to produce ODS steels

Schneibel et al. (2008) [73] examined the internal oxidation of $Fe_{17}Y_2$ and $Fe_{11}YTi$ intermetallics in either powders or flat surfaces to produce oxide dispersoids. In this research, they obtained oxides such as Y_2O_3 and $Y_2Ti_2O_7$ but they also observed the formation of some other oxides, such as $YFeO_3$ and Fe_2TiO_4 in the iron solid solution matrix. The latter oxides could be considered undesirable since the oxidation of the base element (Fe) occurred, as a complete selective oxidation of Y and/or Ti was not succeeded. The depth of internal oxidation for flat surfaces in this work was reported in the range of about 20-30 µm after three days.

Rieken et al. (2012) [74] produced oxide dispersion ferritic stainless steel powders (Fe-Cr-Y-Hf) without using mechanical alloying. The rapid solidification by using a reactive atomization gas (Ar-O_2) led to the formation of Cr-enriched oxides on the surface of alloy droplets. Later high temperature heat treatment, promoted internal oxygen exchange between Cr-enriched oxide and Y-enriched intermetallic precipitates, forming Y-(Hf)-O dispersoids throughout the alloy microstructure. However, the succeeding HIP for compaction of powders and following heat treatments was still necessary for the target ODS steel.

Tang et al. (2014) [75] reported a particular route to form titanium-oxide (Ti_3O_5) in a steel matrix (Fe-C-Mn-Si). Initially, the base metal was melted within the vacuum furnace. Then, the pure Ti wire was supplied to the molten alloy in multiple points, and electromagnet stirring was also active during the process. After reacting the whole Ti wire, the melt was cooled inside the crucible in the air. The following heat treatments and rolling were also performed. The formation of titanium oxide was based on the in-situ internal oxidation of titanium. Although this work supplied a valuable and straightforward way to strengthen the plain carbon steel, the addition of Cr and Y into the alloy by this route and the calculation of the exact partial pressure of oxygen during in-situ oxidation were still necessary to approach ODS steels. This information was not given in this publication.

Kachur et al. (2016) [76] examined the internal oxidation of Fe-Y alloys using Fe-Fe_2O_3 pack with Y contents of 1.5, 3, 6, 12 and 15 wt.%. In the as-cast alloys, a microstructure with two phases of Fe+ $Fe_{17}Y_2$ was observed. In the oxidized samples, only $Fe_{17}Y_2$ phase was oxidized. The formed oxides were not identified by characterization methods, but the proposed hypothesis was that the oxides are Y_2O_3, $YFeO_3$ or $Y_3Fe_5O_{12}$ by referring to previous works in this system. The maximum detected oxidation depth in this work was approximately 160 µm after 3 days.

Moghadasi et al. (2016) [77] suggested a new concept for the production of ODS steels. In this work, they used Fe-10Ni-7Mn (wt.%) as the master alloy, Fe-20Y (wt.%) intermetallic alloy as the source of yttrium and Fe-10TiO_2 (wt.%) as oxygen carrier. Fe-10TiO_2 was in the form of compressed discs which were produced by mechanical alloying of Fe and TiO_2 powders and final sintering at an elevated temperature (1120 ˚C). The master alloys of Fe-10Ni-7Mn and Fe-20Y using vacuum arc melting under an argon atmosphere were produced. Afterwards, both alloys were remelted in a vacuum arc melting furnace to obtain Fe-Ni-Mn-Y alloy. This step was followed by remelting the obtained ingot of Fe-Ni-Mn-Y with Fe-10TiO_2 discs under an argon atmosphere. The formation of Y-Ti oxides in the matrix was reported in this work, but the lack of Cr in the produced steel and using the mechanical alloying and several times of casting in this route were among the drawbacks of this method.

In the work of Wang et al. (2017) [78], powders of reduced activation steel with oversaturated Ti and Y were prepared. After a thermal treatment simulating hot isostatic pressing (HIP), the precipitation of Ti and Y oxides (TiO_2 and Y_2O_3) on the surface of the powders was observed. Inside the powder particles, the formation of larger Ti oxide dispersoids, and less oxygen-containing dispersoids of intermetallic compound (Fe_2Y) was also reported. This work suggested that the mechanical alloying step and HIP might be merged into a single step by adjusting the composition and optimizing the fabrication process. However, the overall cost and simplicity of the manufacturing process were still under question.

The above mentioned published works added scientific value to this field. However, most of them relied on the powder metallurgy route and the drawbacks of each production method were commented. In the current work, the internal oxidation of bulk steel alloys of Fe-Cr-Al-(Y) was investigated. The primary goal of this research was to examine the feasibility of the internal oxidation method, which would be entirely independent of the powder metallurgy route to disperse oxide particles on the steel matrix.

Internal oxidation might occur in ODS steels during the fabrication using a powder metallurgy route like the one published by Klimenkov et al. [79]. In their work, the formation of V-Mn-Cr oxide was reported, which might have affected the impact behavior of ODS steel negatively. Since no oxygen activity and phase diagram calculations in the work of Klimenkov et al. [79] were reported, the present research could brighten additionally the understanding of the computational work including required oxygen activities, phase diagrams and internal oxidation depths estimations in the field of conventionally produced ODS steels as well. The subsequent section reviews the thermodynamic and kinetic background in the Fe-Cr-Al-(Y) system. The oxidation behavior of the principal involved elements (Fe: base component, Cr: alloying element, Al and/or Y: oxide-forming elements) for successful internal oxidation of the alloy is also studied.

2.3 Computational thermodynamics and kinetics

To approach to the goal of this study, computational thermodynamics and kinetics (CALPHAD method) as powerful tools for experiment planning and result interpretation are applied. The CALPHAD calculation principles and Thermo-Calc software are briefly then discussed.

2.3.1 CALPHAD

CALPHAD is a method in which modelled Gibbs energies and derivatives are used to calculate thermodynamic properties and simulate transformations of multi-component materials. The basic principle of equilibrium calculations is based on the finding of the minimum Gibbs energy (G) for a system with constant pressure (p), temperature (T) and amounts of components (N_i). Each system may have different phases and the total energy of the system is equivalent to the sum of molar Gibbs energies of phases (G_m^α) and the molar fractions of the phases (m^α). This can be written as [80]:

$$G = \sum_\alpha m^\alpha G_m^\alpha \qquad (25)$$

The above Gibbs energy function may have several minima and the most negative value is called global minimum and corresponds to a stable equilibrium. The other local minima are known as metastable equilibria. The molar Gibbs energy of each phase is expressed as functions of T, p and mole fractions of components in α-phase denoted as x_i^α or as site fractions of constituents k on sublattices l of α-phase known as $y_k^{(\alpha,l)}$. The equilibrium assumption (25) can now be written as [80]:

$$\min(G) = \min\left(\sum_\alpha m^\alpha G_m^\alpha\left(T, p, x_i^\alpha \ or \ y_k^{(\alpha,l)}\right)\right) \qquad (26)$$

As mentioned in the above equation, T and p are kept constant. Three extra constraints for an approach to the solution of equilibrium assumption (26) can be noted as:

a) Total amount of each component (N_i) is kept constant.
b) The sum of site fractions in each sublattice is equal to unity.
c) The charges of ionic species sum up to zero in each phase.

These constraints (a to c) are formulated in equations (27) to (29), respectively [80].

$$\sum_{\alpha} m^{\alpha} \sum_{l} a^{(l)} \sum_{k} b_{k,i}^{(\alpha,l)} \cdot y_k^{(\alpha,l)} - N_i = 0 \qquad (27)$$

$$\sum_{k} y_k^{(\alpha,l)} - 1 = 0 \qquad (28)$$

$$\sum_{l} a^{(l)} \sum_{k} q_k^{(\alpha,l)} \cdot y_k^{(\alpha,l)} = 0 \qquad (29)$$

In equation (27), $a^{(l)}$ and $b_{k,i}^{(\alpha,l)}$ are the fractions of sites of sublattice l referred to all sites of the phase, and the stoichiometric numbers of component i in species k on sublattice l of α-phase, respectively. In equation (29), $q_k^{(\alpha,l)}$ is the charges of ionized species k on sublattice l of α-phase.

To solve equilibrium assumption (26), Eriksson [81] and Hillert [82] used the Lagrange multiplier method in which the equations (27) to (29) are each multiplied by a Lagrange coefficient and added to equation (26). The new sum is called S and it is equal to G and therefore the minimum of S-function is the same as minimum in equilibrium assumption (26).

According to Hillert [82], the Lagrange multiplier of equation (27) is identical to chemical potentials (μ_i) of i-component. The Lagrange multiplier of equations (28) and (29) are unknown and are designated as $\phi^{(\alpha,l)}$ and ϕ_e^{α} , respectively.

The derivatives of S-function to unknown parameters $(m^{\alpha}, y_k^{(\alpha,l)}, \mu_i, \phi^{(\alpha,l)}, \phi_e^{\alpha})$ must be zero and two sets of equations can be written as follows [80]:

$$\frac{\partial G_m^{\alpha}}{\partial y_k^{(\alpha,l)}} + \sum_{i=1}^{r} \mu_i \cdot a^{(l)} \cdot b_{k,i}^{(\alpha,l)} + \frac{\phi^{(\alpha,l)}}{m^{\alpha}} + \frac{\phi_e^{\alpha}}{m^{\alpha}} \cdot a^{(l)} \cdot q_k^{(\alpha,l)} = 0 \qquad (30)$$

$$G_m^{\alpha} - \sum_{i} \mu_i \sum_{l} a^{(l)} \sum_{k} b_{k,i}^{(\alpha,l)} \cdot y_k^{(\alpha,l)} = 0 \qquad (31)$$

To solve the sets of equations described above and find equilibria for different and highly complex thermodynamic systems, several software packages like FactSage [83], Pandat [84] and Thermo-Calc have been developed. The thermodynamic and phase

equilibria calculations are executed in this work with Thermo-Calc software. The first version of the software was released in 1981 [85] and Sundman et al. [86] later in 1985 published the first description of the software in CALPHAD journal officially. Since Thermo-Calc began, the software and the thermodynamic databases have been regularly developed and improved. This includes for example, adding new features and enhancing the visualization of the software, fixing bugs, updating the add-on modules, and extension of various thermodynamic databases by increasing the number of the involved elements. In this work, steel and Fe-alloys (TCFE), as the main thermodynamic database, and some other relevant databases are used which are introduced in the next section. The fundamental basis of the oxidation and the databases applied in the current research are also presented and discussed in more detail.

2.3.2 The background of the computational work in the current research

In the first part of the computational work, the oxidation behavior of the involved metals in the system using the Ellingham diagram must be understood. The standard free Gibbs energy of the formation for the metal oxide per one mole of oxygen (ΔG^{o}_{molar}) and the related equilibrium activity of oxygen (a_{O_2}) is defined as [87]:

$$\Delta G^{o}_{molar} = RT \ln\left(\frac{p}{p^{o}}\right) = RT \ln a_{O_2\,(equil)} \;\rightarrow\; a_{O_2\,(equil)} = \exp\left(\frac{\Delta G^{o}_{molar}}{RT}\right) \qquad (32)$$

In the above equation, R is the gas constant, T is the absolute temperature, p is the pressure, and p^{o} is the standard pressure. The basic principle for the oxidation of a pure metallic element is that a higher oxygen activity than the equilibrium value obtained in (32) leads to metal oxidation. The plotting of experimentally determined variation ΔG^{o}_{molar} with T for the oxidation of metals can be approximated to a straight line when no change of state is present. This is written as [87]:

$$\Delta G^{o}_{molar} = \Delta H^{o}_{molar} - T\,\Delta S^{o}_{molar} \qquad (33)$$

ΔH^{o}_{molar} is the molar standard enthalpy of oxidation, and ΔS^{o}_{molar} is the molar standard entropy for oxidation. When a change in phase of a metallic element (M) or oxide product (MO_v) occurs, the slope of the lines changes slightly. This is seen since the enthalpy of a higher temperature phase, for example the liquid phase, exceeds the

enthalpy of a solid phase by the latent heat of melting, and therefore the slope of the line slightly changes.

In this approach, the equilibrium oxygen activities (a_{O_2}) shown in equation (32) for the oxidation of metallic elements in the target system (Fe, Cr, Al and Y) at different temperatures have to be calculated accordingly. The results versus inverse temperature (1000K /T) are plotted in Fig. 5. Selected temperatures (1000 °C, 1300 °C and 1450 °C) with vertical lines are seen in Fig. 5 as well (a_{O_2} are unitless values). The equivalent oxygen partial pressures (p_{O_2} in bar) for selected oxygen activities (a_{O_2}) at these temperatures are given later in chapter 3.

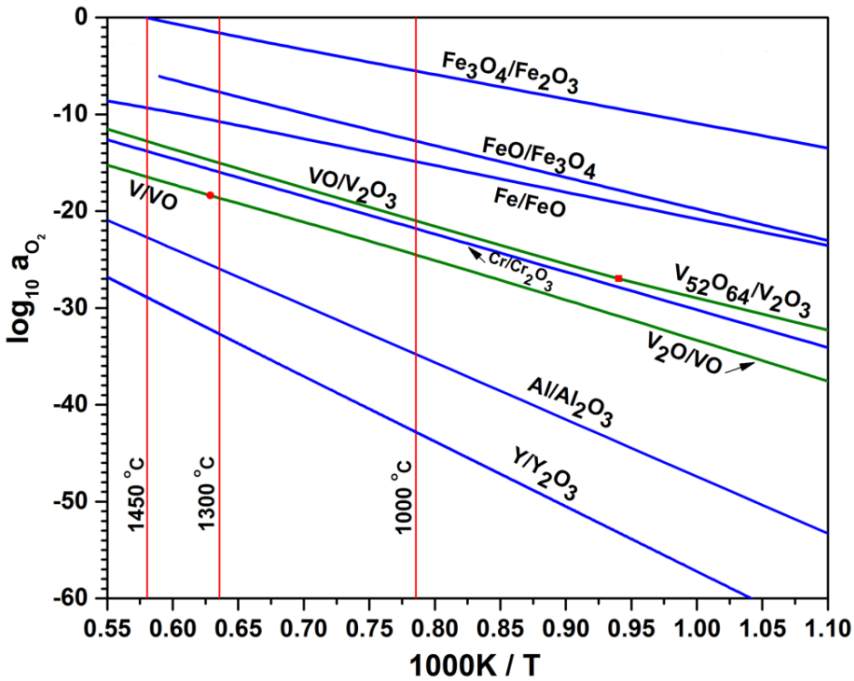

Fig. 5 The calculated oxygen activity versus temperature for different metal/oxide equilibria using databases TCFE7 [88], Kjellqvist et al. [89], TCBIN [90] and Swamy et al. [91]. (a_{O_2} are unitless values).

It is seen (Fig. 5) that at a defined temperature for example, at 1000 ˚C, the equilibria of (Al/Al_2O_3) and (Y/Y_2O_3) show lower oxygen activities than the corresponding oxygen activities for Fe and Cr equilibria. However, in this approach, the activities of metallic elements are equal to one, while the activity values of Fe, Cr, Al and Y in a real steel alloy are lower than one. The thermodynamic databases (TDB files) used to obtain the

Ellingham diagram (Fig. 5) are TCFE7 [88], Kjellqvist et al. [89], TCBIN [90] and Swamy et al. [91]. The following provides a brief introduction to these databases.

TCFE7 is a thermodynamic database for various types of Fe-based alloys (stainless steels, cast irons, tool steels, HSLA steels, …) applied in Thermo-Calc software. The steels/Fe-alloys database is based on the reassessment of binary and many ternary subsystems, and its first release (TCFE1) backs to 1992. Some of the applications of the steels database can be mentioned as follows:

1. The prediction and description of the oxidation, carburization and nitriding of the interested steels
2. Optimization of heat treatments in steels
3. The study of the influence of alloying elements on the phase stabilities and solubility limits of alloying elements in each phase
4. Control of slag systems in steel making industries

The range of the recommended maximum content in TCFE7 for Cr and Al are 30 and 5 (wt.%), respectively. In TCFE7, all oxide phases for the Fe-Al-Cr-O system are updated or incorporated into the database. In addition, the description of spinel, halite, and corundum phases allows accurate prediction for oxidation applications.

Kjellqvist et al. [89] provide a thermodynamic description for a quaternary system of Cr-Fe-Ni-O. In this work, the subsystem of Cr-O is used to calculate the equilibrium of Cr/Cr_2O_3 and its corresponding equilibrium oxygen activities. The subsystems of Fe-Cr and Fe-O are used in this database as well. Appendix 5 illustrates the calculated oxygen activity versus temperature in Fe-O system using the database file described by Kjellqvist et al. [89].

TCBIN [90] or Thermo-Calc binary solutions database contains many critically-assessed thermo-chemical data, which helps calculate the binary systems. TCBIN covers 67 elements with 360 critically assessed binary systems. The system of Al-O is calculated using this database, and the equilibrium oxygen activity is then achieved.

The Y-O system is calculated using the database file described in the work of Swamy et al. [91]. In this assessment, the Y_2O_3 polymorphs are described in a narrow

homogeneity range as stoichiometric compound for simplified calculations. The calculated Y-O phase diagram in the work of Swamy et al. [91] is shown in Fig. 6.

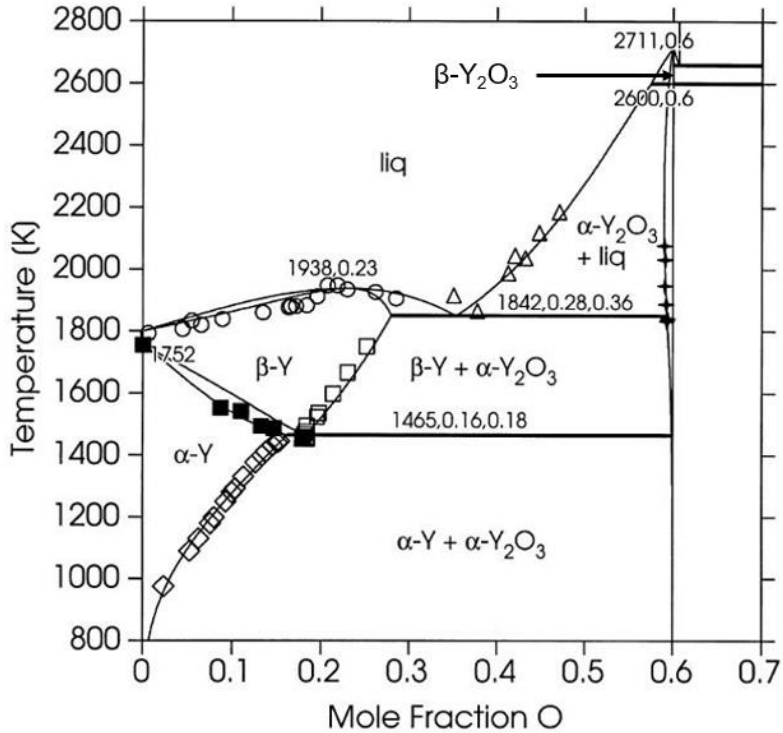

Fig. 6 The calculated Y-O phase diagram in the work of Swamy et al. [91].

α-Y has hcp crystal structures that is stable up to 1751 K and then transforms to β-Y with bcc crystal structure. Both phases have considerable solubility for oxygen in their crystal lattice. α-Y_2O_3 and β-Y_2O_3 are the stable oxides in this system which have stability up to 2600 K and 2711 K (melting temperature), respectively.

Moreover, the calculated Ellingham diagram (Fig. 5) is used to evaluate the oxygen buffer systems to fix the environmental oxygen partial pressures, i.e. the oxygen activities for the experiments. In this work, solid-state powder mixtures to adjust the oxygen partial pressures are selected. To calculate the candidate buffer systems, the dataset file for the V-O system based on the assessment of Yang et al. [92] in addition to the above stated databases is used. The phase diagram of this system using the provided dataset file is then calculated.

In Fig. 7, the calculated phase diagram illustrates the most relevant oxides in this system for the current work. The diagram includes the illustration of these oxides up to a mole fraction of 0.62 for oxygen.

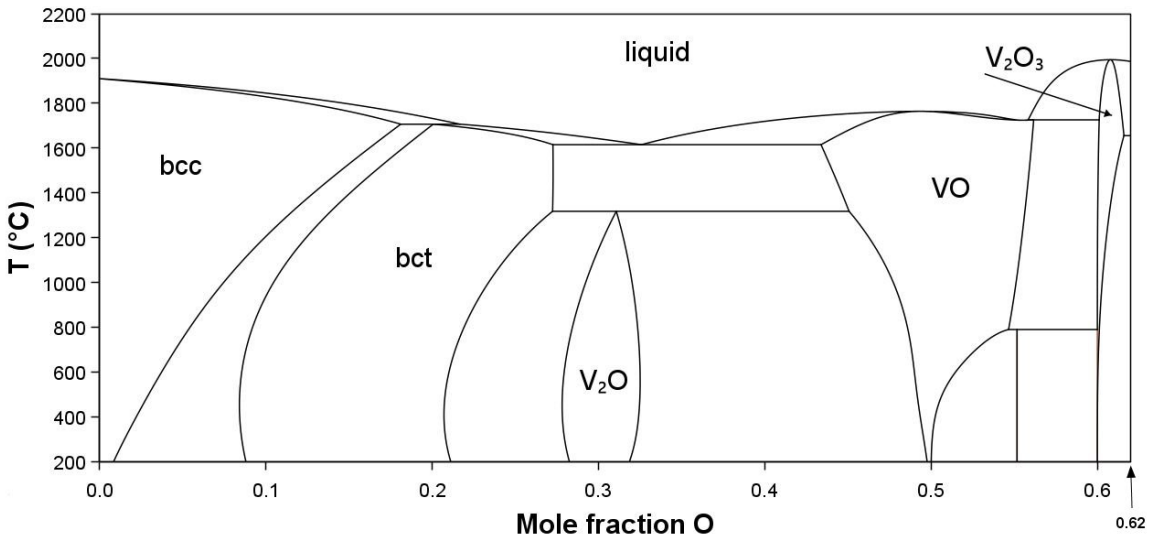

Fig. 7. The phase diagram of V-O system based on the assessment of Yang et al. [92]. In order to show the most relevant oxides in this system up to 0.62 mole fraction of oxygen is presented in this phase diagram.

In this system (Fig. 7), oxygen has specific solubility in bcc vanadium which forms a solid solution known as α phase. The β-phase (shown as bct in Fig. 7) has a bct crystal structure (body centered tetragonal) for vanadium in which oxygen atoms are distributed preferentially in one of the three sets of octahedral interstitial sites. The V_2O phase has monoclinic crystal symmetry with a certain area of stability and VO (halite) has B1 structure, which exists over a more comprehensive range of oxygen contents other than the ideal 0.5 molar fraction of oxygen. The other relevant oxide in this work is V_2O_3 which is sesquioxide with a corundum structure. The standard Gibbs energy of formation for relevant equilibria of oxides (V/VO, VO/V_2O, VO/V_2O_3) in this system are calculated and shown in Appendix 6.

The most important criterion for choosing an oxygen buffer system for this work is the location of its equilibrium reaction line in the Ellingham diagram. The line must be above (Al/Al_2O_3) and (Y/Y_2O_3) line, lower than (Fe/FeO) equilibrium line and ideally close to (Cr/Cr_2O_3) line. This is important since Al and/or Y must be selectively oxidized compared to Fe and Cr as earlier noticed. Based on this concept, (Cr/Cr_2O_3) powder

mixture seems to be an ideal buffer for the goal of this work. Since the activity of Cr as an alloying element within the steel is lower than one and the activity of Cr in the powder mixture is equal to one, the oxidation of Cr within the steel might not be then expected to occur. According to this preliminary concept, the oxidation of steel alloy with (Cr/Cr_2O_3) oxygen buffer is planned. After observing the results for (Cr/Cr_2O_3) buffer, experiments are optimized and tailored for the aim of the current work.

In addition to thermodynamic calculations, the diffusion profiles and the growth of particles are calculated by DICTRA software using MOBFE2 [93] database. DICTRA (diffusion-controlled transformations) is an add-on module within Thermo-Calc for the simulation of diffusion-controlled reactions in multi-component systems and it is first commercially licensed in 1992. Inter-diffusion in compounds, homogenization of alloys, growth or dissolution of intermetallics, carbides and micro-segregation during solidifications are among the main applications of this module.

The mobility databases (DICTRA databases) contain the mobility data of an element in a specific phase as a function of the temperature and the composition. The various diffusion coefficients can be obtained if the mobility database is combined with the thermodynamic database. Each mobility database is specifically compatible with the thermodynamic database of the same class of materials, e.g. TCS mobility database of steels is compatible with thermodynamic databases of steels used in Thermo-Calc software, and this is also valid for the other class of mobility databases. In this work, MOBFE2 [93], a kinetic database containing mobility data of Fe-based alloys and compatible with the TCFE thermodynamic database, is applied. It includes 24 elements as shown in Table 2 and it is applied for the simulation of diffusion profiles, and oxides growth kinetics.

Table 2. The included elements in MOBFE2 provided by Thermo-Calc company.

Including elements in MOBFE2
Fe, Al, Ar, B, C, Ca, Co, Cr, Cu, Mg, Mn, Mo, N, Nb, Ni, O, P, S, Si, Ta, Ti, W, V, Zr

The theoretical background, including the internal oxidation process and the computational thermodynamics and kinetics to approach the objectives of this work, were described in this chapter. Applying extremely low oxygen activities for the iron

alloys with trace amounts of aluminum and yttrium (lower than 1 wt.%) to avoid the formation of external scales, and to obtain steels with optimized properties might make this research distinct in this area. Considering that Fe-Cr-Al alloys in the iron-rich region typically contained around 5 to 10 wt.% Al, previous studies primarily centered on high-temperature oxidation in ambient atmospheres or atmospheres with higher oxygen activities [94-98]. The published works in this field mainly focused on the performance of steel alloys in service and the study of the generated external scales. In the following chapter, the experimental procedures for this work are outlined.

Chapter 3. Experimental Procedure

The methods and equipment used in this research are introduced in this chapter. The oxidation experiments, the experimental setup and tensile testing executed on the alloys are also given in this section.

3.1 Methods

The methods used in this work include: arc melting to produce the materials, inductively coupled plasma-optical emission spectroscopy (ICP-OES) and carrier gas hot extraction (CGHE) analysis to measure the chemical composition of materials, scanning electron microscopy (SEM) coupled with EDX detector to observe the microstructure of materials, transmission electron microscopy (TEM) for more detailed microstructure analyses, and electron backscatter diffraction analysis (EBSD).

3.1.1 Arc melting

This method provides a technique to melt various materials with remarkably high melting points and materials susceptible to oxidation. The principle of melting is to generate an arc between the upper electrode and the materials. In this work, the arc melting furnace (AM/0.5, Edmund Bühler) could melt approximately 500 g of metallic pieces and was able to reach the maximum temperature of about 3500 °C.

The electrode in this work was non-consumable and made of tungsten; the electrode holder was a water-cooled copper tube, and the materials were inserted in a water-cooled copper platform. After three cycles of evacuation and filling with argon, the atmosphere of the chamber was sealed by argon (Ar 6.0) to approximately 600 mbar. The arc was generated by passing an electrical current through the electrode, which melted the materials. The output power could be increased by raising the current to melt the materials with higher melting points. The buttons were flipped and remelted five times to improve the homogeneity of the produced alloys. In addition, Zr metallic piece inside the chamber as an oxygen-getter was used to obtain higher qualities of final cast alloys.

3.1.2 Inductively coupled plasma-optical emission spectroscopy (ICP-OES)

ICP-OES is an attractive method that is applied for the chemical analysis of a variety of materials. The sample is decomposed into atoms and ions of the elements by applying plasma. The atomic and ions emission emanating from plasma is viewed in either a radial or axial configuration, collected with a lens or mirror, and imaged onto the entrance slit of a wavelength selection device. Simultaneous multi-element determinations are performed for up to 70 elements with the combination of a polychromator and an array detector [99].

In this work, optical emission spectrometry (ICP-OES, OPTIMA 4300 DV from PerkinElmer, iCAP 7600 from Thermo Fisher Scientific) was used. About 20 – 50 mg of the samples (weighing accuracy ± 0.01 mg) was dissolved in 10 ml mixed acid of hydrochloric acid, nitric acid and millipore water at 334 K for four hours in an ultrasonic bath. The main components were analyzed with four different calibration solutions and an internal standard (Sc). Three major wavelengths of the elements were then used for the calculation.

3.1.3 Carrier gas hot extraction analysis (CGHE)

The oxygen and/or nitrogen contents of the alloys were examined with the method of carrier gas hot extraction (CGHE). The method has been widely applied for especially low oxygen contents in metals and alloys for over thirty years. The basic procedure of CGHE analysis is written as [100]:

1. Reduction of oxygen in the sample by carbon, commonly assisted by metallic melt-forming additives
2. Quantitative release of gaseous reaction products under defined temperature and time
3. Selective and quantitative detection of the evolved gases

A commercial oxygen/nitrogen analyzer TC600 (LECO) was used for this work. The oxygen concentration was calibrated with two certified standards (ELTRA1003, ELTRA1004 from ELTRA). The calibration was verified with another certified standard (502-257 from LECO). The calibration range was close to the concentration of the samples and the standards, and the samples were weighed with a mass in the range

from 100 to 500 mg (weighing accuracy ± 0.1 mg). The samples and standards were loaded in an out-gassed (6300 W) graphite crucible and the measurements took place at 5800 W. The evolving gases CO_2 and CO were swept out by helium as an inert carrier gas and measured by infrared detectors.

3.1.4 Metallographic preparation

In order to prepare the samples for metallographic investigations and microstructure studies, each specimen was ground up to grade # 4000 (SiC papers, Struers GmbH) and then polished with OPS suspension. Afterwards, the specimens were ultrasonically cleaned in isopropanol. The samples later were studied and characterized by analytical tools like SEM, TEM and EBSD.

3.1.5 Scanning electron microscopy (SEM)

SEM is a well-known and prevalent imaging technique that uses electron beams. The microstructures of the specimens were imaged with FEIXL30S microscope, coupled with EDX detector for compositional analyses in this work. In the following, the basic principles of this method are presented briefly.

In this method, a focused beam of electrons is deflected by electromagnetic coils and the beam scans across the surface of the specimen. The interaction of the electron beam and atoms of the sample generates various signals including Auger electrons, Secondary electrons (SE), Backscattered electrons (BSE), and characteristic X-rays. The source of information lies in these signals, which originated from different interaction volumes in the sample [101].

The most used signals for materials science and engineering studies are SE, BSE and characteristic X-rays. SE has an energy of less than 50 eV and the escape depth of these electrons is about 5-50 nm. BSE can have energy from 50 eV to about the incident beam energy and their escape depth is hundreds of times greater and the escape depth of characteristic X-rays is greater than BSE. The application of 30 kV as an acceleration voltage results in an interaction volume of about 2 to 3 µm in iron alloys. BSE electrons carry important information about the structures under the surface of the samples. When the incident beam displaces an electron from an inner shell of the sample, an electron from an outer shell fills the inner shell and causes a release of

characteristic X-ray. This technique is commonly referred to as Energy Dispersive X-ray (EDX) analysis, which enables the determination of composition at specific locations, areas up to 10 cm in diameter, or along a designated line within the sample [102].

3.1.6 Transmission electron microscopy (TEM)

The primary mechanism of the imaging of TEM is that a beam of electrons illuminates the sample, and electrons may pass through the sample without being scattered or may be diffracted off-axis by interaction with the sample or they might also be backscattered. The transmitted electrons are refocused and then magnified by an electromagnetic lens and are projected on a phosphorous screen to the visible form. The vacuum system for the operation of TEM is essential to prevent electrons collision with gas atoms and hydrocarbons [103].

Depending on the position of the objective aperture, the diffracted and unscattered electrons can be used to generate bright and dark field images, respectively. In the bright field mode, only the transmitted electrons can pass through the aperture which had been weakened as it passed through the specimen with variable mass density in different area of the sample. Based on this concept, the thick area, and inclusions of heavy atoms of the specimen show dark zones on the screen. On the other hand, transmitted electrons are blocked by the aperture in dark field mode, and the diffracted electrons could pass. Consequently, the crystal information of a specimen could become bright in this mode if the diffraction condition is satisfied [104]. TEM investigations in this work were performed using a FEI Tecnai 20 F (200 kV, field emission gun) microscope with a high angle annular dark field (HAADF) detector. The EDX spectra were recorded using an EDAX Si/Li detector with an ultra-thin window.

3.1.7 Electron backscatter diffraction analysis (EBSD)

EBSD is a microstructure-crystallographic technique and a SEM-based method that provides essential data on the texture of material, crystal orientation mapping, grain size analysis and the determination of phases based on the crystallographic structure contrast. In this method, the sample is tilted to 70° to horizontal and an electron beam is incident on the surface. The diffracted electrons, which exit near the Bragg angle, produce a pattern composed of intersecting bands. The diffracted patterns, also known

as Kikuchi patterns, are captured by the camera and subsequently transferred to computer software for indexing and analysis. The software enables the determination of crystal orientation and identification of the phases present in the sample [105].

The reason to tilt the sample in this method is to decrease the path length of the electrons which are backscattered by the lattice planes of the specimen. Therefore, these electrons can undergo the diffraction and escape from the sample before being absorbed. The macroscopic size of the sample for the characterization by EBSD is dependent on the ability of the SEM's stage and chamber to orient the specimen at 70° tilt, typically ranging from 5 to 30 mm [106].

EBSD method is limited to crystalline materials in which grain sizes are larger than several tens of nanometers in diameter. The specimen should be conductive and its surface should be free of deformation (which might be occurred in the preparation step), corrosion and contamination [107]. Electron backscatter diffraction (EBSD) analysis in this work was performed on a Zeiss Merlin field-emission-gun microscope working at 20 kV using a beam current of 10 nA. A Hikkari high-speed camera equipped with forward scatter diodes (FSDs) by EDAX was used for imaging the 70° tilted sample and acquiring of the Kikuchi-Patterns.

3.2 Produced materials

The high-purity alloys in this work were prepared by arc-melting as described earlier. The starting materials were metal pieces of Fe, Cr, Al and Y. The first three elements were 99.99% pure and Y was 99.9% pure and they were all obtained from Alfa Aesar GmbH & Co KG. Table 3 on the next page presents the list of the prepared alloys and their chemical compositions as determined by ICP-OES.

All the compositions in this work were in wt.% and the standard deviations for the measurements were also given. The obtained chemical analyses (see Table 3) agreed well with the expected nominal compositions. Two sets of alloys (A01 and A02) for Fe-16Cr-0.2Al with the same nominal composition were produced since more experiments were performed for this alloy, and therefore more cast materials were needed for this type of alloy. The chemical analyses were given for both sets of Fe-16Cr-0.2Al alloys and they did not show significant differences for Al and Cr contents (see again Table 3).

Table 3. Prepared alloys in this work and their chemical composition.

Alloy designation	Nominal composition (wt.%)				Chemical analysis (wt.%)			
	Y	Al	Cr	Fe	Y	Al	Cr	Fe
Fe-16Cr-0.5Al	-	0.5	16	83.5	-	0.451 ± 0.005	15.9 ± 0.05	83.2 ± 0.2
Fe-9Cr-0.5Al	-	0.5	9	90.5	-	0.429 ± 0.003	8.85 ± 0.07	90.3 ± 0.2
Fe-16Cr-0.2Al (A01)	-	0.2	16.0	83.8	-	0.202 ± 0.005	15.9 ± 0.1	83.5 ± 0.2
Fe-16Cr-0.2Al (A02)	-	0.2	16.0	83.8	-	0.207 ± 0.002	15.7 ± 0.03	82.5 ± 0.08
Fe-9Cr-0.2Al	-	0.2	9.0	90.8	-	0.210 ± 0.002	9.01 ± 0.07	91.1 ± 0.8
Fe-16Cr-0.2Al-0.05Y	0.05	0.2	16.0	83.75	0.0537 ± 0.0011	0.214 ± 0.002	15.8 ± 0.04	82.6 ± 0.1

The phase diagram of Fe-Cr system in the iron-rich side using Kjellqvist et al. [89] was calculated and shown in Fig. 8. The reason for the selection of Cr contents of alloys as 9 wt.% (0.09 weight fraction) and 16 wt.% (0.16 weight fraction) was to investigate both austenitic (fcc) and ferritic (bcc) steels at higher temperatures, respectively. The temperatures of all the experiments conducted in this work were equal to or higher than 1000 °C, which suggested that both austenitic and ferritic steels could be considered in the study (see Fig. 8).

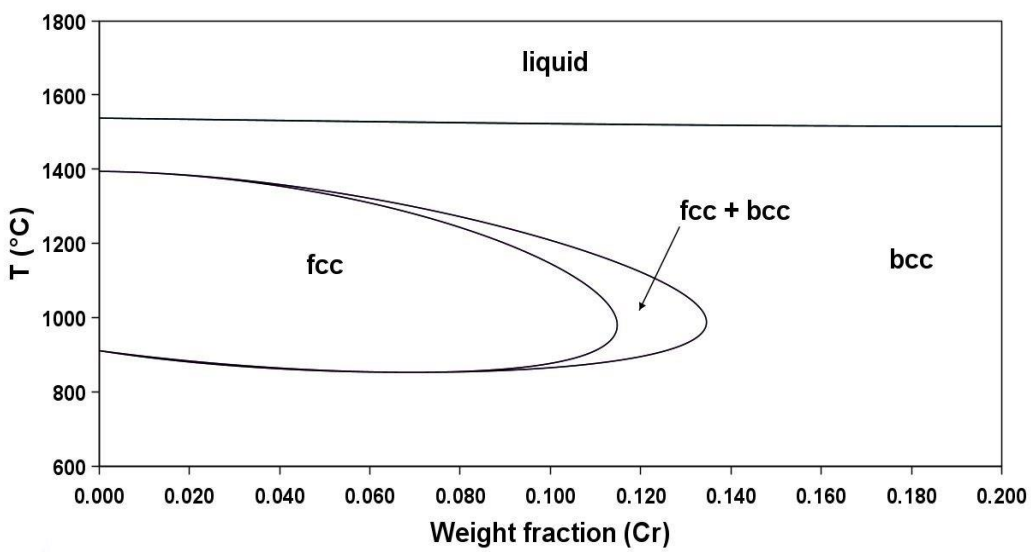

Fig. 8 Calculated Fe-Cr phase diagram in the iron-rich side using the database developed by Kjellqvist et al. [89].

The initial Al content (0.5 wt.%) was selected based on the concept that in conventional ODS steels, Y_2O_3 content was about 0.3 wt.% and to obtain theoretically equivalent content of Al_2O_3, the weight fractions of two oxides in the alloys needed to be equal. This can be written as:

$$W_{Al_2O_3} = W_{Y_2O_3} = 0.3\ \text{wt.}\% \tag{34}$$

$$W_{Al_2O_3} = 0.3\ \text{wt.}\% \rightarrow \quad W_{Al} = \alpha\, W_{Al_2O_3} \tag{35}$$

$$\alpha = \frac{2 \times \mathrm{M_{Al}}}{(2 \times \mathrm{M_{Al}}) + (3 \times \mathrm{M_O})} = \frac{2 \times 27}{(2 \times 27) + (3 \times 16)} = 0.53 \tag{36}$$

$$W_{Al_2O_3} = 0.3\ \text{wt.}\% \rightarrow \quad W_{Al} = 0.53 \times 0.3 = 0.16\ \text{wt.}\% \tag{37}$$

The required Al content to obtain ideally 0.3 wt.% Al_2O_3 was calculated to be 0.16 wt.%. To cast the first alloys in this work and by regarding losses during arc-melting process, Al content was taken nominally as 0.5 wt.%. By considering the same atomic fraction of Y_2O_3 and Al_2O_3 in ODS steels instead of weight fraction (0.3 wt.% Y_2O_3 was equivalent to 0.37 at.% Y_2O_3), the required Al content in the alloys would be 0.07 wt.% which was much less than 0.16 wt.%. Therefore, the mass fraction criterion as the basis for calculations was elected.

3.3 Oxidation experiment

The oxidation experiments in this work were performed in two sets. The following sections introduce two sets of experiments and their respective experimental procedures.

3.3.1 First set of experiments

In the first set of experiments, a single piece from each alloy (as-cast) weighing about 1 g was sealed in an evacuated quartz glass ampoule with a diameter of around 2 cm and a length of approximately 20 cm, together with the selected oxygen buffer systems (Cr/Cr_2O_3, Fe/FeO and V_2O/VO). The powder mixtures supplied required oxygen activities during oxidation process and hereafter the powder mixtures are referred to as oxygen buffer systems.

Fig. 9 illustrates the schematic representation of the experimental setup.

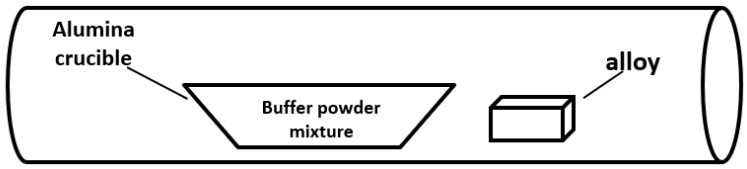

Fig. 9 The schematic illustration of the oxidation experiments in the first set of this work using evacuated and sealed quartz glass ampoule.

The selected oxygen buffer powders were mixed based on the weight ratio of the starting constituents (see Table 4). All the starting constituents for the buffers were in powder form. Cr powder, Cr_2O_3 powder, Fe powder, Fe_3O_4 powder, V powder and VO_2 powder were 99.95%, 99.97%, 99.998%, 99.997%, 99.5% and 99% pure, respectively and the powders were obtained from Alfa Aesar GmbH & Co KG.

Table 4. Buffer compositions for oxidation experiments in the first set of experiments.

No.	Equilibrium components of oxygen buffer mixture (at 1000 ˚C)	Provided oxygen activity at 1000 ˚C ($\log_{10} a_{O_2}$)	Equivalent oxygen partial pressure (p_{O_2} in bar)	Starting constituents of the buffers at room temperature	Weight ratio of the starting constituents	Total weight
1	Cr/Cr_2O_3	-21.8	1.61×10^{-22}	Cr/Cr_2O_3	1 : 1	1 g
2	Fe/FeO	–14.9	1.28×10^{-15}	Fe/Fe_3O_4	1 : 1	1 g
3	V_2O/VO	–24.5	3.20×10^{-25}	V/VO_2	1 : 1	1 g

The initial mole amounts of oxygen and metallic elements from starting constituents at room temperature for each experiment were then calculated. This is shown, for example for (Cr/Cr_2O_3) buffer as follows:

$$m_{Cr} = m_{Cr_2O_3} = 0.5\ g \tag{38}$$

$$M_{Cr} = 52\ g.mol^{-1} \rightarrow n_{Cr} = \frac{0.5}{52} = 0.0096\ mol \tag{39}$$

$$M_{Cr_2O_3} = 152\ g.mol^{-1} \rightarrow n_{Cr_2O_3} = \frac{0.5}{152} = 0.0033\ mol \tag{40}$$

$$n_{(Cr\ in\ Cr_2O_3)} = 2 \times n_{Cr_2O_3} = 2 \times 0.0033 = 0.0066\ mol \tag{41}$$

$$n_{Cr\ in\ (Cr/Cr_2O_3)} = n_{Cr} + n_{Cr\ in\ (Cr_2O_3)} = 0.0096 + 0.0066 = 0.0162\ mol \tag{42}$$

$$n_{(O\ in\ Cr_2O_3)} = 3 \times n_{Cr_2O_3} = 3 \times 0.0033 = \ 0.0099\, mol \quad (43)$$

According to the initial moles of Cr (0.0162 mol) and O (0.0099 mol), the equilibrium was then calculated at 1000 ˚C with Thermo-Calc software and the corresponding oxygen activity (a_{O_2}) and equivalent oxygen partial pressure (p_{O_2}) were then obtained and recorded in Table 4. The same strategy was then applied to the other buffer systems.

The specimens and buffer powder mixtures were kept separate to prevent them from coming into contact with each other. The buffer powder mixture was in an alumina boat (> 99.5% pure) and the alloy under examination on the bottom of the quartz glass ampoule was positioned. The sealed glass ampoules were then annealed at 1000 ˚C for 7 days in a muffle furnace. At the end of each experiment, the sealed glass ampoules were quenched in water to room temperature and then were broken to take the specimen out for further analyses.

3.3.2 Second set of experiments

The samples in the second set of experiments were wholly packed in a powder bed, made of a mixture of metal/oxide, using alumina crucibles. The specimens were in the form of small cubes with a few millimeters in size and a weight of approximately 1 g. Since they were in direct contact with powder mixtures, all the sides of the specimens before the experiments were ground up to grade # 4000 (SiC, Struers GmbH) to standardize the surface conditions.

The experiments in this set were conducted at elevated temperatures (1300 ˚C and 1450 ˚C) using either (V_2O/VO), (Cr/Cr_2O_3) or (VO/V_2O_3) powder mixtures in high temperature furnace (Nabertherm RHTV 120/300/18 furnace). The reason for carrying out the experiments at higher temperatures and putting the alloys in direct contact with buffer mixture and using no quartz glass ampoules, was to make the kinetics of the transport of oxygen from the buffer to the alloy faster. Moreover, a higher depth of internally oxidized zone might be obtained in shorter times. The heating rate of the furnace from room temperature to the final temperatures was fixed to approximately 4 ˚C/min.

The experimental setup for the second set of the experiments performed in this work is schematically presented in Fig. 10 (height: ca. 200 cm, width: ca. 15 cm).

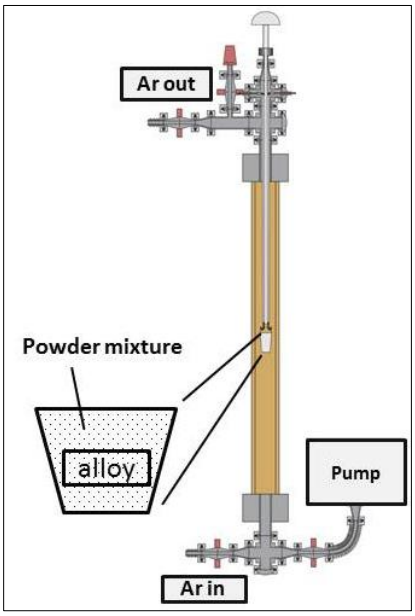

Fig. 10 The schematic illustration of the oxidation experiments in the second set of this work. In this set, a high temperature furnace under argon atmosphere was used. The alloy and power mixtures were in direct contact.

Similar to the first set of experiments (section 3.3.1), the equilibrium components, oxygen activities, and corresponding equivalent oxygen pressures were calculated using Thermo-Calc software for each experiment. This was done by inputting the initial mole amounts of oxygen and metallic elements from the starting constituents of buffers into the software. The calculations were performed for the temperatures of 1300 °C and 1450 °C. This is summarized in Table 5.

Table 5. Buffer compositions of the buffers for oxidation experiments in the second set of experiments.

No.	Equilibrium components of oxygen buffer mixture	T (°C)	Provided oxygen activity ($\log_{10} a_{O_2}$)	Equivalent oxygen partial pressure (p_{O_2} in bar)	Starting constituents	Weight ratio of the starting constituents	Total weight
4	V_2O / VO	1300	−18.7	2.02×10^{-19}	V / VO_2	1 : 1	2 g
5	Cr / Cr_2O_3	1300	−16.0	1.01×10^{-16}	Cr / Cr_2O_3	1 : 1	2 g
6	VO / V_2O_3	1300	−15.0	1.01×10^{-15}	V / VO_2	0.35 : 1	2 g
7&8	VO / V_2O_3	1450	−12.8	1.61×10^{-13}	V / VO_2	0.35 : 1	2 g

All the experiments in this set were performed under argon atmosphere (Ar 6.0) and it might be argued that calculated equivalent oxygen partial pressures of buffers (see equivalent oxygen partial pressures in Table 5) with the quality of the argon gas (purity of 99.9999%) contradicted. To comment on this issue, it had to be considered that oxygen did not constitute the whole impurities of argon gas and some other impurities like N_2, H_2O, H_2, … existed, and therefore partial oxygen pressure coming from contaminants was low. Additionally, the examined steels in the experiments were covered by a buffer mixture and this coverage protected the steels from being oxidized externally by oxygen originating from impurities in Ar 6.0. This issue was again argued and considered in chapter 4.

After the experiments, the specimens were cooled down to room temperature inside the furnace. The attached powders were then removed from the surface of the specimens by mechanical grinding. Table 6 summarizes the parameters of the oxidation experiments done in this work.

Table 6. The parameters of the oxidation experiments in this work.

Set of experiment	Experiment Number	Used oxygen buffer	Examined alloys	T (˚C)	Duration of annealing
set 1	1	Cr/Cr_2O_3	Fe-16Cr-0.5Al Fe-9Cr-0.5Al	1000	7 days (inside quartz glass, no contact between sample and buffer)
set 1	2	Fe / FeO	Fe-16Cr-0.2Al (A01) Fe- 9Cr-0.2Al	1000	7 days (inside quartz glass, no contact between sample and buffer)
set 1	3	V_2O / VO			
set 2	4	V_2O / VO	Fe-16Cr-0.2Al (A01)	1300	20 hours (sample in powder bed)
set 2	5	Cr / Cr_2O_3	Fe-16Cr-0.2Al (A02)	1300	
set 2	6	VO / V_2O_3	Fe-16Cr-0.2Al (A02)	1300	
set 2	7	VO / V_2O_3	Fe-16Cr-0.2Al (A02)	1450	
set 2	8	VO / V_2O_3	Fe-16Cr-0.2Al-0.05Y	1450	20 hours (sample in powder bed)

3.4 Mechanical testing

In order to evaluate the mechanical properties, tensile specimens for some selected alloys were prepared. The produced button from arc-melting (30 g) with flame (Fig. 11 a) was heated and forged with a hammer to make a coin-shaped sample. The coin-shape sample was then rasped to remove scales from the surface, and it was then cold-rolled to a final thickness of about 400 µm. These steps are shown in Fig. 11.

Fig. 11 The production route of sheet from as-cast button: (a) heating of the button with flame, (b) forging of the heated button to make a coin-shape sample, (c) rasping of the forged sample to remove the oxide scales from the surface, (d) the prepared sample for cold rolling, (e) the rolling of the sample, (f) further rolling of the sample to the desired thickness of ~ 400 µm for this work, (g) the obtained sheets after cutting to smaller parts.

The obtained sheet was used to make a tensile sample by YAG laser cutting machine (Carl Bassel Lasertechnik GmbH & Co. KG). The tensile specimens were directly embedded into buffer system (VO/V_2O_3) to be internally oxidized and the used setup for internal oxidation was a high temperature furnace as described in the previous section (see Fig. 10 in the section 3.3.2).

A typical tensile sample for mechanical testing is shown in Fig. 12.

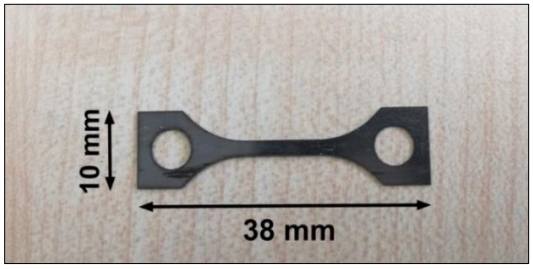

Fig. 12 The produced tensile sample from arc-melting buttons with a thickness of ~ 400 µm.

The internally oxidized sample was then examined for the stress-strain behavior. Zwick100 machine for the tensile tests was used and the test rate was fixed to 0.2 mm/min and all tests were performed at room temperature.

Chapter 4. Results and Discussion

The explanation and the discussion of the observed results with the help of the calculations were reported in this chapter. It encompassed the examination and analysis of microstructures in alloys after casting, as well as the investigation of oxidation experiments conducted in quartz glass ampoules and inside alumina crucibles using a vertical tube furnace. Various experiments were conducted under different oxidation conditions, which were optimized to obtain specific types of oxides relevant to the current research.

The thermodynamic calculations using the TCFE7 database [88] and simulated diffusion profiles by MOBFE2 [93] databases were also presented. The internal oxidation depths using classical Wagner's internal oxidation theory were calculated and compared to the experimentally obtained results. Furthermore, the tensile tests for the selected alloys were shown and the UTS values were compared to the ODS steels conventionally produced with the powder metallurgy.

4.1 As-cast alloys

The microstructures of as-cast alloys were observed with the SEM method in back-scattered (BSE) mode that shows z (atomic number) contrast and it seemed that no separate phases segregated. The alloys exhibited microstructures with large grain sizes, typically in the millimeter range. Considering that the as-cast alloys were scheduled for annealing at higher temperatures, the possible phases at those temperatures were calculated using Thermo-Calc software. This is shown later in this section.

The chemical compositions of as-cast alloys (Fe, Cr, and Al) were determined by the ICP-OES method, as mentioned in chapter 3 (see Table 3). The number of ICP-OES measurements was restricted to a maximum of three times per alloy since a double check of compositions with the EDX method was planned. EDX spot analyses within an area with dimensions of ca. $200\ \mu m \times 200\ \mu m$ for different regions of matrices were performed and did not show major differences for main elements.

Here four examples of quantitative results of EDX spot analyses of metallic elements for Fe-16Cr-0.2Al (A01) are shown in Table 7. The results for the impurities and a typical EDX spectrum of the analyses are provided in Appendix 7.

Table 7. EDX spot analyses of as-cast Fe-16Cr-0.2Al (A01) in different regions for metallic elements.

Spot Number	Al (wt.%)	Cr (wt.%)	Fe (wt.%)
01	0.27	15.84	81.23
02	0.27	16.00	81.00
03	0.21	15.70	80.89
04	0.29	15.89	80.19

The EDX spot analyses (see Table 7) and reported standard deviations after ICP-OES measurements (see again Table 3) led to the conclusion that homogeneous alloys after the casting process were obtained. The atomic distribution of aluminum, as oxide-forming element, was nearly the same in different spots of the sample which was necessary for internal oxidation.

The partial isothermal section of the Fe-Cr-Al system at the temperatures of the experiments, calculated using Thermo-Calc as described earlier, is shown in Fig. 13.

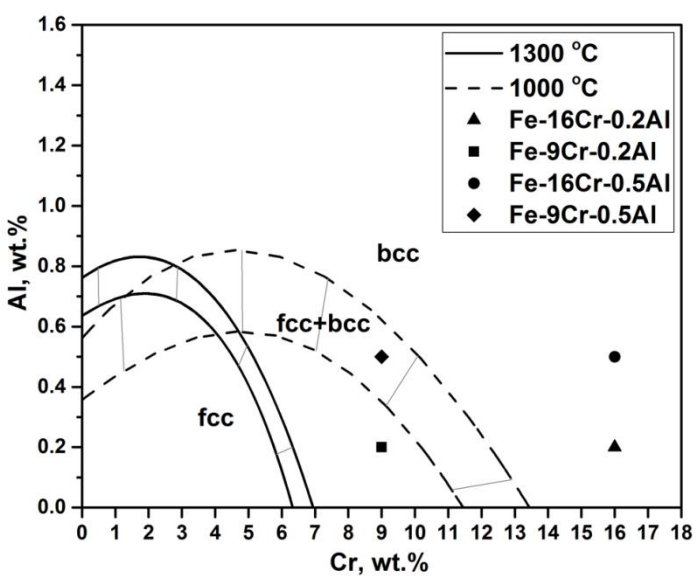

Fig. 13 Calculated partial isothermal section of Fe-Cr-Al system at 1000 ˚C and 1300 °C with alloy compositions indicated.

The calculated section (Fig. 13) revealed that both Fe-16Cr-0.5Al and Fe-16Cr-0.2Al had a single ferrite phase (bcc) at both temperatures (1000 °C and 1300 °C). Fe-9Cr-0.5Al had a dual-phase microstructure of ferrite and austenite (fcc) at 1000 °C, and a single-phase of ferrite at 1300 °C. In the case of Fe-9Cr-0.2Al, the stable phase at 1000 °C was austenite, while it was in the ferrite region at 1300 °C.

4.2 Oxidation in evacuated quartz glass ampoules

The first set of oxidation experiments for different steels were performed in quartz glass ampoules as earlier mentioned. This was done using three types of oxygen buffer systems (Cr/Cr_2O_3), (Fe/FeO), and (V_2O/VO) powder mixtures. In the following section, the observed results with (Cr/Cr_2O_3) oxygen buffer are presented.

4.2.1 Cr/Cr_2O_3 oxygen buffer results for Fe-16Cr-0.5Al and Fe-9Cr-0.5Al alloys

Two steel alloys (Fe-16Cr-0.5Al and Fe-9Cr-0.5Al) were annealed in the presence of (Cr/Cr_2O_3) oxygen buffer at 1000 ˚C for a duration of 7 days in an evacuated quartz glass ampoule. Subsequent SEM investigations confirmed the formation of particles within the matrices of both alloys, mainly along the grain boundaries.

This is shown in Fig. 14, where arrows were used to highlight the presence of particles.

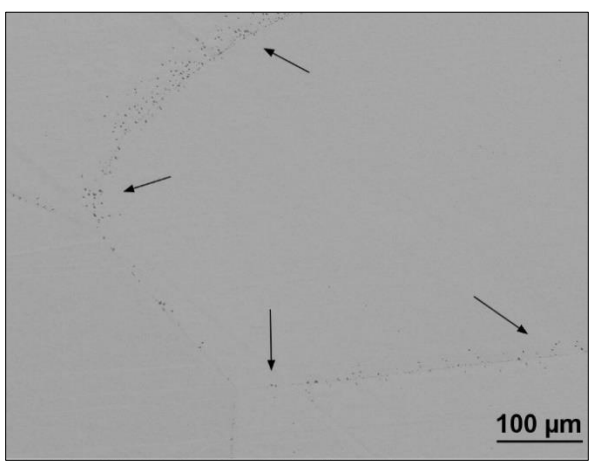

Fig. 14 Backscattered-micrograph of Fe-16Cr-0.5Al using SEM method after annealing at 1000 ˚C after 7 days with Cr/Cr_2O_3 buffer mixture. The arrows show the particles along the grain boundaries.

To argue why most of the particles were located along the grain boundaries, it should be considered generally, nuclei appear at points of high-lattice-strain energy such as grain boundaries [42]. Grain boundary diffusion becomes also important below about

0.75 to 0.8 T_m, where T_m is the melting temperature in Kelvin [108]. The diffusion along the grain boundaries was here dominant compared to the diffusion through the grains (T_m was about 1790 K). In the first step of analytical characterization, the EDX area measurements were performed in matrices of both as-cast and annealed alloys as well. The compositions in annealed alloys were determined in local regions within the matrix close to the formed particles. A typical selected area for EDX measurements is given in Fig. 15.

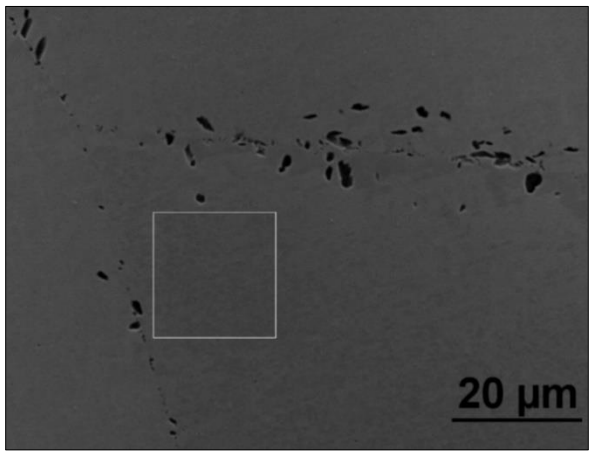

Fig. 15 A typical selected area for EDX area analysis shown by a white square (Fe-16Cr-0.5Al, annealed at 1000 ˚C for 7 days with the presence of Cr/Cr_2O_3 buffer mixture).

All the obtained EDX area analyses were compared regarding Al-fraction in the matrix. This was calculated to identify the possible deviations of Al-fraction in as-cast and annealed alloys. Al-fraction (Z) was defined by the following equation:

$$Z = \frac{Al\,[at.\%]}{Al\,[at.\%] + Cr\,[at.\%] + Fe\,[at.\%]} \qquad (44)$$

All attained Al-fraction values, their mean values, the box-whisker plot for each dataset and the normal distribution functions for as-cast and annealed alloys were plotted in one diagram and shown in Fig. 16. The mean values of as-cast and its annealed alloy were connected for the clarity of comparisons (e.g. compare as-cast Fe-16Cr-0.5Al with annealed Fe-16Cr-0.5Al in Fig. 16).

The calculated Z values for Fe-16Cr-0.5Al alloy after annealing showed a greater scattering range (Max. - Min. = 0.0055) than Fe-9Cr-0.5Al after annealing (0.0035). This might be explained that three measurements for Fe-16Cr-0.5Al after annealing were in

closer areas to the precipitates. Therefore, higher Z values were obtained for these three measurements, and a higher scattering range was then recorded (see again the measured points of Fe-16Cr-0.5Al after annealing in Fig. 16).

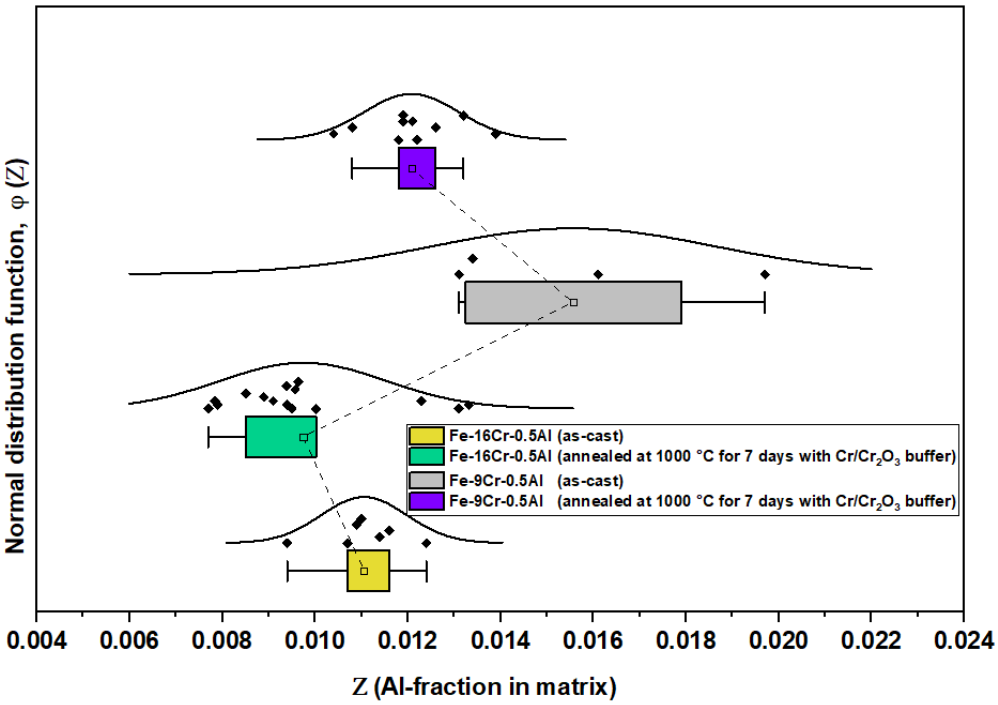

Fig. 16 Al-fraction values, their box-whisker-plot and the normal distribution for as-cast and annealed alloys.

According to EDX analyses of the matrix (Fig. 16), the Al-fractions in the matrices of both annealed alloys with the presence of Cr/Cr_2O_3 buffer reduced compared to the Al-ratio in as-cast alloys. After this analytical approach, it was interpreted that the obtained particles were enriched in Al compared to the matrix.

In the next step of characterization for the particles, one TEM sample from Fe-16Cr-0.5Al alloy was prepared and the compositional analysis of the particles using STEM mode combined with EDX detector was done. One particle in high-angle annular dark-field (HAADF) mode with a typical elemental distribution profile (EDX line scan) along an indicated path is shown in Fig. 17.

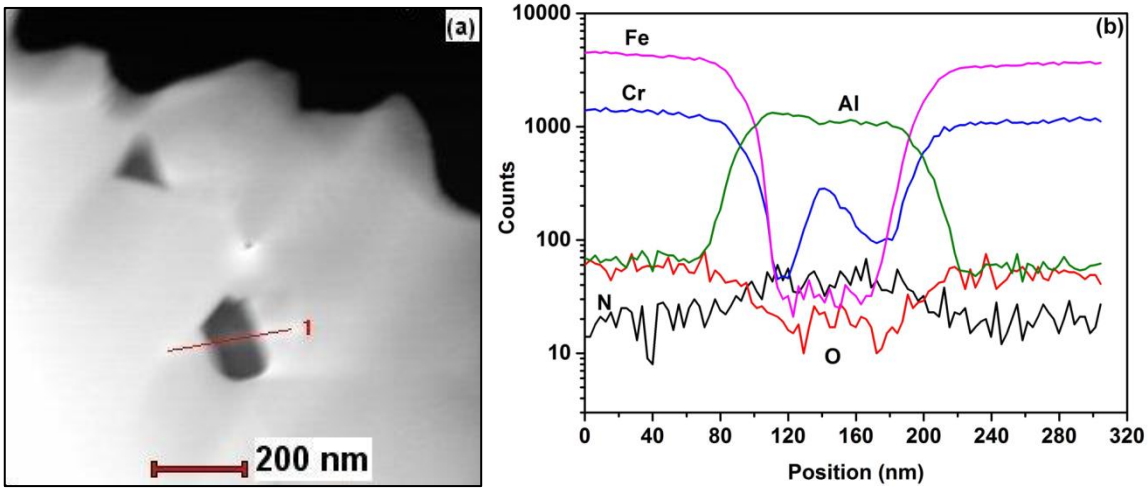

Fig. 17 The investigation of Fe-16Cr-0.5Al alloy annealed with presence of Cr/Cr_2O_3 buffer mixture at 1000 ˚C after 7 days inside quartz glass ampoule: (a) A typical particle (HAADF image), (b) its elemental distribution profile along the indicated line.

Al counts were higher in the middle of the particle than in the surrounding matrix, whereas Fe and Cr profiles revealed a decrease in the number of counts relative to the matrix (Fig. 17 b). Cr level in the middle of the examined particle showed an increase and the possibility of Cr presence in the particles has been argued later in this section. A relatively higher level of N counts than O counts was seen. However, the absolute number of counts of N and O were relatively low.

The reason for presenting the EDX results for particles in counts rather than atomic or weight percentage was the presence of low atomic number elements (O and N) and to prevent potential misinterpretations. This approach for particles was adopted in this study, and only the results in counts for particles were provided. The typical EDX results after TEM observation suggested that more detailed analyses were needed to provide comments on the generated particles. It is important to note that, initially, elucidating the composition of particles was a priority, and as a result, methods like SAED (selected area electron diffraction) in TEM were not employed for these particles.

An individual elemental mapping with a SEM microscope was carried out to facilitate further compositional analyses. The elemental mappings (Fig. 18) were performed using a Zeiss Merlin FEG-SEM equipped with an EDAX Apollo Super SDD detector. A resolution of 512x400 pixel was chosen for the mappings with a dwell time of 500 µs and 64 total frames.

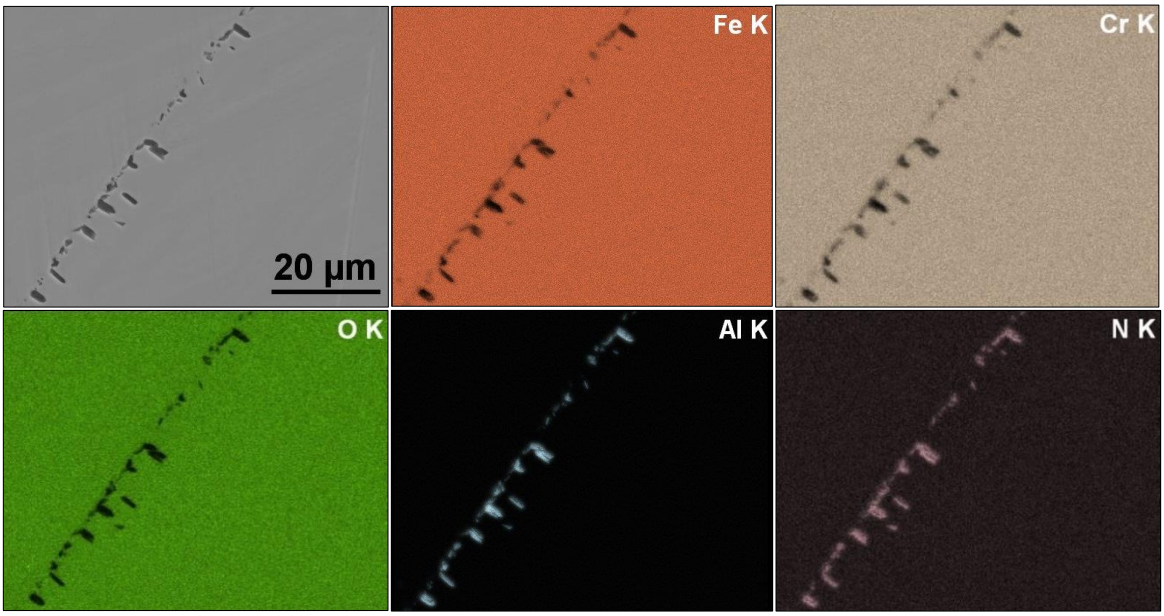

Fig. 18 A typical individual elemental distribution maps for Fe, Cr, O, Al and N found in Fe-16Cr-0.5Al alloy annealed with presence of Cr/Cr_2O_3 buffer mixture at 1000 ˚C after 7 days inside quartz glass ampoule.

The obtained mapping (Fig. 18) illustrated the depletion of Fe, Cr and O in the formed particles compared to the matrix; meanwhile there was an enrichment of Al and N in those particles. This underlined that most of the particles were AlN-based rather than Al_2O_3-based, contrary to the earlier expectation. A further investigation of the other alloy (Fe-9Cr-0.5Al) by SEM and TEM revealed similar results with the formation of AlN-based particles.

The nucleation of AlN in steel is typically challenging unless specific thermal or mechanical treatments are employed to enhance the precipitation. The formation of AlN is influenced by various factors, including the structure and composition of the steel matrix, temperature, duration of exposure, and cooling rate [109].

The Gibbs energy of formation of AlN (kJ/mol N_2) and Al_2O_3 (kJ/mol O_2) from the pure element at different temperatures in binary systems (Al-N and Al-O) were calculated and shown in Fig. 19. Based on this information, it could be concluded that the formation of oxide was more favored than the nitride formation.

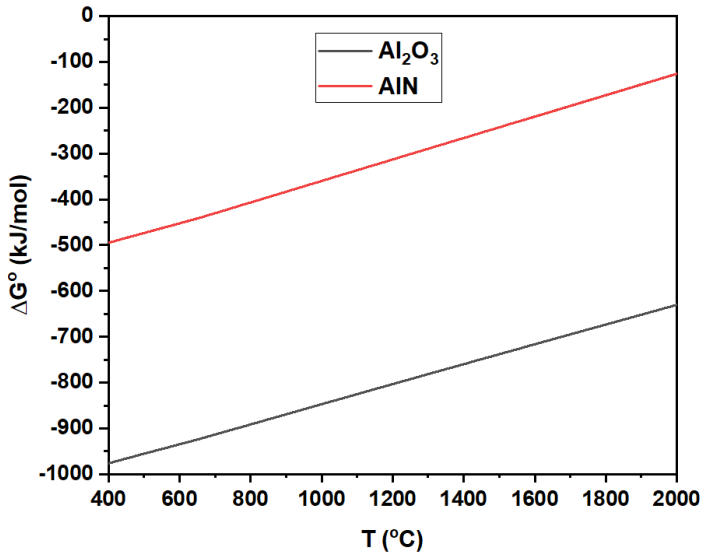

Fig. 19 The calculated standard Gibbs energy of formation of AlN (kJ/mol N_2) and Al_2O_3 (kJ/mol O_2) using TCBIN database [90].

An in-depth study was initiated to investigate the origin of the formation of AlN particles within the examined alloys, aiming to explore the underlying reasons for this observation. The likely explanations for this phenomenon could be categorized into two possibilities:

1. One possibility was the diffusion of nitrogen through the quartz glass during the 7 days of annealing. The dissolved nitrogen in the matrix of alloy could react to aluminum, leading to the formation of AlN particles.
2. Another possibility was that nitrogen originated from the oxygen buffer system itself and contaminated the alloy during the annealing process.

To clarify this issue, a specimen from the Fe-16Cr-0.5Al alloy was placed inside an evacuated quartz glass ampoule and annealed at a temperature of 1000 °C for 7 days. Unlike the previous experiments, this particular experiment was conducted without the use of any oxygen buffer. The specimen and other experimental conditions remained the same as those used in the experiments with the oxygen buffer system. By comparing the results of this experiment to the previous ones, the contribution of nitrogen from the oxygen buffer system could be assessed.

The microstructure of the alloy (Fe-16Cr-0.5Al) after annealing with SEM was investigated and a single-phase structure without nitride particles was seen (Fig. 20).

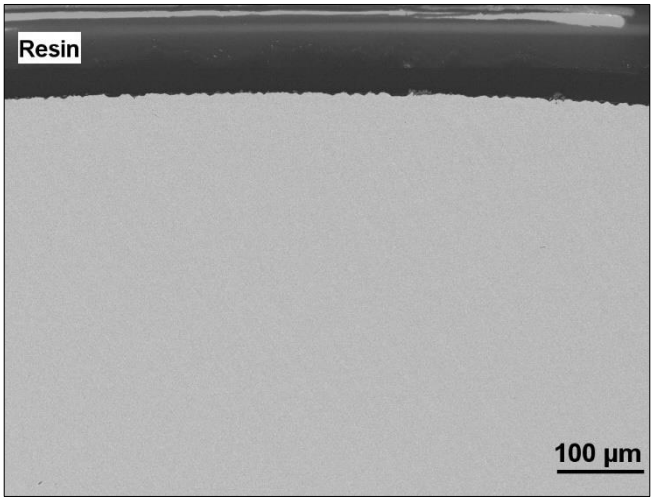

Fig. 20 Cross-section backscattered-micrograph of Fe-16Cr-0.5Al using SEM method after annealing at 1000 ˚C after 7 days inside evacuated quartz glass. No oxygen buffer system was used. The formation of AlN was not seen.

The chemical composition of the specimen after annealing with and without the presence of oxygen buffer system (Cr/Cr_2O_3), was figured out by ICP-OES and CGHE methods and shown in Table 8. The chemical analysis of N in Fe-16Cr-0.5Al alloy annealed at 1000 ˚C for 7 days with the presence of (Cr/Cr_2O_3) buffer was reported after one measurement because of the lack of extra samples for further measurements. Therefore, no standard deviation was available for this analysis.

Table 8. The comparison of the chemical composition of the annealed alloy (Fe-16Cr-0.5Al) with and without oxygen buffer system (including reported standard deviations).

Description	Chemical analysis (wt.%)				
	CGHE		ICP-OES		
	O	N	Al	Cr	Fe
Fe-16Cr-0.5Al (after annealing at 1000˚C for 7 days with the presence of Cr/Cr_2O_3 buffer)	0.0194 ± 0.0065	0.011	0.385 ± 0.001	16.8 ± 0.03	81.9 ± 0.50
Fe-16Cr-0.5Al: (after annealing at 1000˚C for 7 days without oxygen buffer system)	0.010 ± 0.006	0.0019 ± 0.002	0.353 ± 0.006	15.8 ± 0.02	83.0 ± 0.09

The nitrogen content of annealed alloy with (Cr/Cr_2O_3) buffer was greater than the nitrogen content of annealed alloy without the presence of buffer system (0.0110 wt.% compared to 0.0019 wt.% nitrogen, respectively). This inspection could remark that the first assumption (nitrogen diffusion through the quartz glass) as the cause of AlN formation was unlikely. The nitrogen content of both constituents of the used buffer system (Cr and Cr_2O_3 powder) measured with CGHE method is shown in Table 9.

Table 9. The nitrogen content measured by CGHE method for Cr and Cr_2O_3 powder.

	Cr powder	Cr_2O_3 powder
N in wt.%	< 0.0007	0.0224 ± 0.0009

Cr powder had a negligible amount of nitrogen and therefore Cr powder could not cause a major source of contamination to the alloys. Cr_2O_3 powder had a relatively higher amount of nitrogen, which could explain the source of contamination. To evaluate the sensitivity of Fe-Cr-Al system in the iron-rich side of the phase diagram to the presence of oxygen and especially nitrogen in trace values, an isothermal section for this system with five elements (Fe-Cr-Al-O-N) was calculated. This was done to obtain the stability fields for AlN or Al_2O_3 corundum. The chromium and aluminum content of the system was fixed to the measured values for the alloy which was determined after experiment with (Cr/Cr_2O_3) system by ICP-EOS method: $W_{Cr} = 16.8\ \text{wt.}\%$, $W_{Al} = 0.385\ \text{wt.}\%$ (see Table 8 again). The partial isothermal section for this system was calculated at 1000 ˚C and shown in Fig. 21.

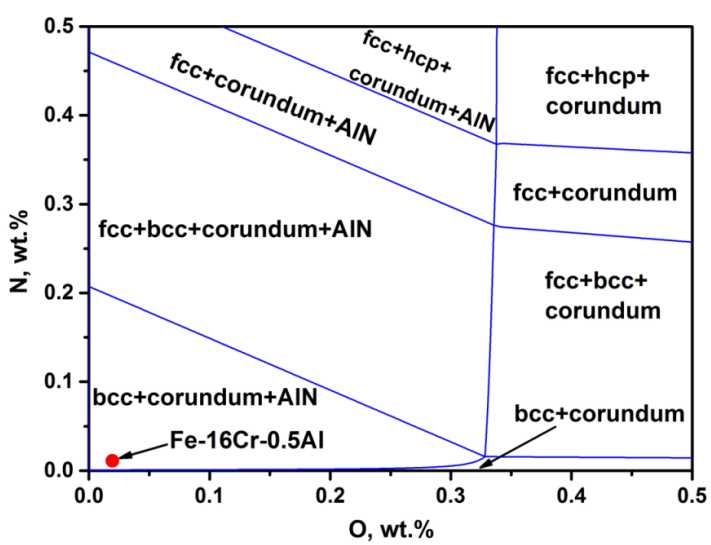

Fig. 21 Calculated partial isothermal section of Fe-Cr-Al-O-N system at 1000 ˚C. The Cr and Al contents of the system were fixed to 16.8 wt.% and 0.385 wt.%, respectively.

The calculated phase diagram was a partial isothermal section in the iron-rich side with up to 0.5 wt.% for oxygen and nitrogen. Each region stood for the thermodynamically stable phases that could be formed at certain ranges of oxygen and nitrogen. Corundum, bcc, fcc, AlN and hcp in Fig. 21 could be, for simplicity, described as $(Al,Cr)_2O_3$, ferrite, austenite, AlN-base phase and Cr_2N-based phase, respectively. In trace values of nitrogen, AlN-phase (an undesirable phase) and Al_2O_3 corundum could be formed (the left-hand side of Fig. 21). The desirable aim for this work was to shift the alloy to the right-hand side of the diagram and this meant that the region of (bcc+corundum) was the region of interest for this work. The location of the alloy (Fe-16Cr-0.5Al) was shown in Fig. 21 as well. The equivalent activity of oxygen and nitrogen at this point is given in Table 10. The values were calculated with the TCFE7 database [88].

Table 10. The oxygen and nitrogen activity for Fe-16Cr-0.5Al alloy, in which the phases of AlN and Al_2O_3 and ferrite were in equilibrium with each other at 1000 ˚C.

Oxygen activity at 1000 ˚C ($\log_{10} a_{O_2}$)	Equivalent oxygen partial pressure (p_{O_2} in bar)	Nitrogen activity at 1000 ˚C ($\log_{10} a_{N_2}$)	Equivalent nitrogen partial pressure (p_{N_2} in bar)
-27.8	1.61×10^{-28}	-4.3	5.08×10^{-5}

The formation of AlN at such a low activity of nitrogen as shown in Table 10, was a certain issue in this system. The formation of hcp (Cr_2N-based phase) had an incredibly low chance for the examined alloy (see Fig. 21 again) but a few particles could show the formation of this phase like the one seen and reported in Fig. 17. At the surface of the alloy, higher solubility of N in the alloy could occur and the particle shown in Fig. 17 might fulfill the formation of hcp (Cr_2N-based phase) as well, but most of the particles as thermodynamic modelling (Fig. 21) and elemental mapping analyses (Fig. 18) suggested, were AlN-based particles. Based on the thermodynamic calculations conducted, two strategies were identified to mitigate the formation of the AlN phase:

1. The reduction of the aluminum content of the alloy would decrease the chance of AlN formation. This was obtained by calculation of the partial isothermal section

of Fe-Cr-Al-O-N system at 1000 ˚C up to 0.5 wt.% oxygen and nitrogen. The Cr and Al contents of the system were fixed to 16.8 wt.% and 0.2 wt.%, respectively. In Fig. 22, the undesirable three-phase region of 'bcc+corundum+AlN' became smaller and the region of interest 'bcc+corundum' expanded to the left side of the diagram. (compare Fig. 21 and Fig. 22).

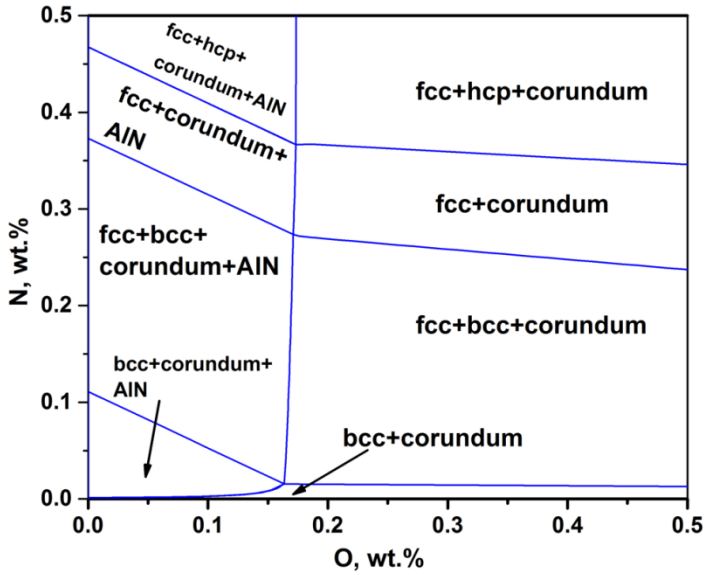

Fig. 22 Calculated partial isothermal section of Fe-Cr-Al-O-N system at 1000 ˚C. The Cr and Al contents of the system were fixed to 16.8 wt.% and 0.2 wt.%, respectively.

2. The second strategy could be the usage of higher oxygen partial pressures, i.e. the oxygen activities for the experiments. Since this experiment was done by Cr/Cr_2O_3 buffer system, an alternative buffer system with a higher oxygen activity than Cr/Cr_2O_3 equilibrium line would be the equilibrium line Fe/FeO. Referring to the Ellingham diagram in chapter 2, the Fe/FeO buffer exhibited an oxygen activity of $10^{-14.9}$ at this temperature (1000 ˚C). Notably, this value was approximately 10^7 times higher than the oxygen activity provided by the Cr/Cr_2O_3 buffer system. The number of O_2 molecules (here denoted as N_{O_2}) in one liter ($0.001\ m^3$) at 1000 ˚C with oxygen partial pressure of 1.61×10^{-22} bar (provided by Cr/Cr_2O_3 buffer system and extracted from Ellingham diagram) by considering an ideal gas behavior could be written theoretically as:

$$p_{O_2} = 1.61 \times 10^{-22}\ bar \quad (45)$$

$$V = 0.001\ m^3 \quad (46)$$

$$T = 1273.15\ K \quad (47)$$

$$pV = nRT \ \rightarrow \ n_{O_2} = 1.5 \times 10^{-24}\ \ mol \quad (48)$$

$$N_{O_2} < 1 \quad (49)$$

The theoretical calculated number of O_2 molecules was found to be less than one molecule. This revealed that this buffer system was not a proper and practical candidate for internal oxidation experiments. (The quartz glass ampoule volume was less than one liter).

Following the observations of the results obtained with Cr/Cr_2O_3 for Fe-16Cr-0.5Al and Fe-9Cr-0.5Al alloys, the experiments were then modified and the results given in the subsequent section.

4.2.2 Fe/FeO oxygen buffer results for Fe-16Cr-0.2Al and Fe-9Cr-0.2Al alloys

According to the strategies highlighted in the previous section (4.2.1), further experiments were then planned. The experiments were performed by producing the alloys containing 0.2 wt.% Al and using Fe/FeO buffer system for the internal oxidation. The oxidation result for Fe-16Cr-0.2Al (A01) at 1000 ˚C for 7 days in the presence this buffer inside the quartz glass ampoule is illustrated in Fig. 23.

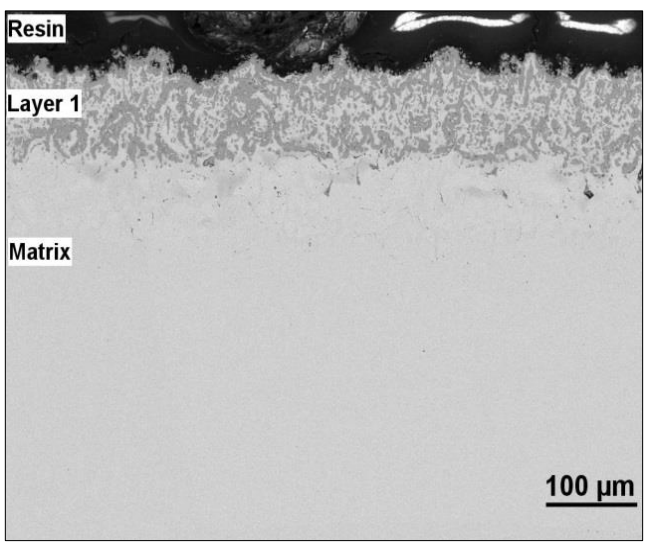

Fig. 23 Cross-section backscattered-micrograph of Fe-16Cr-0.2Al (A01) using SEM method after oxidation at 1000 ˚C after 7 days in presence of Fe/FeO buffer mixture.

In this specimen, the formation of an external scale referred as “Layer 1” with about 130 µm thickness in the outer regions of the sample was observed (Fig. 23). Only a

single zone of external oxidation was here formed, and no internal oxidation zone was detected. The external scale in this alloy could be potentially predicted as one of the following oxides:

1. Only Fe-O layer or Fe/Cr oxide layers (a non-protective oxide scale in iron alloys)
2. External protective chromia-based scale (Cr_2O_3) or mixed chromia-alumina scale (Cr_2O_3-Al_2O_3)
3. Only alumina external oxide layer (Al_2O_3)

The formation of an external Fe-O, Fe/Cr oxide layer or only Cr_2O_3 scale (Cr_2O_3-Al_2O_3 mixed scale) could occur (assumption 1 and 2), but the formation of an alumina external oxide layer was not possible (assumption 3). Since Al concentration in the examined alloy was exceptionally low (0.2 wt.%), the formation of a continuous and external layer consisting only Al_2O_3 oxides was not reasonable. The formation of Al_2O_3 protective scale typically needed the addition of 4-6 wt.% aluminum in steel [110]. Jozaghi et al. [111] calculated that at least about 7 wt.% Al was needed to build an alumina scale in Fe-16Cr alloy. According to this fundamental, 0.2 wt.% Al could not clearly fulfill the minimum critical amount of Al to form a protective alumina scale. To assess the oxide scale, a higher magnification image of “Layer 1” and a EDX line scan for a selected path in this layer were done (Fig. 24).

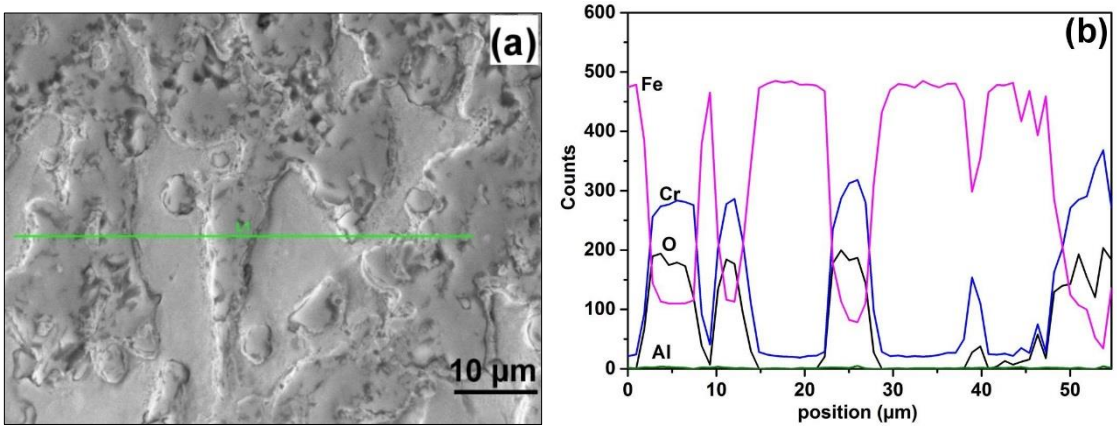

Fig. 24 EDX analysis of Fe-16Cr-0.2Al (A01) after oxidation at 1000 ˚C after 7 days in presence of Fe/FeO buffer: (a) A higher magnification of the scale formed via secondary electrons-micrograph and indicated path for line scan, (b) the corresponding composition profile.

The line scan profile for elements (Fig. 24) suggested that the formed scales were enriched in Fe, Cr and O and this revealed the formation of Fe/Cr oxide phase in

Layer 1 and not the formation of Cr-O or Cr-Al-O based scale. In addition, according to Jozaghi et al. [111] the minimum Cr content to form Cr_2O_3 or Cr_2O_3-Al_2O_3 protective scale for an alloy of Fe-0.2Al was about 32 wt.% and not 16 wt.%. This result and EDX observations could appraise that the first assumption (the formation of Fe/Cr oxide layer) was valid. The result for the same experimental conditions for Fe-9Cr-0.2Al alloys is shown in Fig. 25.

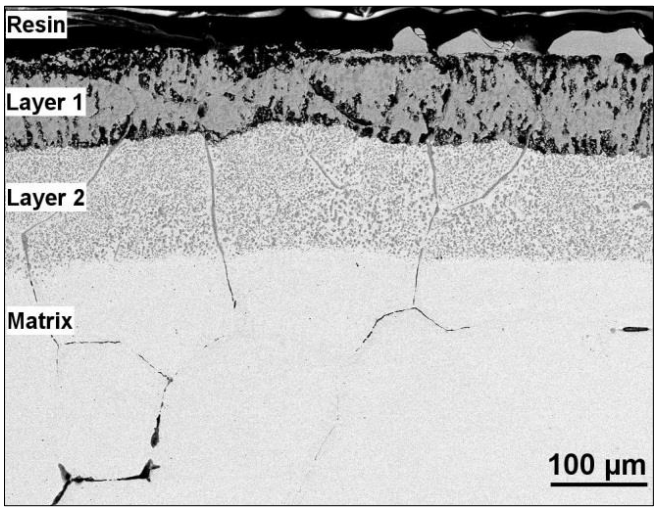

Fig. 25 Cross-section backscattered-micrograph of Fe-9Cr-0.2Al using SEM method after oxidation at 1000 ˚C after 7 days using Fe/FeO buffer.

Two separate layers (Layer 1 with approximately 120 µm thickness and Layer 2 with about 130 µm thickness) in the outer areas of the sample were detected (Fig. 25). The three assumptions mentioned above (for Fe-16Cr-0.2Al) could be hypothesized to predict the type of Layer 1 in Fig. 25 for Fe-9Cr-0.2Al:

1. Only Fe-O layer or Fe/Cr oxide layers (a non-protective oxide scale in iron alloys)
2. External protective chromia based scale (Cr_2O_3) or mixed chromia-alumina scale (Cr_2O_3-Al_2O_3)
3. Only alumina external oxide layer (Al_2O_3)

The second and third assumptions could be questionable, since Cr and Al contents in Fe-9Cr-0.2Al did not satisfy the minimum required values, as stated above for Fe-16Cr-0.2Al. The formation of Fe-O or Fe/Cr oxide scale in Layer 1 could be hence interpreted. To argue why two separate oxide layers were formed here, it must be noted

that the inward diffusion of oxygen was decelerated (because of the existence of Layer 1) and therefore a zone of internal oxidation was obtained in Layer 2.

The possible oxides in Layer 2 could be categorized as:

1. Internal oxidation zone of Fe-O or Fe/Cr oxide particles
2. Internal oxidation zone consisting of Cr-O, Cr-Al-O or Al-O particles

To analyze the possible oxides in Layer 1 and 2 quantitatively, an obtained EDX line scan for a path from “Layer 1” towards “Matrix” for this sample was recorded and shown in Fig. 26.

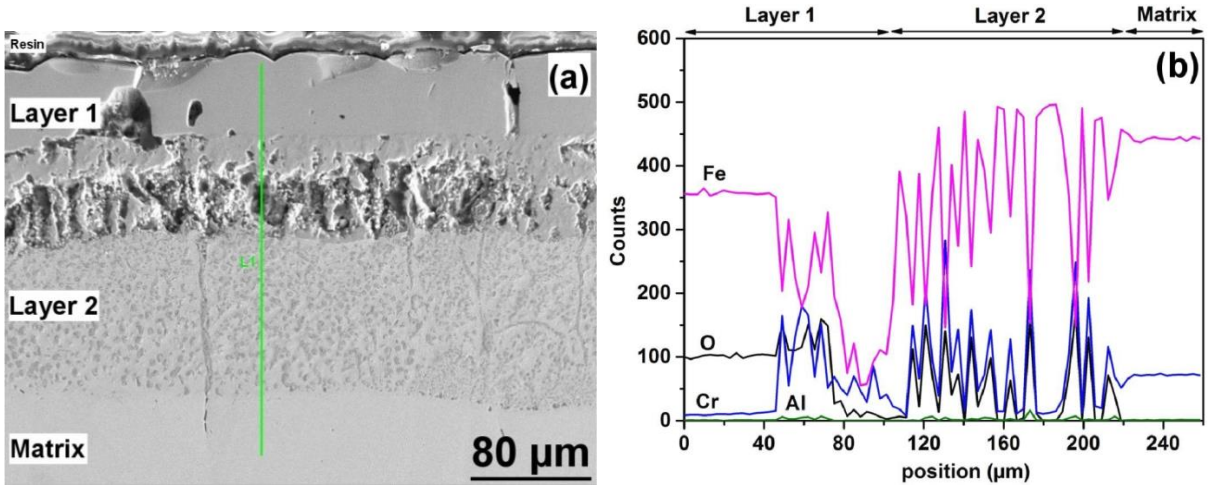

Fig. 26 EDX analysis of Fe-9Cr-0.2Al after oxidation at 1000 ˚C after 7 days in presence of Fe/FeO buffer: (a) Cross-section secondary electrons-micrograph showing the formation of two layers in outer regions and indicated path for line scan, (b) the corresponding composition profile.

The EDX line scan profile (Fig. 26 b) suggested the formation of Fe/O scale in layer 1. In this layer, the counts for Fe and O up to about 45 µm were clearly visible (see Fig. 26 b again). The outer scale (layer 1) seemed to be spalled in some spots, leading to a reduction in the number of counts above 45 µm up to 115 µm in these spots (see Fig. 26 b). The spallation of the outer scale could come from the metallographic preparation of the samples. In layer 2 (from the positions above about 115 µm up to about 220 µm in Fig. 26 b), Fe/Cr oxide particles were precipitated from the alloy, i.e. a zone of internal oxidation was present in layer 2. The positions above about 220 µm showed the simple Fe-Cr matrix with almost stable Fe and Cr counts. According to the EDX observations, it could be concluded that assumptions 1 regarding the presence of Fe/Cr oxides in Layer 1 and Layer 2 were confirmed.

After these experimental observations, the thermodynamic equilibria calculations were executed. The partial isothermal section in the system of Fe-Cr-Al-O at 1000 ˚C with a fixed oxygen activity ($10^{-14.9}$) provided by the buffer (Fe/FeO) was then calculated and shown in Fig. 27. In a narrow region at the bottom of the phase diagram, FeO phase (wustite) was present. The molar fraction of oxygen in wustite at 9 and 16 wt.% Cr was calculated using Thermo-Calc software and recorded as 1.079. Wustite could be represented by the formula of $Fe_{1-x}O$ (i.e. x = 0.073 for both alloys), since it was deficient in iron. The compositional formula ($Fe_{1-x}O$) might not reflect the structural complexities of iron monoxide and therefore a more representative formula for wustite could be noted as $(Fe^{2+}_{1-3x}\ Fe^{3+}_{2x}\ \square_x)\ O^{2-}$ in which two valence states of iron (Fe^{+2} and Fe^{+3}) were considered as well (□ stands here for vacancies) [112]. After this supplementary description of wustite, hereafter only the stoichiometric formula of FeO was used to designate wustite in the shown phase diagrams for simplicity.

In the left corner of the phase diagram, a three-phase region consisting of FeO (wustite), $(Fe,Cr,Al)_3O_4$ and $(Al,Cr,Fe)_3O_4$ existed. In the right corner, two phases of $(Al,Cr)_2O_3$ and $(Fe,Cr,Al)_3O_4$ were in equilibrium with each other. Some tie-lines were illustrated for the two-phase region of FeO and $(Fe,Cr,Al)_3O_4$.

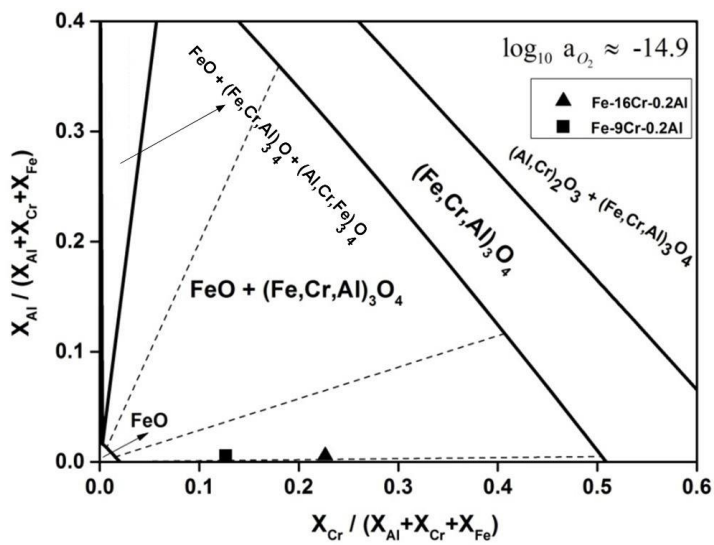

Fig. 27 Calculated partial isothermal section of the system Fe-Cr-Al-O under the oxygen activity of $10^{-14.9}$ at 1000 ˚C with alloy compositions indicated.

Thermodynamic modelling (Fig. 27) revealed the formation of FeO and $(Fe,Cr,Al)_3O_4$ (spinel) for both examined alloys. The formation of “Fe/Cr oxide phase” was seen in

both cases (in Fig. 24 as scale and in Fig. 26 as precipitated zone or layer 2). The formation of FeO in Fe-9Cr-0.2Al was detected as well (in Fig. 26 as layer 1). However, FeO in Fe-16Cr-0.2Al was not detected. This could be referred to the point that the oxidation time was insufficient for forming a separate layer of iron-oxide (Fe/O) phase in this alloy. In the work of Zurek et al. (2011) [113], the oxidation behavior of similar steel (Fe-10Cr) during exposure to Ar-4%H_2-2%H_2O was reported and Fe-Cr-Al alloys could be very similar to Fe-Cr alloys when the Al concentration kept very low. The calculated oxygen activity for the oxidizing medium, shown as $\log(p_{O_2}/bar)$, was given in their work (Fig. 28). Ar-4%H_2-2%H_2O, as a low O_2 holding gas, gave an oxygen activity of $10^{-15.3}$ in Fig. 28 which was comparable with the oxygen activity obtained with the buffer system Fe/FeO used in the current work ($10^{-14.9}$).

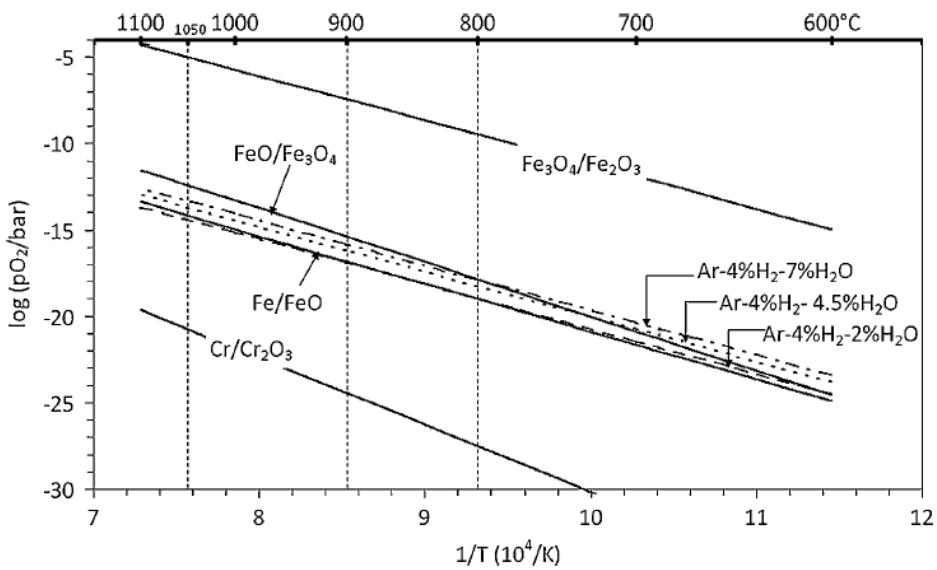

Fig. 28 The equilibrium oxygen activity for the exposure atmospheres and relevant oxides in the work of Zurek et al. (2011) [113].

Zurek et al. [113] concluded that at and above 900 ˚C, the internally oxidized chromium prevails in form of Fe/Cr spinel, aligning with the observed results in this work. The buffer of (Fe/FeO) provided an oxygen activity of $10^{-14.9}$ and caused an undesirable type of oxidation in both investigated alloys. Applying a higher oxygen activity than $10^{-14.9}$ could result in more severe oxidation in examined alloys which was against the aim of this work (refer again to Fig. 23 and Fig. 25 for external oxide layers). The change in the used buffer and the applied oxygen activity was therefore essential. The newly examined buffer system could be (V_2O/VO) powder mixture.

4.2.3 V_2O/VO oxygen buffer results for Fe-16Cr-0.2Al and Fe-9Cr-0.2Al alloys

The oxidation results with the presence of the new mixed oxide buffer system (V_2O/VO) for both alloys inside the quartz glass ampoule under the same conditions (at 1000 ˚C for 7 days) were presented in this section. The experiment conditions were maintained to be identical to those of the experiment with (Fe/FeO) buffer system to ensure the comparability of results. The results for Fe-16Cr-0.2Al (A01) is shown in Fig. 29.

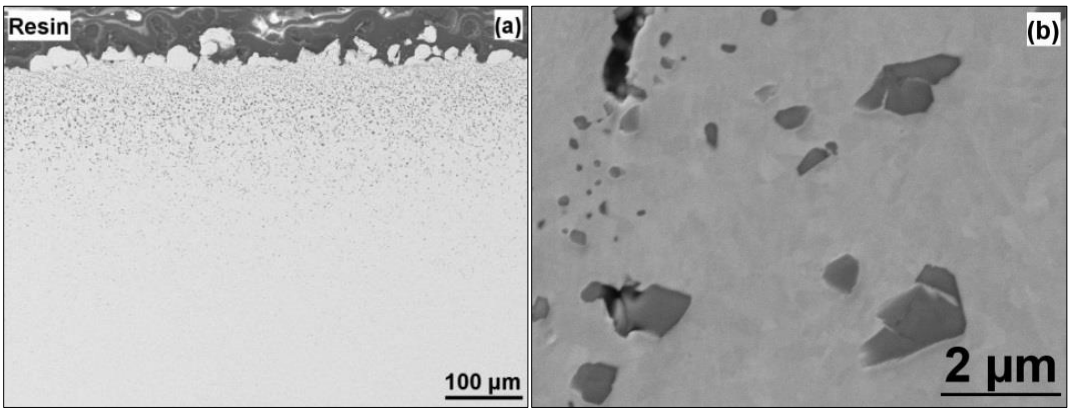

Fig. 29 The oxidation result of Fe-16Cr-0.2Al (A01) at 1000 ˚C after 7 days in presence of V_2O/VO oxygen buffer: (a) Cross-section backscattered-micrograph in outer regions (SEM method), (b) secondary electrons-micrograph, a higher magnification image showed the formed particles (SEM method).

An external scale was not found here and a zone of discrete precipitates in the outer areas of the sample with a thickness of approximately 250 µm was detected (Fig. 29 a). The maximum size of particles was about a few micrometers (Fig. 29 b). An EDX line scan profile for a particle is shown in Fig. 30.

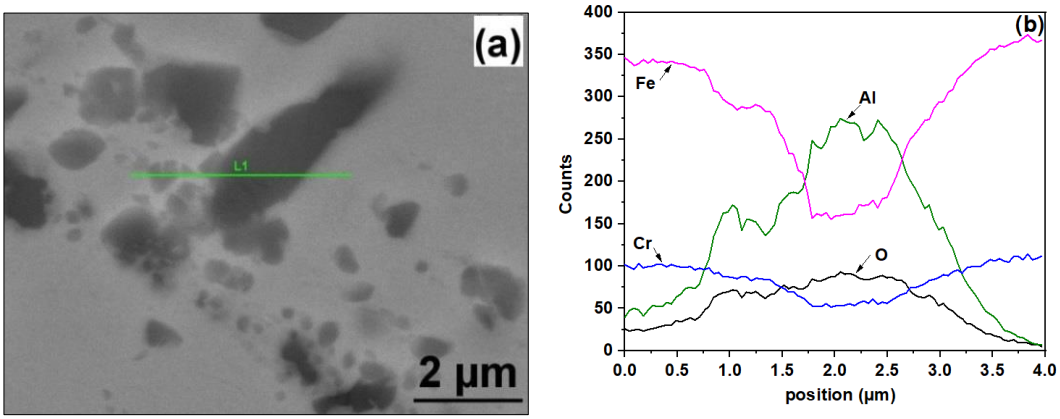

Fig. 30 EDX analysis for the formed particles in Fe-16Cr-0.2Al (A01) at 1000 ˚C after 7 days in presence of V_2O/VO oxygen buffer: (a) Secondary electrons-micrograph and indicated path for line scan (SEM method), (b) the corresponding composition profile.

As the line scan profile showed, the formed particles had compositional enrichment in Al and O (in Fig. 30). The number of counts for Fe and Cr in the middle of path did not reach to zero. This could be attributed to the small size of particles and the effect of matrix on the recorded counts. The oxygen buffer system of (V_2O/VO) for this experiment provided an oxygen activity of $10^{-24.5}$ which was lower than the oxygen activity of $10^{-21.8}$ provided with (Cr/Cr_2O_3). Therefore, the oxide phase which formed here was expected to be Al_2O_3-based corundum with a negligible Cr content (see again Table 4 in chapter 3 for provided oxygen activities). This observation was the internal oxidation of steel with the formation of aluminum-oxide particles within the matrix. The depth of detected internal oxidation throughout various positions of the sample was not uniform. This depth varied from approximately a dozen micrometers to a few hundred micrometers.

The non-uniform depth of oxidation could be explained by the direct contact of quartz glass with alloys at 1000 °C for 7 days. Therefore, it would be relevant to address the solubility of SiO_2 in the examined alloy. Considering that the solubility of SiO_2 in Fe is generally low, and experimental solubility values of SiO_2 are often reported in molten iron, as demonstrated in the works of Hirose et al. [114] or Shibaev et al. [115], the solubility value of SiO_2 at the temperature of experiment in Fe-16Cr-0.2Al (bcc) was here only theoretically calculated and reported. The solubility limit of SiO_2 at 1000 ˚C was calculated to be about 0.7 wt.% by TCFE7 [88]. The solubility of SiO_2 in the examined alloy could affect the homogeneity of the matrix, and hence the nucleation sites of oxide particles in different spots of the sample were altered. Moreover, the nucleation of the further oxide dispersoids in the matrix could occur during the sample quenching and therefore an extended region of IO was observed.

Based on Wagner's theory presented in detail in chapter 2 (section 2.1.1), it was shown that two limiting conditions led to two modes of internal oxidation as follows:

1. Oxygen permeability (product of the diffusion coefficient and concentration) was much higher than the less noble alloying element.
2. Permeability of less noble alloying element was much higher than oxygen permeability.

To assess the mode of internal oxidation occurred in this work with the presence of (V_2O/VO) buffer system at 1000 ˚C, the limiting conditions (18) and (23) (after Wagner's theory described in chapter 2) were examined at the temperature of the experiment. To do this, at the first step by using MOBFE2 [93], the diffusion coefficients of aluminum and oxygen in Fe-16Cr at different temperatures were obtained. The mobility parameters for the diffusion coefficients of oxygen in ferrite (bcc) using the literature [116-118] were re-optimized and new parameters were then applied by Dr. Peter Franke [119]. Aluminum was assumed to be fully consumed in the internal oxidation zone and converted to oxides. Based on this assumption, the solubility value of oxygen in the matrix was calculated. In other words, the aluminum content in the matrix was set to zero. The solubility value of oxygen (N_O^S) in Fe-16Cr at different oxygen activities was calculated with Thermo-Calc software using the database developed by Kjellqvist et al. [89] and shown in Fig. 31.

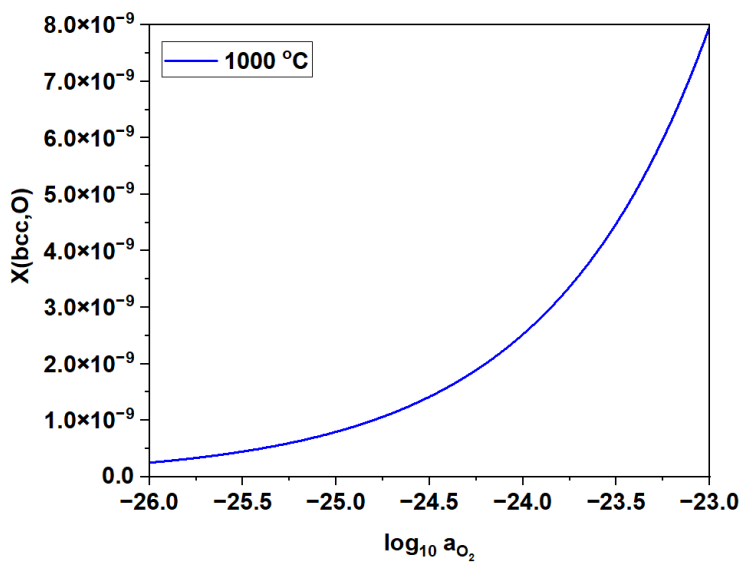

Fig. 31 The solubility of oxygen in bcc-matrix (Fe-16Cr) at 1000 ˚C. The data was calculated using the database developed by Kjellqvist et al. [89].

The obtained solubility value in Fe-16Cr at the oxygen activity supplied by V_2O/VO buffer ($\log_{10} a_{O_2} \approx -24.5$) at 1000 °C was calculated to be 1.4×10^{-9} . The corresponding diffusion coefficients of aluminum and oxygen and their molar fractions in Fe-16Cr at 1000 °C were as follows:

$$D_{Al} = 5.3 \times 10^{-14}\ {m^2}/{s} \qquad (50)$$

$$D_O = 1.3 \times 10^{-10}\ {m^2}/{s} \qquad (51)$$

$$N_O^s = 1.4 \times 10^{-9} \qquad (52)$$

$$N_{Al}^0 = 4.0 \times 10^{-3} \qquad (53)$$

According to the above values, condition (23) in chapter 2 was fulfilled as:

$$\frac{N_O^s}{N_B^0} \ll \frac{D_B}{D_O} \ll 1 \quad \rightarrow \quad 0.00000035 \ll 0.000408 \ll 1 \qquad (54)$$

Under this condition, the permeability of oxygen was slower than aluminum and known as the slow mode of Wagner's internal oxidation theory. Based on this, the parameter γ defined in equation (21) was simplified as:

$$\gamma = \left(\frac{\pi \times 1.3 \times 10^{-10}}{5.3 \times 10^{-14}}\right)^{0.5} \times \left(\frac{1.4 \times 10^{-9}}{3 \times 4.0 \times 10^{-3}}\right) = 1.02 \times 10^{-5} \qquad (55)$$

The IOZ depth according to equation (24) in chapter 2 was written as:

$$L_{in} = (2.33 \times 10^{-10})\ t^{0.5} \quad {m}/{s^{0.5}} \qquad (56)$$

The IOZ depth versus time of oxidation was then plotted after equation (56) and shown in Fig. 32. The calculated IOZ depth at 1000 ˚C for 7 days (168 hours) showed theoretically a depth of about 0.18 µm but the obtained experimentally IOZ depth varied from approximately a dozen of micrometers to a few hundred micrometers.

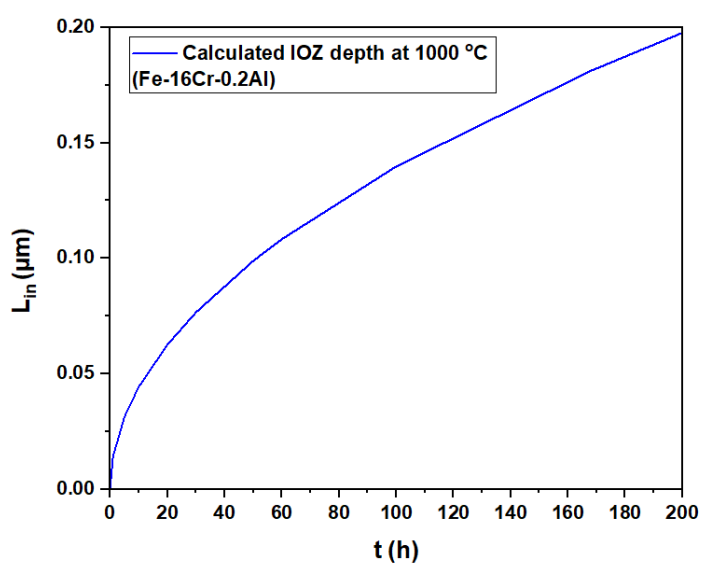

Fig. 32 Calculated IOZ depth at 1000 ˚C for Fe-16Cr-0.2Al alloy in presence of V_2O/VO oxygen buffer.

To explain this deviation, the addition of a ternary element (i.e. Cr) into the system made complexities to the classical Wagner's theory and therefore achieved IOZ depth might deviate from the calculated values. In section 4.3.3, an analytical comparison will be presented to illustrate the change in the solubility value of oxygen as well as the diffusion coefficient of aluminum and oxygen, upon the introduction of chromium into the system. This analysis aims to clarify the observed issue.

It might be intriguing here to explore, as supplementary information, the work of Meijering [120], where the permeability values of oxygen after the oxidation of three iron-based alloys (Fe-0.97Al, Fe-0.99Al-30Ni and Fe-0.50Al-5Sn in wt.%) were calculated. Fe-0.97Al alloy was used for comparison purposes, as it was the alloy most similar to the examined alloy in this work. The quantitative results of the permeability values of oxygen reported by Meijering [120] were digitized, and the value at 1000 ˚C was recorded as approximately $6.2 \times 10^{-15}\ {m^2}/{s}$. The calculated permeability value ($D_O N_O^s$) in the current study at 1000 ˚C was $1.8 \times 10^{-19}\ {m^2}/{s}$.

To explain this deviation, it should be noted that in the work of Meijering [120], it was hypothetically assumed that permeability of oxygen was much higher than aluminum. Therefore, the fast mode of Wagner's theory was applied, and based on this assumption, the permeability values were then calculated. In the current study, as demonstrated in condition (54), the slow mode of Wagner's theory was found to be valid, and the actual values of oxygen permeabilities would be much lower than suggested in the work of Meijering [120].

The oxidation results for Fe-9Cr-0.2Al at 1000 ˚C for 7 days in the presence of V_2O/VO showed similar results in which the oxide particles were detected mainly in outer areas. These results were the first successful internal oxidation in this work and held a meaningful promise for further experiments.

4.3 Oxidation in high temperature furnace by embedding Fe-Cr-Al alloy into oxygen buffer system

The second set of experiments with V_2O/VO buffer at a higher temperature for 20 hours was performed to promote a more extensive internal oxidation zone. As mentioned

previously, in this set of experiments, the alloy was completely embedded in the buffer mixture.

4.3.1 V_2O/VO oxygen buffer results for Fe-16Cr-0.2Al alloy

The results at a higher temperature experiment (1300 °C) for Fe-16Cr-0.2Al by direct contact of the alloy and powder mixture (V_2O/VO) was shown in this section. The specimen was in the form of a small cube with a few millimeters in size. The exposed surfaces of the samples did not show external oxidation and one outer surface of the specimen is shown in Fig. 33 a. The sample was then ground down for 2 mm from one side and afterwards imaged to assess how the depth of internal oxidation changes (Fig. 33 b). A substantial internally oxidized zone in the interior of the alloy was not seen and a few oxide particles were present.

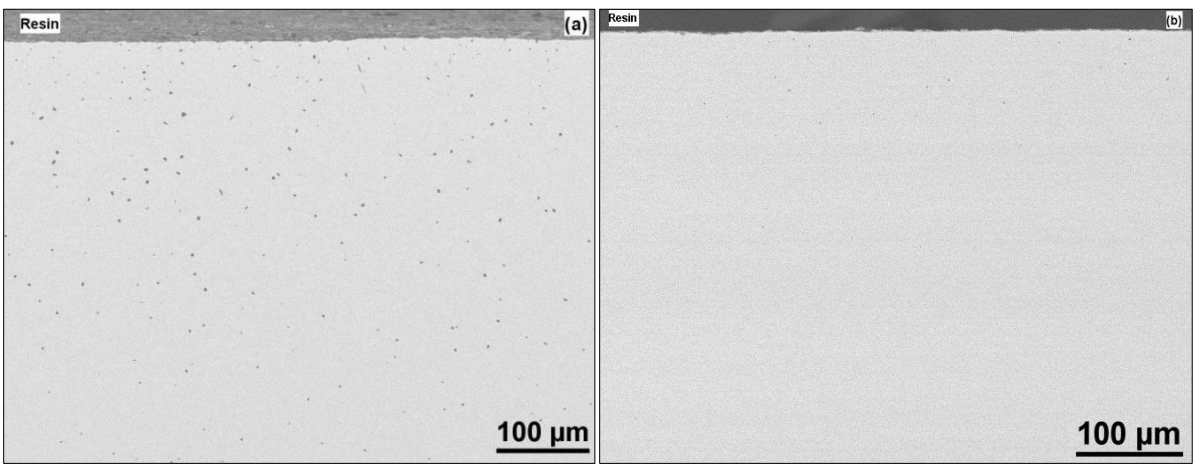

Fig. 33 The oxidation result of Fe-16Cr-0.2Al (A01) after oxidation at 1300 ˚C for 20 hours in V_2O/VO mixture. The specimen was in the form of a small cube with a few millimeters size. The images were backscattered-micrographs using SEM method: (a) the micrograph of the external surface of the sample, (b) cross-section approximately through the middle of sample, showed a few oxide particles left on the surface (the cubic sample was ground 2 mm from one side).

To apply the Wagner's theory, the corresponding diffusion coefficients of aluminum and oxygen and their molar fractions in Fe-16C at 1300 °C for conditions (18) and (23) in chapter 2 were used as:

$$D_{Al} = 3.8 \times 10^{-12} \quad {m^2}/{s} \qquad (57)$$

$$D_O = 1.4 \times 10^{-9} \; {m^2}/{s} \qquad (58)$$

$$N_O^s = \; 4.3 \; \times 10^{-8} \qquad (59)$$

$$N_{Al}^0 = 4.0 \times 10^{-3} \qquad (60)$$

The solubility value of oxygen (N_O^S) in Fe-16Cr at the oxygen activity of the experiment was calculated with Thermo-Calc software using the database developed by Kjellqvist et al. [89]. According to the above values, condition (23) in chapter 2 was fulfilled:

$$\frac{N_O^S}{N_B^0} \ll \frac{D_B}{D_O} \ll 1 \quad \rightarrow \quad 0.00001075 \ll 0.00271 \ll 1 \qquad (61)$$

Under this condition, the slow mode of Wagner's internal oxidation theory became valid. Based on this, the parameter γ defined in equation (21) was simplified as follows:

$$\gamma = \left(\frac{\pi \times 1.4 \times 10^{-9}}{3.8 \times 10^{-12}}\right)^{0.5} \times \left(\frac{4.3 \times 10^{-8}}{3 \times 4.0 \times 10^{-3}}\right) = 12.29 \times 10^{-5} \qquad (62)$$

The IOZ depth according to equation (24) was then written as:

$$L_{in} = (9.12 \times 10^{-9})\ t^{0.5}\ {}^{m}/_{s^{0.5}} \qquad (63)$$

The calculated IOZ depth at 1300 °C for a duration of 20 hours theoretically indicated a depth of approximately 2.4 µm. The actual depth of the internally oxidized zone under the given experimental conditions was indeed quite negligible as well, as shown in Fig. 33 b (a few oxide particles left on the surface). The IOZ depth was plotted against the oxidation time (up to 200 hours) using equation (63), and the result is presented in Fig. 34. It could be assumed after Fig. 34 that even after 200 hours of oxidation, the IOZ depth remained less than 8 µm, indicating a limited extent of internal oxidation.

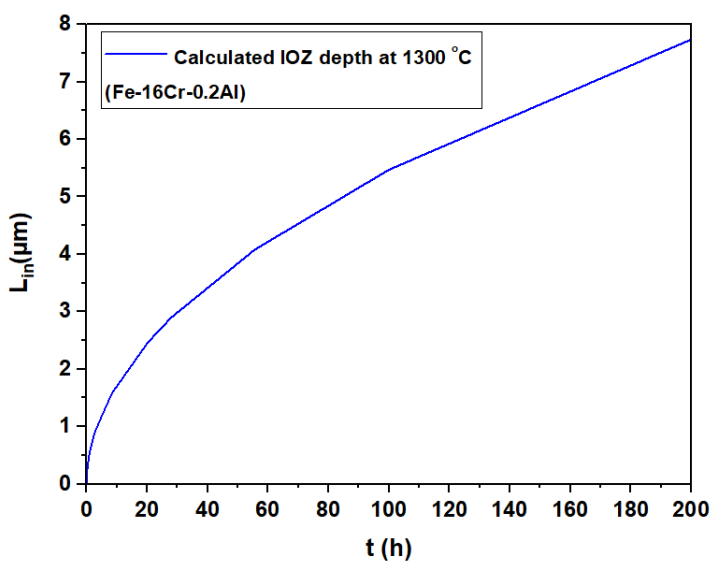

Fig. 34 Calculated IOZ depth at 1300 ˚C for Fe-16Cr-0.2Al alloy in presence of V_2O/VO oxygen buffer.

The thermodynamic calculations with V_2O/VO oxygen buffer at 1000 ˚C and 1300 ˚C were afterwards performed and shown in Fig. 35 a and b, respectively. The calculations were done at fixed oxygen activities and the alloy compositions were also indicated.

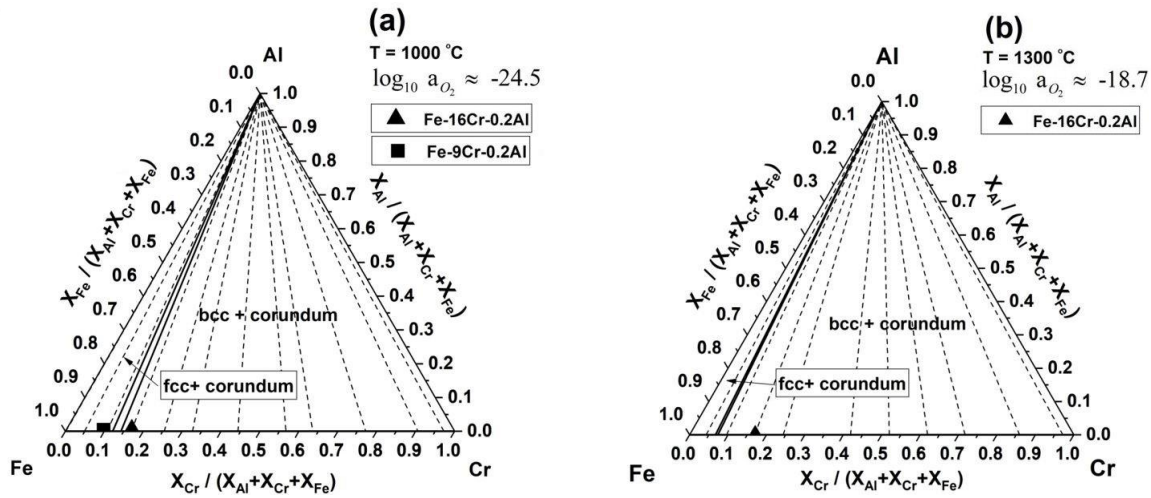

Fig. 35 Calculated phase diagram of the system Fe-Cr-Al-O with V_2O/VO oxygen buffer (a) at 1000 ˚C and oxygen activity of $10^{-24.5}$, (b) at 1300 ˚C and oxygen activity of $10^{-18.7}$. Alloy compositions were shown in both diagrams and the oxygen activity for each temperature was fixed. Some tie-lines were illustrated by dashed-lines in two phase regions.

Dashed-lines illustrated some tie-lines in two phase regions of (bcc+corundum) and (fcc+corundum) as well. The bcc, fcc and corundum were ferrite, austenite and Al_2O_3-based phase, respectively. For Fe-16Cr-0.2Al, bcc (ferritic steel) and corundum were in equilibrium for both temperatures (see again Fig. 35 a and b). For Fe-9Cr-0.2Al (Fig. 35 a), the equilibrium between fcc (austenitic) and corundum at 1000 °C existed. The calculated thermodynamic modelling for both alloys agreed well with the observed experimental results. In addition, two complementary arguments were presented for internal oxidation in this system as follows.

It was argued in section 3.3.2 that under Ar 6.0 atmosphere, the hypothesis of internal oxidation due to possible oxygen impurities could not be realistic. The results obtained in this section (4.3.1) supported the argument in section 3.3.2, since no external scales were detected in the second set of experiments with direct contact with the buffer system. Instead, only Al_2O_3-based discrete particles were observed.

One another interesting argument would be that in Fe-based alloys, the achievement of Al_2O_3-based separate oxides was not intensively researched; most of the published

works in this area finally turned to the oxidation of alloying elements like Mn or Cr with IOZ depth of about a few micrometers. It might be mentioned, for example, to the work of Prillieux et al. [121]. In this work, the formation of $FeCr_2O_4$ and Cr_2O_3 oxide particles in Fe-Ni-Cr alloys at 1150 °C under H_2/H_2O mixture (with the ratio of 1.36) were reported as shown in Fig. 36. The oxygen activity of the experiments at this temperature was 2.45×10^{-13}. The images were displayed here as they were in the publication.

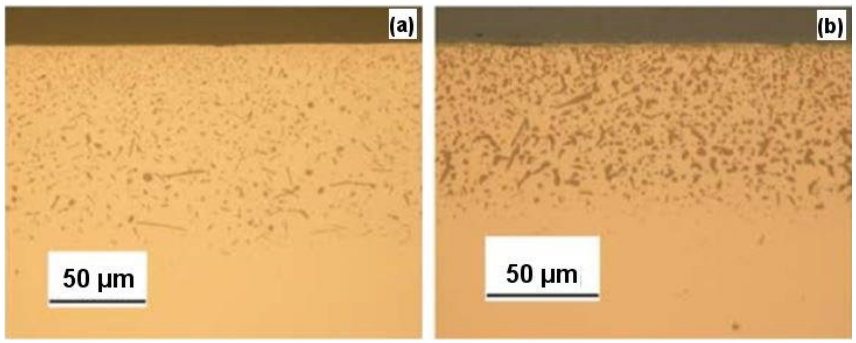

Fig. 36 The internal oxidation of Fe-Ni-Cr alloys after 8 hours at 1150 °C in H_2/H_2O mixture with the ratio of 1.36, (a) $\frac{N_{Fe}}{N_{Fe}+N_{Ni}} = 0.8$ and $N_{Cr} = 0.02$, (b) $\frac{N_{Fe}}{N_{Fe}+N_{Ni}} = 0.8$ and $N_{Cr} = 0.075$ [121].

The obtained oxides in the work of Prillieux et al. [121], as an example, were Fe-Cr mixed particles and also Cr-O based dispersoids. In the current work, as it was mentioned previously, unlike many other internal oxidation studies in the literature, the pursuance of the formation of specific types of oxides with considerable depth of oxidation was among the first priorities. To accomplish this objective, the following experiments were carried out.

4.3.2 Oxidation of Fe-16Cr-0.2Al alloy with Cr/Cr_2O_3 oxygen buffer

The oxygen buffer system of (Cr/Cr_2O_3) was re-applied in further experiments. This buffer provided higher oxygen activity ($10^{-16.0}$) relative to (V_2O/VO) buffer system ($10^{-18.7}$) as discussed in earlier section. It was reported that (Cr/Cr_2O_3) buffer system inside the evacuated quartz glass ampoule at 1000 ˚C for Fe-16Cr-0.5Al and Fe-9Cr-0.5Al alloys was used, but an unexpected result of the formation of AlN-phase was observed (described in section 4.2.1). This buffer (Cr/Cr_2O_3) was re-applied at 1300 ˚C with direct contact to alloys, since the calculated partial phase diagram at this temperature (see Fig. 37) suggested no chance of the formation of AlN.

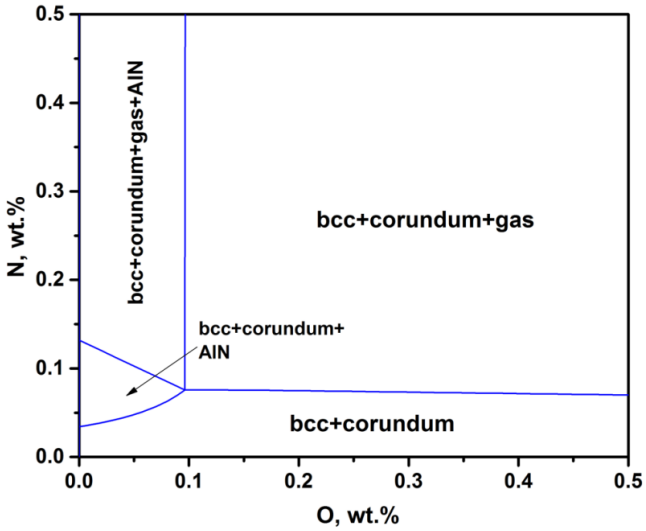

Fig. 37 Calculated partial isothermal section of Fe-Cr-Al-O-N system at 1300 ˚C. The Cr and Al contents of the system were fixed to 16.0 wt.% and 0.2 wt.%, respectively.

The Cr and Al contents for the calculation were fixed to 16.0 wt.% and 0.2 wt.%, respectively. The phase diagram consisted of four regions, and the stable phases in each region were noted. In this phase diagram (Fig. 37) corundum, gas, bcc and fcc were $(Al,Cr)_2O_3$, N_2-gas, ferrite and austenite, respectively. The region of interest (bcc+corundum) was expanded over the whole axis of the oxygen weight percentage. This emphasized that the formation of AlN-phase was unlikely by using (Cr/Cr_2O_3) buffer at this temperature. According to this prediction, the experiment by embedding the alloy into (Cr/Cr_2O_3) buffer was performed, and the result is given in Fig. 38.

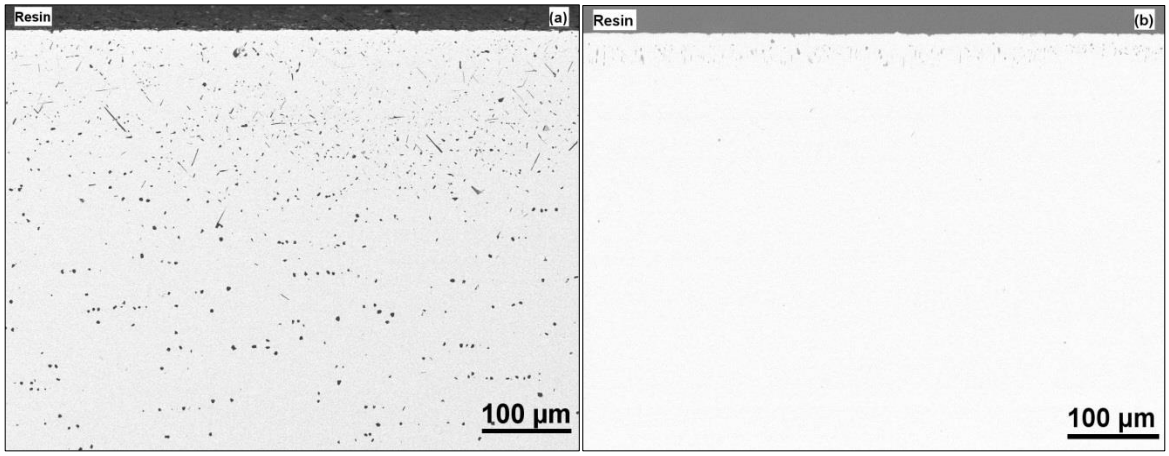

Fig. 38 The oxidation result of Fe-16Cr-0.2Al (A02) after oxidation at 1300 ˚C for 20 hours Cr/Cr_2O_3 mixture. The specimen was in the form of a small cube with a few millimeters size. The SEM images were backscattered-micrographs using SEM mthod: (a) the micrograph of the external surface of the sample, (b) cross-section approximately through the middle of sample, showed a few oxide particles left on the surface (after 2 mm grinding from one side).

The observed result was the internal oxidation of the exposed surfaces of the specimen, and discrete aluminum-oxide particles were formed on all external surfaces of the sample (Fig. 38 a). However, the formation of such particles within a substantial distance from the external surfaces towards the bulk of the sample was not detected. IOZ was measured to be about 30 µm after 2 mm grinding the cubic sample from one side (Fig. 38 b). To apply Wagner's theory, the corresponding diffusion coefficients of aluminum and oxygen and their molar fractions in Fe-16C at 1300 °C for conditions (18) and (23) in chapter 2 were calculated as follows. The solubility value of oxygen (N_O^S) in Fe-16Cr at the oxygen activity of the experiment was calculated with Thermo-Calc software using the database developed by Kjellqvist et al. [89].

$$D_{Al} = 3.8 \times 10^{-12}\ {m^2}/{s} \qquad (64)$$

$$D_O = 1.4 \times 10^{-9}\ {m^2}/{s} \qquad (65)$$

$$N_O^S = 9.7 \times 10^{-7} \qquad (66)$$

$$N_{Al}^0 = 4.0 \times 10^{-3} \qquad (67)$$

The condition (23) in Wagner's theory was then satisfied as follows:

$$\frac{N_O^S}{N_B^0} \ll \frac{D_B}{D_O} \ll 1 \quad \rightarrow \quad 0.0002425 \ \ll \ 0.002714 \ll 1 \qquad (68)$$

Under this condition, the permeability of oxygen was therefore smaller than of aluminum (the slow mode of Wagner's internal oxidation theory). Based on this, the parameter γ was defined in equation (21) and simplified as:

$$\gamma = \left(\frac{\pi \times 1.4 \times 10^{-9}}{3.8 \times 10^{-12}}\right)^{0.5} \times \left(\frac{9.7 \times 10^{-7}}{3 \times 4.0 \times 10^{-3}}\right) = 27.49 \times 10^{-4} \qquad (69)$$

The IOZ depth according to equation (24) was written as:

$$L_{in} = (2.06 \times 10^{-7})\ t^{0.5} \quad {m}/{s^{0.5}} \qquad (70)$$

The IOZ depth versus time of oxidation was then plotted after equation (70) and shown in Fig. 39. The theoretical IOZ depth of the oxidized alloy with (Cr/Cr_2O_3) buffer was estimated to be about 55 µm which was comparable to the observed IOZ in the experiment in Fig. 38 b (about 30 µm).

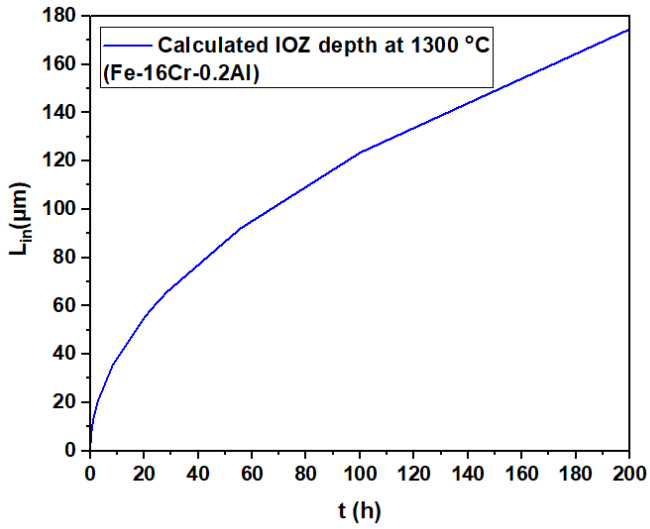

Fig. 39 Calculated IOZ depth at 1300 ˚C for Fe-16Cr-0.2Al alloy in presence of Cr/Cr_2O_3 oxygen buffer.

This buffer system (Cr/Cr_2O_3) also had a challenge regarding Cr diffusion into the specimen, since Cr as the pure metallic powder in the buffer powder mixture had a direct contact with the sample. For this purpose, the diffusion couple of Cr adjacent to the alloy was simulated and shown in Fig. 40.

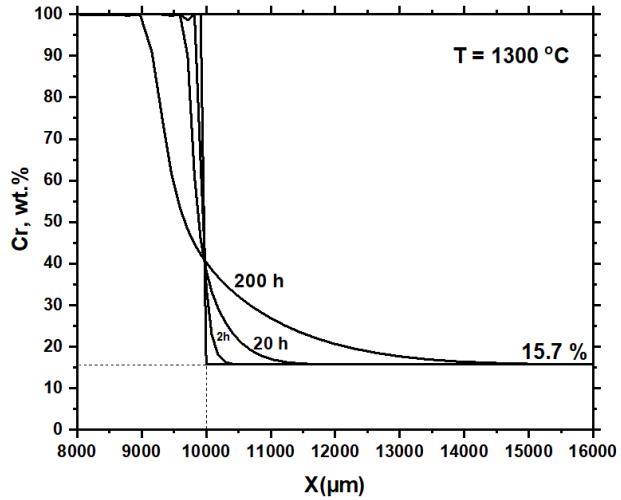

Fig. 40 The simulated diffusion profile of Cr into Fe-16Cr-0.2Al (A02) at 1300 ˚C after 2 h, 20 h and 200 h, respectively (15.7 wt.% in the diagram was the Cr concentration of as-cast alloy measured by ICP-OES. See again Table 3).

The Cr content of as-cast alloy (A02) was 15.7 wt.%. This value for the calculation was then used. The diffusion depth of Cr for example after 20 hours could be estimated to about more than 1000 µm (or 1 mm), and this highlighted that diffusion of the Cr into the alloy was a concern. In addition to the above simulation, an EDX line scan from the

surface of the alloy to the middle of the sample (after 2 mm grinding of the cubic sample) is shown in Fig. 41.

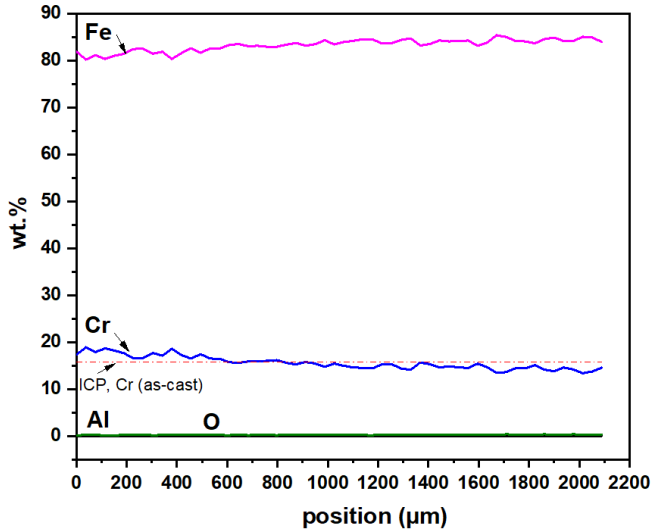

Fig. 41 An obtained EDX line scan from the surface of Fe-16Cr-0.2Al (A02) into the middle of the cubic sample (after 2 mm grinding from one side) after the experiment at 1300 ˚C for 20h oxidation with Cr/Cr_2O_3 buffer mixture.

In the above EDX line scan (Fig. 41), Cr contents of the alloy after the oxidation up to about 700 µm from the surface were above the original Cr content of the alloy. Cr contents at positions from the surface in Fig. 41 (position > 1000 µm) became lower than the original Cr content (measured by ICP method). To address this issue, the Al contents versus the position and a fitted polynomial (second order) are given in Fig. 42.

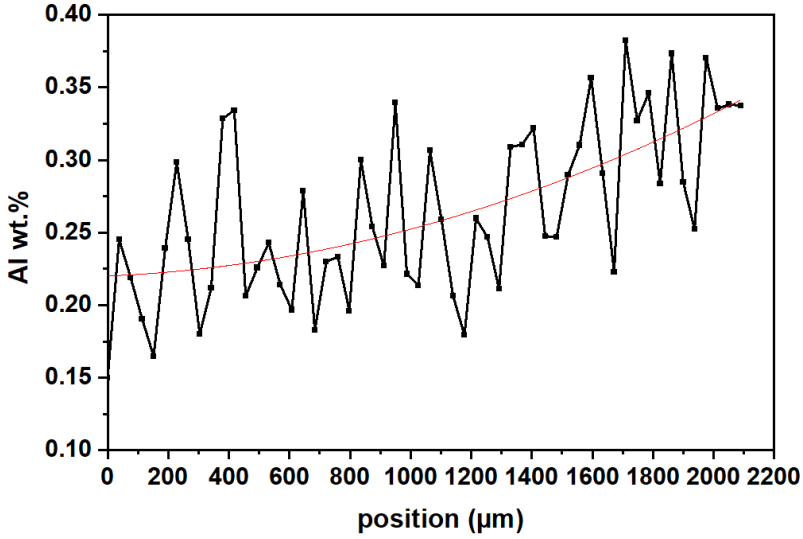

Fig. 42 An obtained Al EDX line scan from the surface of Fe-16Cr-0.2Al (A02) into the middle of the cubic sample (after 2 mm grinding from one side) after the experiment at 1300 ˚C for 20h oxidation with Cr/Cr_2O_3 buffer mixture.

The detection limit with the EDX method for bulk materials is reported to be 0.1 wt.% [122], and the observed EDX line of Al was reliable accordingly. As observed in Fig. 42, Al contents showed scattering, rising from the interior towards the exterior of sample. Correspondingly, Cr content in inner regions dropped sporadically (refer to the positions above 1000 µm in Fig. 41 and Fig. 42).

It is noteworthy that at a position around 1700 µm in Fig. 42, the largest scattering between two successive measured points occurred, approximately 0.16 wt.% Al (0.32 at.% Al). To elucidate if the observed largest scattering correlates with the distance from the surface, one additional available similar line scan, about 1450 µm in length, extending from the surface of the alloys into the interior of the sample, was analyzed. In this scan, the largest scattering between two successive points for Al was recorded to be about 0.22 wt.% (0.45 at.%). This largest scattering was observed at a position around 450 µm from the surface. Considering the absolute values and the position of the largest scattering from the surface of the alloy and reverting to the fact that IOZ depth in this experiment was constrained (about 30 µm in Fig. 38 b), the position of the occurrence of the largest scattering for Al would be more likely to be incidental.

To comment on a very thin IOZ and generation of a few oxide particles, it must be considered that 20 hours oxidation time with (Cr/Cr_2O_3) buffer system was insufficient to produce significant numbers of Al-O particles and a thick IOZ. The (Cr/Cr_2O_3) buffer system appeared to be a more reasonable candidate than (V_2O/VO) system, as it provided an oxygen activity of $10^{-16.0}$, higher than oxygen activity of $10^{-18.7}$ provided by (V_2O/VO) system. The simulation and experimentally observed results revealed that applying this buffer, due to Cr diffusion into the alloy and a very thin attained IOZ depth, was not practical.

4.3.3 Oxidation of Fe-16Cr-0.2Al alloy with VO/V_2O_3 oxygen buffer

Further experiments at higher oxygen activities using (VO/V_2O_3) buffer system were carried out. This buffer supplied greater oxygen activity than (V_2O/VO) and (Cr/Cr_2O_3) buffer systems, as the calculations suggested (presented in Table 5 and Ellingham diagram in chapter 2).

The results at 1300 ˚C and 1450 ˚C for 20 hours in the presence of (VO/V_2O_3) oxygen buffer for Fe-16Cr-0.2Al are illustrated in Fig. 43, respectively.

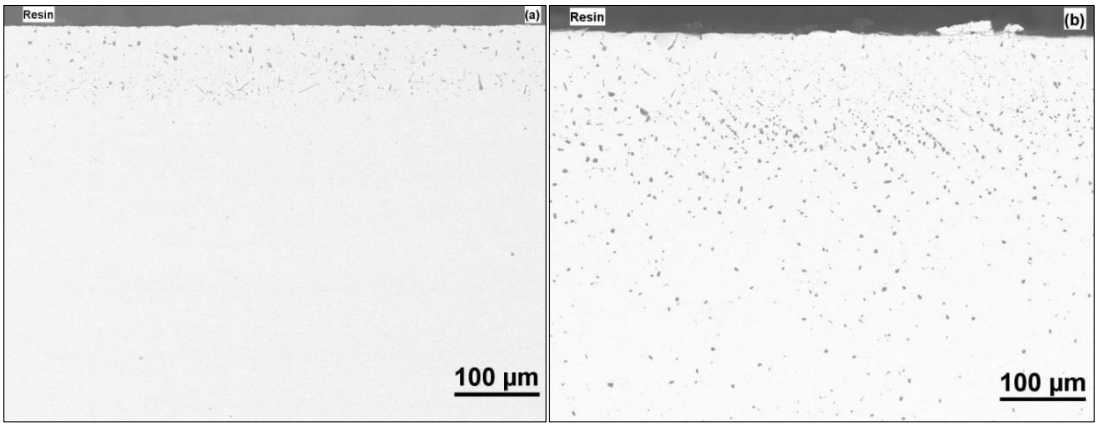

Fig. 43 The internally oxidized zone Fe-16Cr-0.2Al (A02) with VO/V_2O_3 buffer for 20 hours on a section approximately through the middle of the cubic sample (after 2 mm grinding from one side). The images were backscattered-micrographs using SEM method: (a) at 1300 ˚C, (b) at 1450 ˚C.

Both images corresponded to a section approximately through the middle of the cubic sample after 2 mm grinding from one side. The IOZ depth increased to approximately 100 µm at 1300 ˚C (Fig. 43 a). In contrast, the higher temperature experiment at 1450 ˚C led to a much higher depth of oxidation to about 2000 µm from one side (Fig. 43 b). The image in Fig. 43 b was processed with ImageJ software [123] to obtain the particles area, and each particle's area value was then converted to its diameter value. The size distribution of particles (cumulative) was then calculated and shown in Fig. 44.

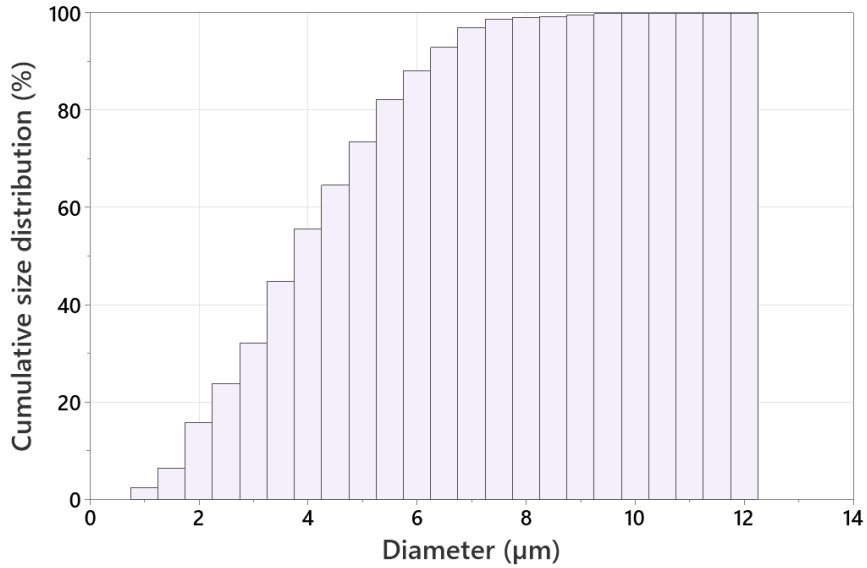

Fig. 44 The cumulative size distribution of particles in Fe-16Cr-0.2Al (wt.%) after oxidation with (VO/V_2O_3) buffer for 20 h at 1450 ˚C.

The mean value of the particles diameters was calculated to be 4.1 µm (standard deviation was 1.7). The size of particles varied between 0.9 µm and 12.2 µm and about 70% of the particles had a diameter of less than or equal to 5 µm.

Additionally, the image in Fig. 43 b was processed with ImageJ software [123], and the average distance between the oxides (mean spacing of the particles or L) was approximated. The image in Fig. 43 b was taken at different distances from the surface (Δx) and processed with three different thresholding methods available in ImageJ software [123], including the Default method, which is a variation of the IsoData algorithm [124], MaxEntropy [125] and the combination of Li [126] and triangle [127] methods. The average particle spacing, obtained after three measurements at each distance, along with their standard error, is shown in Fig. 45. The spacing increased with distance from the surface, and this was associated with the coarsening of particles in the interior of the alloy, hindering the nucleation of new particles. In other words, the particle spacing at the advancing reaction front increased with depth inside the internally oxidized zone.

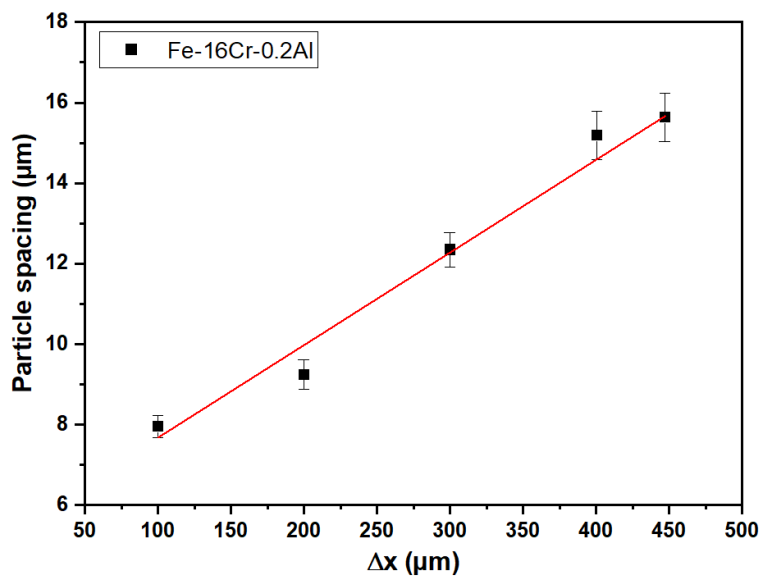

Fig. 45 Variation of particles spacing with their standard error within oxidation zone for Fe-16Cr-0.2Al after intern oxidation at 1450 ˚C.

One typical obtained EDX analysis for a particle and the selected scan area is shown in Fig. 46. In the obtained EDX regional scan from a particle (Fig. 46), the formation of Al-O based particles could be detected.

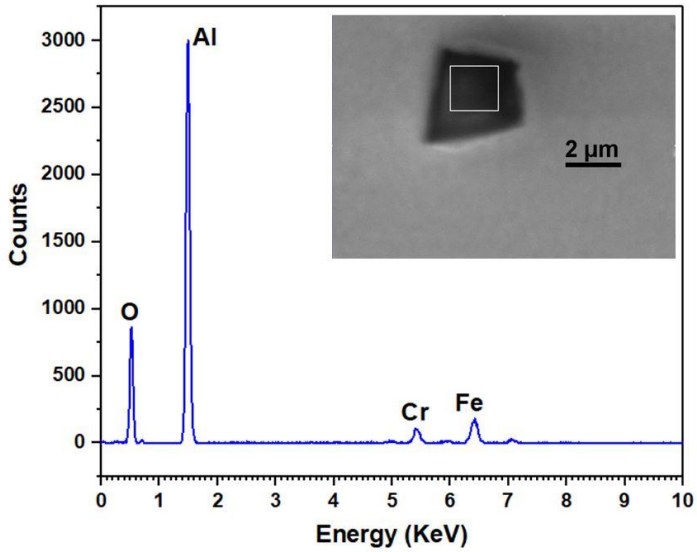

Fig. 46 A typical EDX region scan obtained from the produced particles in Fe-16Cr-0.2Al (A02) after oxidation experiment with VO/V_2O_3 buffer for 20 hours.

The presence of Fe and Cr peaks in Fig. 46 could be related to the small area of the selected region of interest and the effect of the surrounding matrix on the recorded spectra.

Based on Wagner's theory presented in chapter 2 (section 2.1.1), it was shown that two liming conditions led to two modes of internal oxidation. To discuss the mode of internal oxidation occurred by the presence of (VO/V_2O_3) buffer system at 1300 ˚C and 1450 ˚C, the limiting conditions (18) and (23) had to be examined at the temperatures of experiments. The molar fraction of oxygen solubility in Fe-16Cr at different oxygen activities at 1300 ˚C was calculated with Thermo-Calc software using the database file developed by Kjellqvist et al. [89] and shown in Fig. 47. The maximum oxygen solubility (N_O^S) at this experiment with oxygen activity of $10^{-15.0}$ was then reported to be 2.6×10^{-6}. The maximum solubility of oxygen in Fe-16Cr at this temperature (1300 ˚C) was about 2.7×10^{-6} under the oxygen activity of about $10^{-15.1}$ (see Fig. 47).

The reason for the existence of this maximum solubility in Fig. 47 lay in the fact that, at oxygen activities lower than about $10^{-15.1}$, only a single bcc was present. However, as oxygen activity increased, both bcc and corundum in Fe-16Cr alloy coexisted. Consequently, the solubility value of oxygen in bcc initially dropped at oxygen activities

higher than about $10^{-15.1}$, reaching a minimum around the oxygen activity of $10^{-14.8}$, after which it gradually increased (see Fig. 47).

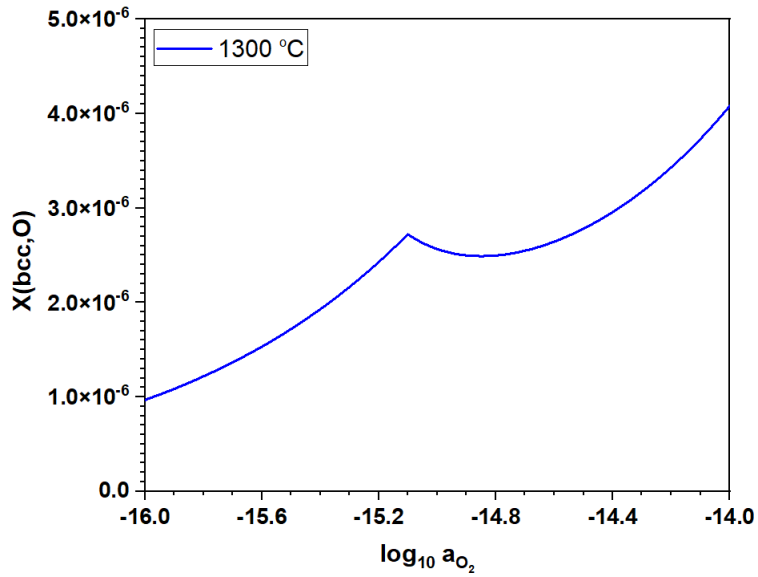

Fig. 47 The solubility of oxygen in bcc-matrix (Fe-16Cr) at 1300 ˚C. The data was calculated with the database developed by Kjellqvist et al. [89].

The corresponding diffusion coefficients of aluminum and oxygen and their molar fractions in Fe-16Cr (by considering no aluminum) for conditions (18) and (23) at 1300 ˚C were as follows:

$$D_{Al} = 3.8 \times 10^{-12}\ {m^2}/{s} \quad (71)$$

$$D_O = 1.4 \times 10^{-9}\ {m^2}/{s} \quad (72)$$

$$N_O^s = 2.6 \times 10^{-6} \quad (73)$$

$$N_{Al}^0 = 4.0 \times 10^{-3} \quad (74)$$

According to the above values, condition (23) in chapter 2 was fulfilled as:

$$\frac{N_O^s}{N_B^0} \ll \frac{D_B}{D_O} \ll 1 \quad \rightarrow \quad 0.00065 \ \ll \ 0.002714 \ll 1 \quad (75)$$

Under this condition, the permeability of oxygen was slower than aluminum (the slow mode of Wagner's internal oxidation theory). Based on this, the parameter γ according to equation (21) was as:

$$\gamma = \left(\frac{\pi \times 1.4 \times 10^{-9}}{3.8 \times 10^{-12}}\right)^{0.5} \times \left(\frac{2.6 \times 10^{-6}}{3 \times 4.0 \times 10^{-3}}\right) = 0.007369 \quad (76)$$

The IOZ depth according to equation (24) was then written:

$$L_{in} = (5.51 \times 10^{-7})\ \mathrm{t}^{0.5} \quad {}^{\mathrm{m}}/_{\mathrm{s}^{0.5}} \qquad (77)$$

The same strategy was applied for the experiment at 1450 °C. The solubility value of oxygen (N_O^s) in Fe-16Cr at the oxygen activity of the experiment ($10^{-12.8}$) was calculated and shown in Fig. 48. The maximum solubility of oxygen at this experiment was then reported to be 9.9×10^{-6} .

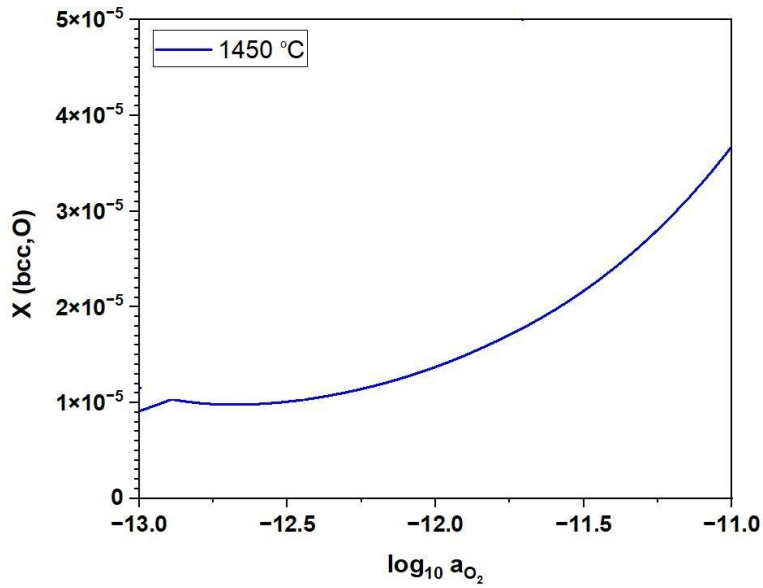

Fig. 48 The calculated solubility of oxygen in Fe-16Cr at 1450 °C.

In the oxygen activity range of 10^{-13} to about $10^{-12.9}$, only bcc is present. As the oxygen activity exceeds $10^{-12.9}$, a coexistence of the bcc and corundum occurs, leading to an initial decrease in solubility values up to an oxygen activity of about $10^{-12.7}$, followed by a gradual increase (see Fig. 48).

The corresponding diffusion coefficients of aluminum and oxygen and their molar fractions in Fe-16C for conditions (18) and (23) at 1450 ˚C were as follows:

$$D_{Al} = 1.8 \times 10^{-11}\ {}^{m^2}/_{s} \qquad (78)$$

$$D_O = 3.5 \times 10^{-9}\ {}^{m^2}/_{s} \qquad (79)$$

$$N_O^s = 9.9 \times 10^{-6} \qquad (80)$$

$$N_{Al}^0 = 4.0 \times 10^{-3} \qquad (81)$$

According to the above values, condition (23) in chapter 2 was fulfilled as follows:

$$\frac{N_O^s}{N_B^0} \ll \frac{D_B}{D_O} \ll 1 \quad \rightarrow \quad 0.0025 \ll 0.0051 \ll 1 \qquad (82)$$

Based on this, the parameter γ in equation (21) was defined as:

$$\gamma = \left(\frac{\pi \times 3.5 \times 10^{-9}}{1.8 \times 10^{-11}}\right)^{0.5} \times \left(\frac{9.9 \times 10^{-6}}{3 \times 4.0 \times 10^{-3}}\right) = 0.02 \quad (83)$$

The IOZ depth according to equation (24) was as:

$$L_{in} = (2.41 \times 10^{-6})\, t^{0.5} \quad {}^{m}/_{s^{0.5}} \qquad (84)$$

The IOZ depth versus time of oxidation was then plotted after equations (77) and (84) and shown in Fig. 49.

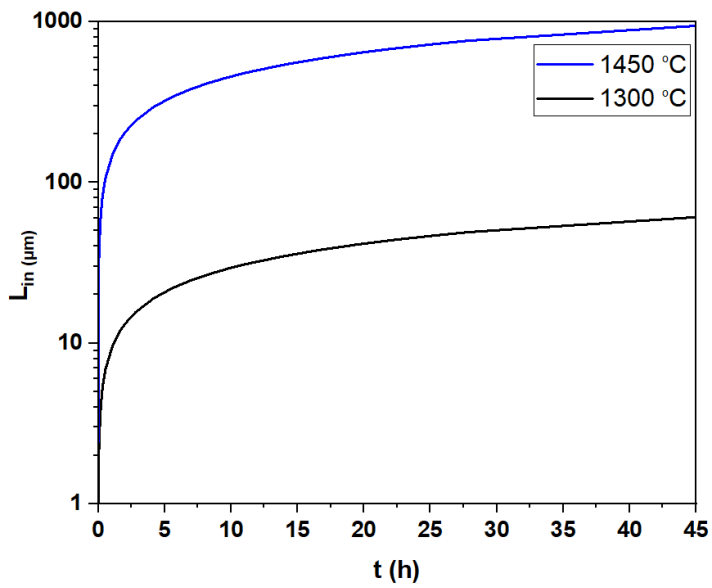

Fig. 49 The calculated IOZ depth for Fe-16Cr-0.2Al alloy oxidized with VO/V_2O_3 buffer system at 1300 °C and 1450 °C based on Wagner's theory of internal oxidation.

In Fig. 49 after 20 hours, the estimated IOZ for the experiment at 1300 ˚C and 1450 ˚C would be about 42 µm and 647 µm, respectively. On the other hand, the achieved IOZ depth in the experiment was about 100 µm and 2000 µm, respectively (see again Fig. 43). This difference in calculated IOZ based on Wagner's theory and observed result after experiment could be backed to the point that Wagner's theory considered only binary system, but in the current work the alloying element of Cr was additionally present which caused the deviation of IOZ from the theoretical value. As noted in section 4.2.3, an analytical comparison of the change in the solubility value of oxygen,

as well as the diffusion coefficient of aluminum and oxygen, upon the introduction of Cr into the system is presented here.

The first deviating factor was the solubility value of oxygen (N_O^s) in Fe-16Cr relative to Fe. The solubility value in Fe at the oxygen activity of the experiment ($10^{-12.8}$) at 1450 ˚C was calculated using the dataset file developed by Kjellqvist et al. [89], and it was found to be approximately 4.5×10^{-6}. The solubility value in Fe-16Cr at the same temperature (1450 ˚C) was about 9.9×10^{-6}, which was 2.2 times higher than in Fe. The reported data in the work of Heumann et al. [128] was digitized to approximate the diffusion coefficient of oxygen in Fe at 1450 ˚C, and it was found to be $3.9 \times 10^{-9}\ {m^2}/{s}$. The used data to extract the diffusion coefficient in Fe is provided in Appendix 8. The calculated the diffusion coefficient of oxygen in Fe-16Cr at 1450 ˚C in this study was reported to be $3.5 \times 10^{-9}\ {m^2}/{s}$.

The data presented by H. Oikawa [129] (shown in Appendix 9) was digitized, and the diffusion coefficient of Al in Fe at 1450 ˚C was found to be about $1.1 \times 10^{-11}\ {m^2}/{s}$. The calculated diffusion coefficient in the Fe-16Cr alloy was $1.8 \times 10^{-11}\ {m^2}/{s}$.

Taking into account theses three deviations (solubility value of oxygen, diffusion coefficients of O and Al) and referring to equation (24) in chapter 2, which indicated that the IOZ depth in the slow mode of Wagner's theory had a linear correspondence to the solubility and diffusion coefficient of oxygen, and an inverse relationship to the square root of the diffusion coefficient of aluminum. It could be expressed that, at constant time (20 h) and fixed solubility of Al (4.0×10^{-3}), and by substituting the above values for solubility values of oxygen and diffusion coefficients of O and Al, internally oxidized depth in Fe-16Cr alloy would be higher than in Fe as follows:

$$\mathrm{L_{in}^2} \cong \frac{(\mathrm{D_O N_O^s})^2\ \pi}{(\nu \mathrm{N_B^0})^2\ \mathrm{D_B}}\ \mathrm{t} \rightarrow \frac{L_{in\ (Fe-16Cr)}}{L_{in\ (Fe)}} = \frac{(3.5 \times 10^{-9}\ \times 9.9 \times 10^{-6})/(1.8 \times 10^{-11}\ )^{0.5}}{(3.9 \times 10^{-9}\ \times 4.5 \times 10^{-6})/(1.1 \times 10^{-11}\ )^{0.5}} > 1 \quad (85)$$

Based on (85), it could be explained at least how Cr caused the deviation in the system, thus explaining the observed higher IOZ depth than predicted by Wagner's theory.

Subsequent to this quantitative comparison, the experiments were further conducted. An internally oxidized sample was then etched and examined using light optical microscopy. The observation revealed that the particles were predominantly located within the grains (Fig. 50).

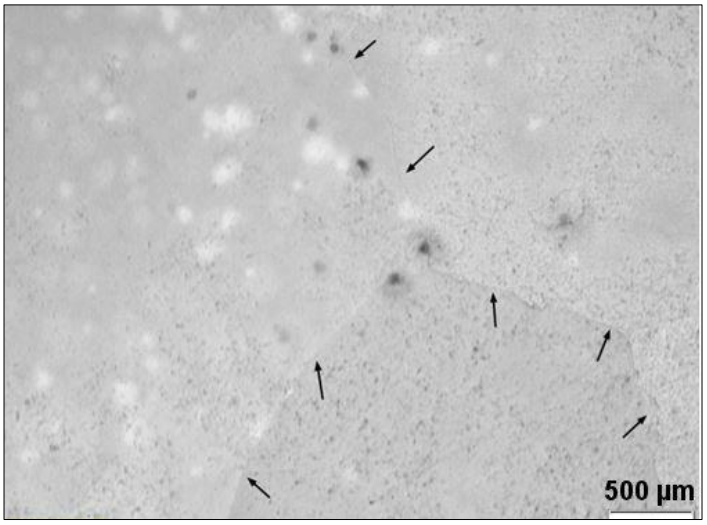

Fig. 50 The formation of oxide particles within the grains (light optical microscopy). The grain boundaries are highlighted with black arrows.

Since the internal oxidation was done at an elevated temperature of 1450 °C, the nucleation and growth of oxide particles had to be considered. Nuclei appeared preferably at the points of high-lattice-strain energy such as grain boundaries [42] as earlier mentioned. The diffusion along the grain boundaries would not be the main mechanism of oxygen diffusion and diffusion through grains was the primary mechanism. Grain boundary diffusion becomes generally important below about 0.75 to 0.8 T_m, where T_m is the melting temperature in Kelvin [108] (T_m was about 1790 K here).

Following the experiments, thermodynamic modelling was carried out to analyze and provide insights into the phase equilibria under the experimental conditions. The calculations at both temperatures and their oxygen activities showed that the alloy (Fe-16Cr-0.2Al) was in the two-phase area of bcc and corundum for both temperatures (see Fig. 51). Bcc and fcc were ferrite and austenite, respectively. The corundum, $(Al,Cr)_2O_3$, consisted of 85% mol.% or 92% mol.% Cr_2O_3 at 1300 or 1450 °C, respectively.

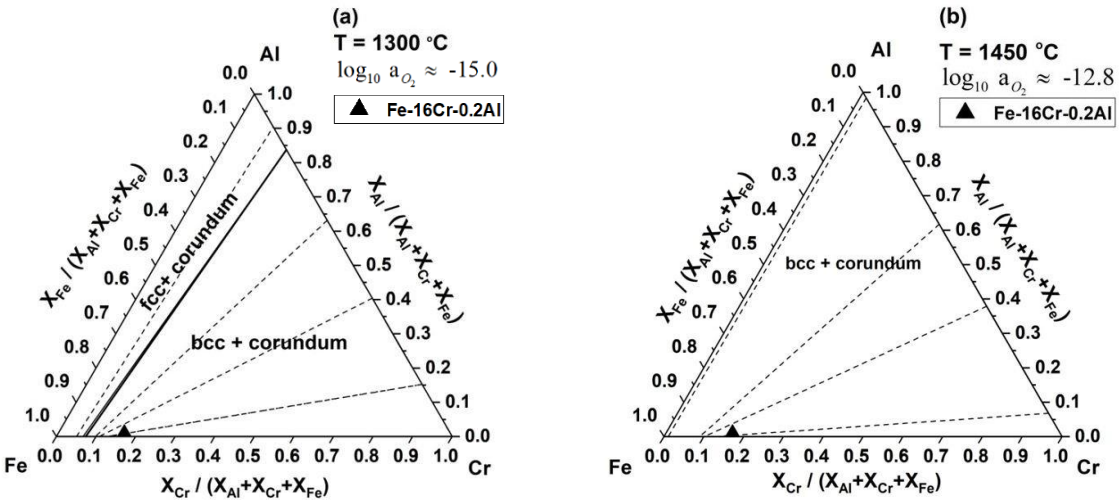

Fig. 51 Calculated phase diagram of the system Fe-Cr-Al-O with a VO/V_2O_3 oxygen buffer at fixed oxygen activities (some tie-lines were illustrated by dashed-lines): (a) at 1300 ˚C, (b) at 1450 ˚C.

The calculated results contradicted the EDX analyses (see again Fig. 46) which declared that the obtained particles were Al-O based oxides rather than Cr-O based oxides. To explain this contradiction, the diffusion simulations with DICTRA software using mainly TCFE7 [88] and MOBFE2 [93] databases were assessed by Dr. Peter Franke [119]. Since these two standard databases did not allow the diffusion in corundum (oxide phase), a database including a new corundum phase was developed internally at KIT and loaded in DICTRA program by Dr. Peter Franke [119]. Here, the corundum was described as a quasi-binary solid solution between Al_2O_3 and Cr_2O_3 and the thermodynamic description for this phase was taken from Saltykov et al. [130].

To simplify the phase model in the work of Dr. Peter Franke [119], the interstitial sublattice was omitted and diffusion in this phase was described with the "dilute" model of DICTRA. Data for the interdiffusion coefficient as a function of temperature and composition was obtained from the work of Atarashiya et al. [131]. After all the above modifications, the growth of an oxide particle within a ferritic alloy at 1450 °C with DICTRA software was modelled by Dr. Peter Franke [119]. Diffusion simulations were simplified to simple spherical geometries because only one independent space coordinate was available.

To model this growth, a spherical cell with a radius of 5 µm was chosen and then filled with a homogeneous alloy of bcc-iron containing 16 wt.% Cr and 0.2 wt.% Al and no

oxygen. The oxygen activity was fixed to the value of the VO/V_2O_3 equilibrium at 1450 °C ($10^{-12.8}$) at the surface of the spherical cell as boundary condition.

The atomic percentage of Cr was plotted in Fig. 52 as a function of position in the spherical cell after various diffusion times, indicated by their logarithms at the respective curves. In Fig. 52 at a diffusion time of 10^3 s, the oxide particle reached a radius of 0.8 µm and almost zero Cr content, and therefore it practically consisted of pure Al_2O_3. The chromium concentration was represented almost by a step-function, the vertical part coinciding with the phase boundary between the oxide and the bcc-alloy. At longer times chromium diffused into the oxide particle and enriched in its outer shell as shown by the curves 4 and 5. Finally, the Cr concentrations at about 10^6 s in the inner and outer shell were the same and the equilibrium was reached.

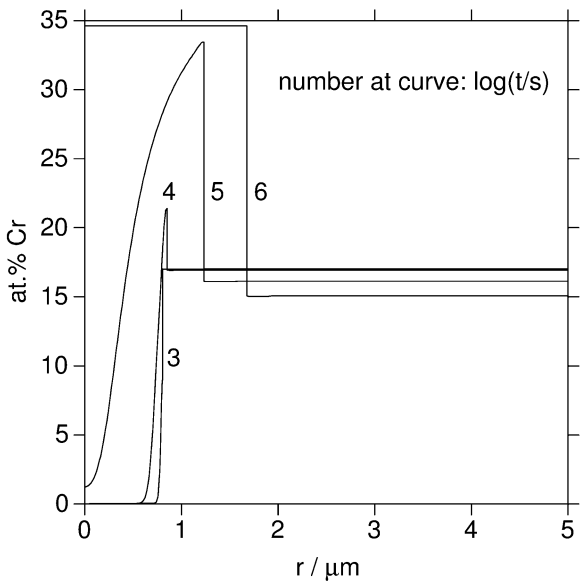

Fig. 52 Cr atomic percentage (at.%) as a function of position in the spherical cell [119].

The concentration profiles in the bcc-phase were almost horizontal at all diffusion times, while notable concentration gradients appeared only in the oxide phase. This effect was caused by the much different diffusion coefficients which were in the bcc-phase higher by several orders of magnitude than in the oxide.

In Fig. 53 the radius of the oxide particle was plotted as a function of time [119].

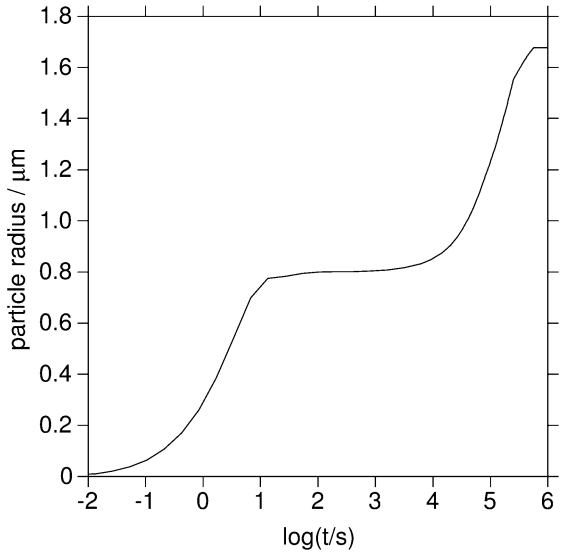

Fig. 53 The radius of the oxide particle as a function of time [119].

According to the results obtained by Dr. Peter Franke [119], the particle growth could be separated into two stages as:

1) The oxide growth was rapid until it reached a radius of 0.8 µm after 10 s and then the growth rate decelerated by several orders of magnitude. Initially, almost pure alumina was formed because it had a much lower Gibbs-energy of formation than chromia and therefore it formed already at much lower oxygen activities, as shown in Ellingham's diagram (presented in chapter 2). The rate-deciding step of the oxide growth in the first stage was the diffusion of aluminum in the bcc-phase toward the growing particle.

2) In the succeeding stage of slow growth, the kinetics was determined by the much slower diffusion of chromium into the oxide. During this stage, the oxygen activity at the phase boundary oxide/alloy gradually increased from low values near the Al/Al_2O_3 equilibrium to much higher values of the VO/V_2O_3 equilibrium.

The two-stage growth mechanism of the oxide clarified at least qualitatively why the EDX analysis of the oxide shown in Fig. 46 is Al-O based oxide with negligible Cr content. The investigated particle had probably reached the slow stage of growth but the incorporation of Cr_2O_3 was not yet enough to be detected.

4.3.3.1 The diffusion of vanadium into Fe-16Cr-0.2Al alloy

The powder mixture (VO/V_2O_3) was in direct contact with the alloy (Fe-16Cr-0.2Al), therefore the diffusion of vanadium into the alloy had to be considered. Since this buffer system comprised an oxide-oxide mixture, the metallic element (V) activity in this equilibrium was expected to be lower than in a metal-oxide mixture. This is explained in Fig. 54, which illustrates schematically molar Gibbs energy for M, MO and M_2O_3. Here, a general designation of M for metallic element was used (M denotes here vanadium or V). By applying the principle of the common tangent in equilibrium, it might be possible to determine the chemical potential values for the elements.

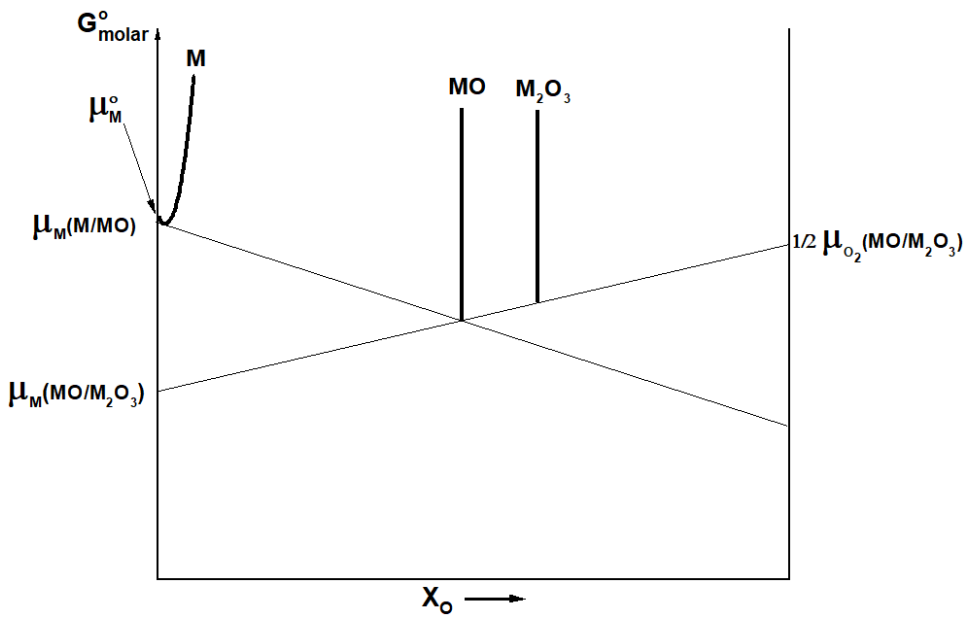

Fig. 54 The schematic comparison of the chemical potentials of metallic element in an oxide-oxide mixture (MO/ M_2O_3) with a metal-oxide mixture (M/MO).

The chemical potential of M in MO/M_2O_3 mixture was lower than the chemical potential in M/MO mixture (as shown in Fig. 54). The chemical potential of one component could be formulated to the activity of that component through the following equation:

$$\mu_i = \mu_i^o + RT \ln a_i \qquad (86)$$

According to the above equation, a lower chemical potential of a component in an equilibrium led to a lower activity of that component. Therefore, for element M in two equilibria of (M/MO) and (MO/ M_2O_3) could be written:

$$\mu_{M \text{ in } (MO/M_2O_3)} < \mu_{M \text{ in } (M/MO)} \rightarrow a_{M \text{ in } (MO/M_2O_3)} < a_{M \text{ in } (M/MO)} \qquad (87)$$

This revealed that the activity value of M in an oxide-oxide mixture had a lower value than in metal-oxide mixture. Therefore, the solubility of M in oxide-oxide mixture into alloy became less than the solubility of M in metal-oxide mixture into the same examined alloy. The choice of (MO/M_2O_3) compared to (M/MO) buffer system in direct contact to an alloy might cause fewer problems for the solubility of metallic component (M) into the examined steel. In this work, the diffusion profile of vanadium into the alloy at the fixed temperature of 1450 °C for 2 h, 20 h and 200 h into Fe-16Cr-0.2Al alloy was calculated (Fig. 55).

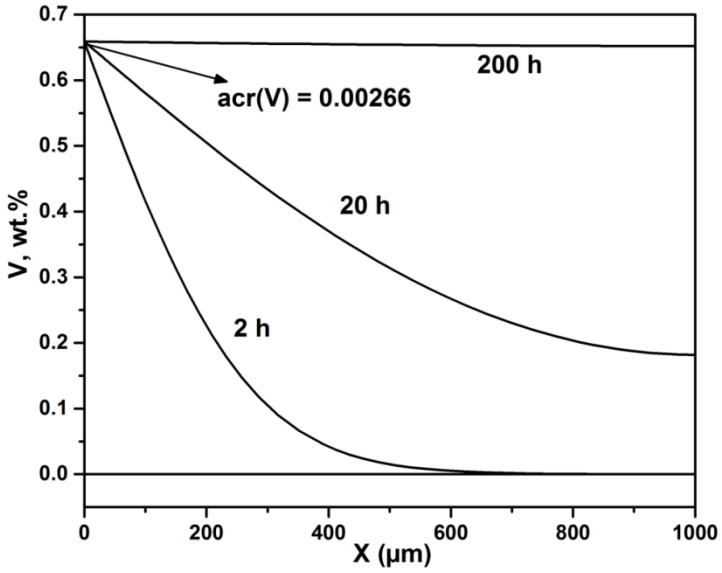

Fig. 55 The calculated diffusion profile of V from (VO/V_2O_3) powder mixture into Fe-16Cr-0.2Al at 1450 ˚C for 2 h, 20 h and 200 h.

To calculate the diffusion profile, the activity of vanadium relative to the standard phase of bcc at the temperature of experiment (here represented as acr-function) was obtained from the equilibrium between VO and V_2O_3 and acr(V) was determined to be 0.00266. The equivalent solubility of V into Fe-16Cr-0.2Al at 1450 ˚C was calculated not to be more than 0.66 wt.% in the matrix. This amount of vanadium in the matrix was negligible and would not change the properties of the steel considerably, and it affirmed that the application of this buffer (VO/V_2O_3) was highly reasonable and practical.

4.3.3.2 Electron backscatter diffraction analysis

For the specimen Fe-16Cr-0.2Al internally oxidized (with VO/V_2O_3 buffer at 1450 ˚C for 20 hours) an electron backscatter diffraction (EBSD) analysis was performed. EBSD

analysis of the alloy proved to be difficult. Although both the ferrite phase and the alumina corundum particles gave indexable EBSD patterns, the contrast difference was too high for automated mapping and analysis of the microstructure. EBSD spot analysis of single particles was used instead.

The significant difference in hardness of the surrounding matrix and the precipitates caused them to protrude from the sample surface. They could be easily imaged and identified by electron forward scatter images in the 70° tilted sample configuration. Fig. 56 shows one of these images. The recorded Kikuchi patterns (1-3) were displayed next to the corresponding measurement spots. All patterns could be indexed to the alumina corundum with high Confidence Index (CI) values and good fitting to the reference orientations.

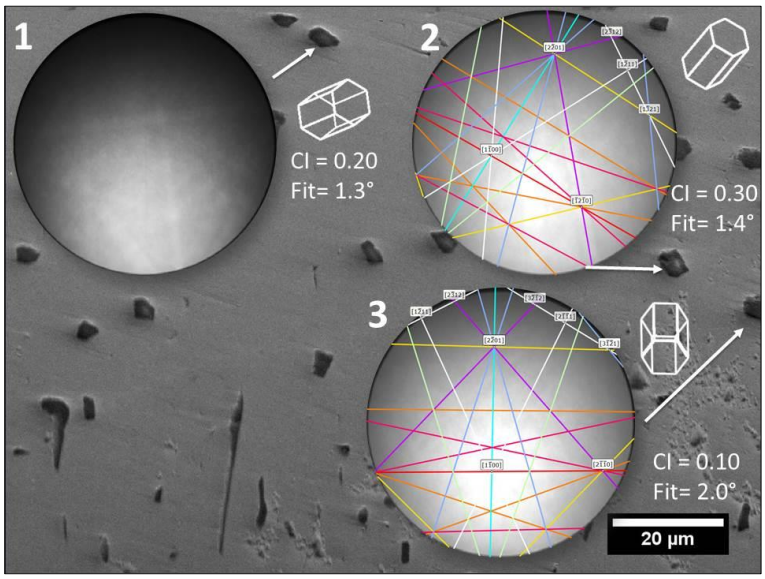

Fig. 56 FSD image with EBSD point analysis of different corundum precipitates. One pattern was shown prior to indexing to give an impression of the low pattern quality.

The CI was patented by EDAX and it represented the accuracy of the indexing and this parameter was determined during automated indexing for the diffraction pattern. CI was calculated after a voting scheme by the software and several possible orientations after fitting might be found to satisfy the obtained diffraction pattern. The voting system was then defined as:

$$\mathrm{CI} = \frac{\mathrm{S}_1 - \mathrm{S}_2}{\mathrm{S}_{\mathrm{total}}} \quad (88)$$

In the above equation, S_1 and S_2 were the number of votes for the first and second highest-ranking orientations, respectively and S_{total} was the total number of votes from the detected bands. A typically agreed correlation of the CI and the probability of the correct solution (in this case, alumina corundum) was reported by Field et al. [132] and shown in Fig. 57.

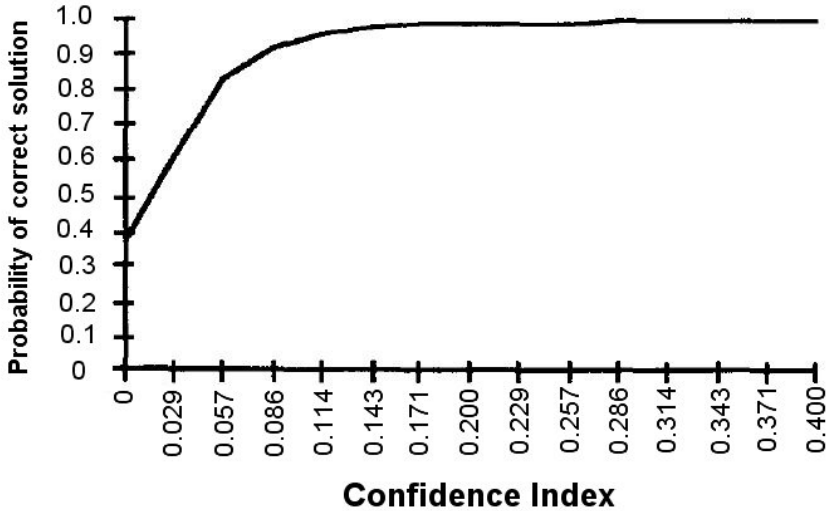

Fig. 57 The correlation of CI (confidence Index) and the probability of correct solution [132]. This image was graphically edited and represented.

CI varied in the range of 0 to 1 and a value of 0.1 equaled a 95 percent probability of a correct solution. Values of 0.2 and above would be virtually 100% correct. The fit parameter in EBSD indexing revealed also the average angular deviation between the detected position of bands and a recalculated position of the bands based on the orientations obtained from the voting procedure. Pattern no. 1 (see Fig. 56) was shown before the indexing to illustrate the weak contrast. In Fig. 56, CI values of 0.2 and 0.3 were obtained, and with these CI values, one can, with high assurance, attribute the generated oxides to alumina corundum.

4.4 Oxidation in high temperature furnace by embedding of Fe-Cr-Al-Y alloy into oxygen buffer system

The successful internal oxidation of Fe-Cr-Al alloys in the earlier sections was reported, and yttrium in trace amount was then added to the alloys to make the size of oxide particles finer; the formation of stable oxides such as Al-Y-O particles, might be achieved by this method as well.

4.4.1 Solubility of Y in iron-based alloys

The phase diagram of Fe-Y system and an enlarged section in the iron side at elevated temperatures (≥ 1300 °C) are shown in Fig. 58, which emphasizes the exceptionally low solubility of Y in Fe.

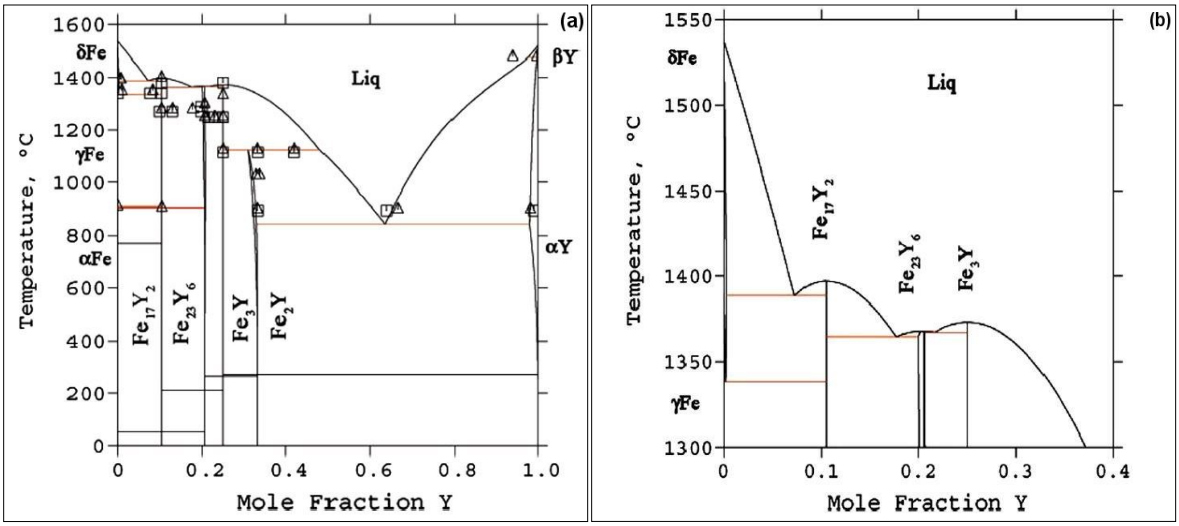

Fig. 58 The phase diagram of Fe-Y phase diagram, (a) the complete composition range, (b) the enlarged section of Fe side [133].

To highlight the extremely low solubility of Y into Fe-Cr alloys, one as-cast alloy (Fe-12.3Cr-0.4Y in wt.%) and after annealing at 1200 °C for 10 days is shown in Fig. 59. The chemical composition of the alloy was measured by ICP-OES method.

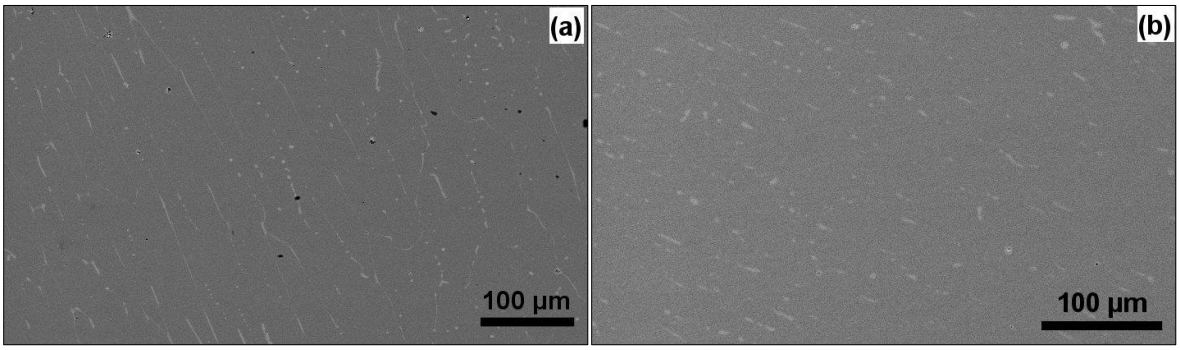

Fig. 59 Fe-12.3Cr-0.4Y (wt.%) alloy: (a) as-cast, (b) after annealing at 1200 °C for 10 days. The formation of $Fe_{17}Y_2$ or Fe-Y-Cr intermetallic phase for both conditions was seen (SEM method).

A segregated phase ($Fe_{17}Y_2$ or Fe-Y-Cr intermetallic) in the matrix of both as-cast and annealed alloy at 1200 °C for 10 days was seen (the phase with brighter contrast in Fig. 59). This revealed a solubility of less than 0.4 wt. % for Y into Fe-12.3Cr matrix. Since adding the alloying element (Cr and Al) into Fe did not significantly improve the

solubility of Y in the steel, the correct choice of initial Y amount for the current work was essential. Based on the assessment of Li et al. [134] for the Y solubility determination in Fe, and by extrapolating the measured results in their work to 1450 °C, the maximum limit of the solubility of Y in Fe at 1450 °C was estimated to be about 0.07 at.% or 0.11 wt.%. According to the extrapolation for the solubility of Y into Fe and performed preliminary annealing experiments for Fe-Cr-Y alloys, the added yttrium content to Fe-16Cr-0.2Al was tailored nominally to 0.05 wt.%. It was then determined by ICP-OES to be 0.0537 wt.%. The as-cast alloy did not show the segregation of yttrium or the formation of $Fe_{17}Y_2$ intermetallic phase, and a homogenous iron matrix was detected.

4.4.2 Oxidation of Fe-16Cr-0.2Al-0.05Y alloy with VO/V_2O_3 oxygen buffer

The alloy, prepared based on the strategies mentioned in the previous section (4.4.1), was subjected to oxidation by directly contacting the alloy with powder mixture (VO/V_2O_3) for a duration of 20 hours at 1450 °C. In the sample, an internally oxidized zone was observed (Fig. 60). In the outer regions of the sample, coarser particles were found, while finer particles were formed in the inner regions.

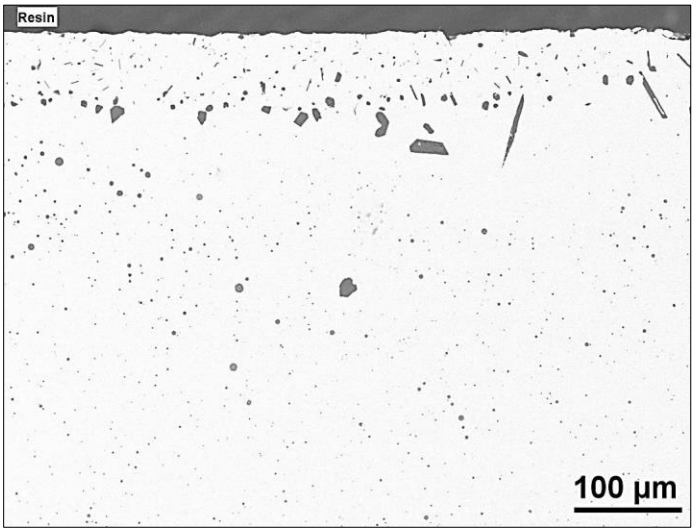

Fig. 60 The internally oxidized zone of Fe-16Cr-0.2Al-0.05Y alloy with (VO/V_2O_3) buffer for 20 h at 1450 ˚C on a surface approximately through the middle of sample (after 2 mm grinding from one side of cubic sample). The SEM images were cross-section backscattered-micrographs. The coarser oxide particles near the surface and finer oxide particles in the inner regions could be seen.

The distribution of particles diameters in image (Fig. 60) was analyzed with the same procedure described for Fe-16Cr-0.2Al with ImageJ software [123], and the cumulative distribution was then calculated and depicted in Fig. 61.

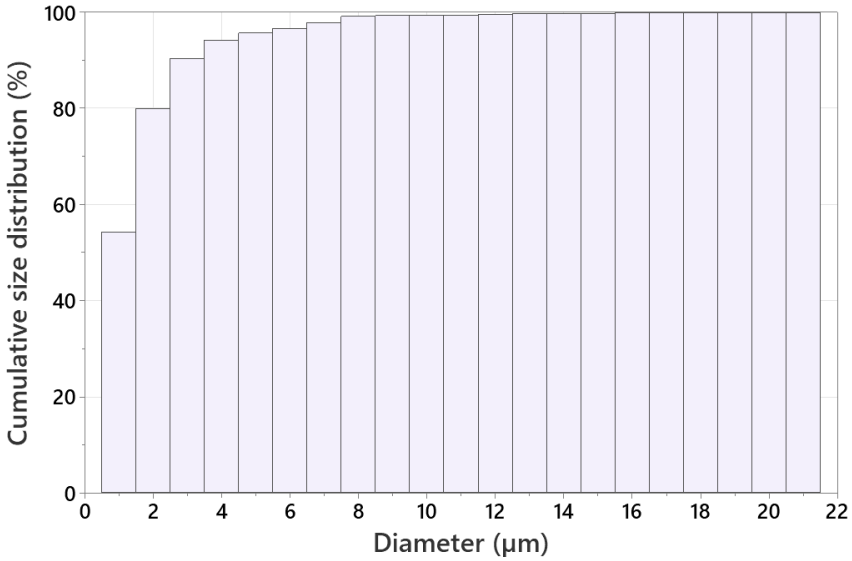

Fig. 61 The cumulative size distribution of particles in Fe-16Cr-0.2Al-0.05Y (wt.%) after oxidation with (VO/V_2O_3) buffer for 20 h at 1450 ˚C.

The mean value of the particles diameters was calculated to be 1.9 µm (standard deviation was 1.8). The size of particles varied between 0.6 µm and 20.8 µm and about 95% of the particles had a diameter of less or equal to 5 µm.

The particles mean spacing (L), approximated using the same strategy as described in section 4.3.3, is presented along with their standard error in Fig. 62. It was observed that in Fe-16Cr-0.2Al-0.05, at distances near the surface ($\Delta x \leq 300$ µm), the mean spacing was higher than in Fe-16Cr-0.2Al (refer to Fig. 45). This could be attributed to the presence of coarser particles near the surface. Furthermore, the mean spacing at greater distances from the surface approached that in the Fe-16Cr-0.2Al alloy. The number of particles per unit volume and its variation with the distance (Δx) within the internal oxidation zone can then be calculated using particle spacing measurements. This issue is discussed in section 4.5 and presented for both alloys (Fe-16Cr-0.2Al and Fe-16Cr-0.2Al-0.05Y).

Moreover, the standard error of particle spacing for this alloy was higher than that obtained in Fe-16Cr-0.2Al (Fig. 45). This difference could be attributed to the presence

of finer particles in Fe-16Cr-0.2Al-0.05Y. After applying three different thresholding methods, the scattering of the measured mean spacing increased, leading to a rise in the standard error.

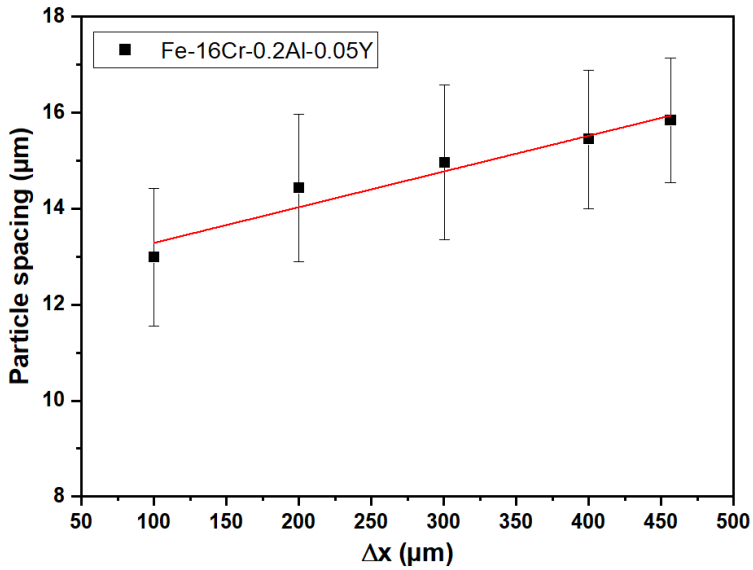

Fig. 62 Variation of particles spacing and the standard error within oxidation zone for Fe-16Cr-0.2Al-0.05Y after intern oxidation at 1450 ˚C.

A typical EDX line scan profile for coarser particles (mostly near the surface of the specimen) is shown in Fig. 63. As suggested by the EDX profile in Fig. 63, the coarser particles (with about a few micrometers in size) were aluminum-oxide.

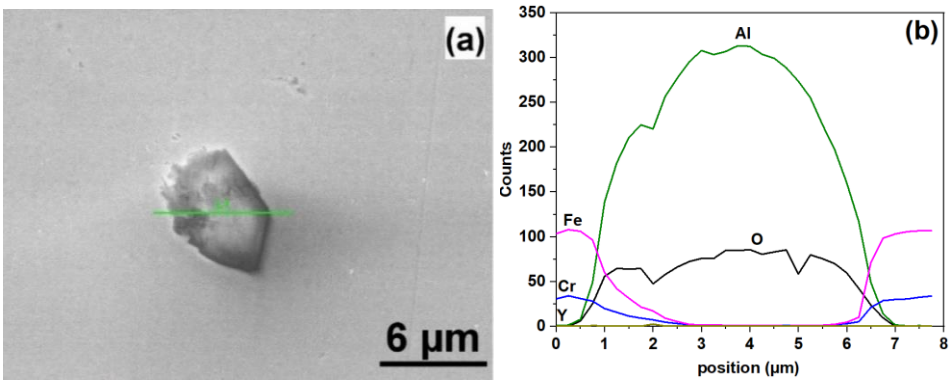

Fig. 63 A typical EDX analysis for the coarser formed particles in Fe-16Cr-0.2Al-0.05Y at 1450 ˚C in outer regions of the sample after 20 h embedded in (VO/V_2O_3) oxygen buffer: (a) secondary electrons micrograph and indicated path for line scan, (b) the corresponding composition profile using 15 kV acceleration voltage showed the formation of aluminum-oxide particle.

The finer oxide particles (approximately some hundred nanometers) were found mainly in the interior of the sample consisting of mixed aluminum-yttrium oxides (Fig. 64).

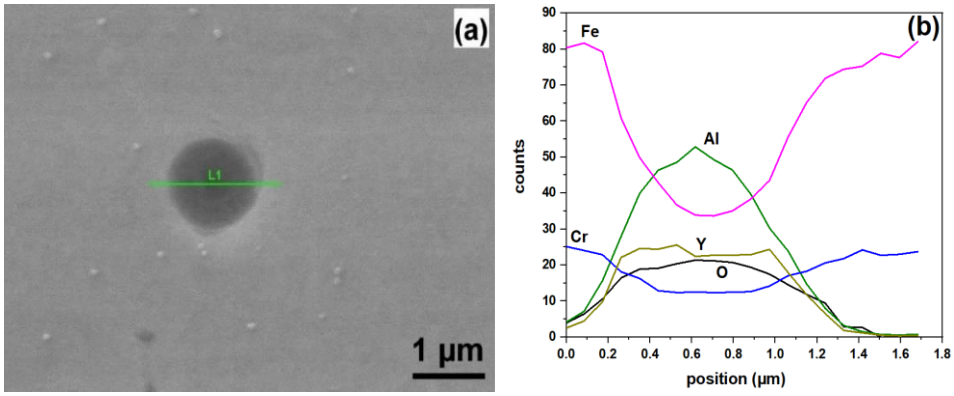

Fig. 64 A typical EDX analysis for the finer formed particles in Fe-16Cr-0.2Al-0.05Y at 1450 ˚C located mainly in inner regions of the sample after 20 h embedded in (VO/V_2O_3) oxygen buffer: (a) secondary electrons-micrograph and indicated path for line scan, (b) the corresponding composition profile using 15 kV acceleration voltage showing mixed aluminum-yttrium oxide particle.

The number of counts for Fe and Cr in the middle of the path did not go down to zero (see Fig. 64 b). This effect could be attributed to the small size of the particle which was in the range of the volume activated by the electron beam, leading to contributions from the surrounding steel matrix. The internal oxidation depth was reported to be approximately 2000 µm similar to Fe-16Cr-0.2Al discussed in section 4.3.3. The observed results showed the formation of desirable oxides particles (Al-O and Al-Y-O precipitates) in examined steels and external scales were not detected for the alloy as well. This type of oxides (Al-Y-O particles) were also present in semi-commercialized PM2000 of type Fe–19Cr–5.5Al–0.5Ti–0.5Y_2O_3 (wt.%) [135]. The obtained results revealed that adding an incredibly low amount of Y into the alloy promoted the nucleation sites and facilitated the formation of finer oxide particles in the steel (the mean value of particles diameters in Fig. 44 for Fe-16Cr-0.2Al was 4.1 µm, while in Fig. 61 for Fe-16Cr-0.2Al-0.05Y it was 1.9 µm). However, the amount of Y had to be less than the maximum solubility of Y in the matrix to prevent the formation of $Fe_{17}Y_2$ phase.

It might be interesting to mention that in the results observed for both alloys (Fe-16Cr-0.2Al in section 4.3.3 and Fe-16Cr-0.2Al-0.05Y in section 4.4.2), minimal agglomeration of oxides was observed. In Appendix 10, a comparative study in terms of agglomeration of non-metallic particles within a steel matrix is provided.

4.5 Tensile tests

The mechanical testing was performed for two internally oxidized samples based on two Fe-Cr-Al and Fe-Cr-Al-Y alloys. The nominal and measured compositions for these two alloys with their reported standard deviations are given in Table 11. The ICP-OES measurements for each alloy were repeated three times.

Table 11. The composition of prepared alloys after cold rolling for the tensile tests.

Alloy designation	Nominal composition (wt.%)				Chemical analysis (wt.%)			
	Y	Al	Cr	Fe	Y	Al	Cr	Fe
Fe-16Cr-0.2Al	-	0.2	16.0	83.8	-	0.153 ± 0.001	15.84 ± 0.04	82.3 ± 0.3
Fe-16Cr-0.2Al-0.05Y	0.05	0.2	16.0	83.75	0.0286 ± 0.003	0.209 ± 0.001	15.78 ± 0.04	82.1 ± 0.2

The cold rolled steel was divided into multiple parts to investigate the effect of annealing on grain orientation. One representative microstructure of the Fe-16Cr-0.2Al alloy after cold rolling and subsequent annealing at 1000 °C for 3 hours was examined. Initially, the grains showed an orientation in the direction of rolling. However, after the annealing process, the previously oriented grains disappeared, indicating a loss of preferred orientation. This phenomenon is seen in Fig. 65. The cold rolled sample was cut into more parts, as mentioned above and therefore the widths in Fig 65 a (after rolling) and in Fig. 65 b (after annealing) became different. The later internal oxidation at 1450 °C (discussed in sections 4.3.3 and 4.4.2) led to the growth of the grains into millimeter ranges but it provided at the same time the nucleation of oxides inside the grains and along the boundaries.

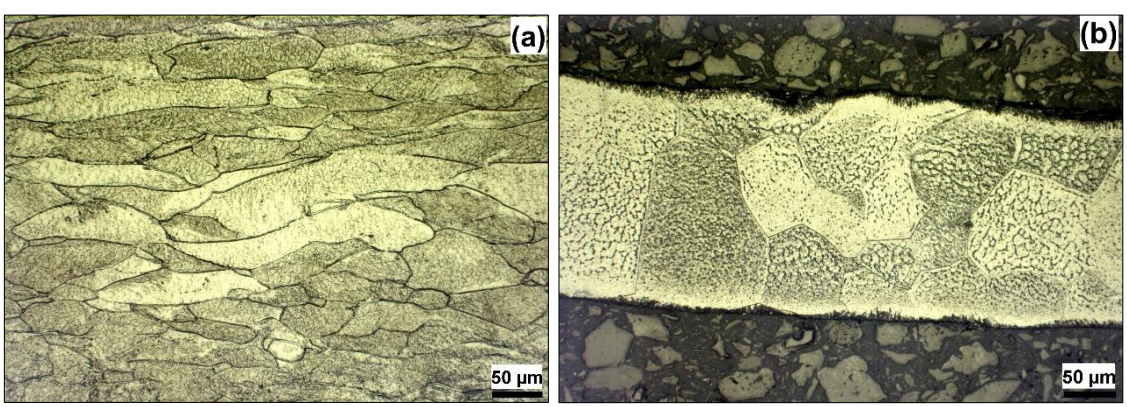

Fig. 65 The microstructure of Fe-16Cr-0.2Al alloy: (a) after rolling, (b) after annealing at 1000 °C for 3 hours.

The Ultimate Tensile Strength (UTS) value of a reference tensile sample (Fe-16Cr-0.2Al) without any internal oxidation was reported to be 179 MPa. Typical tensile tests performed at room temperature for both internally oxidized alloys (1450 °C for 5 hours) are shown in Fig. 66.

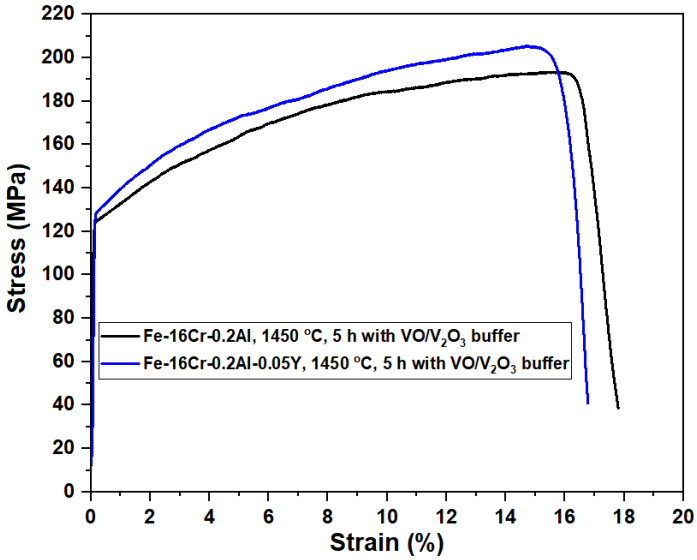

Fig. 66 The comparison of the mechanical testing for both Fe-16Cr-0.2Al and Fe-16Cr-0.2Al-0.05Y after internal oxidation at 1450 °C for 5 hours with VO/V_2O_3 buffer.

The internally oxidized Fe-16Cr-0.2Al-0.05Y alloy exhibited a slightly better performance in terms of Ultimate Tensile Strength (UTS) with a value of 205 MPa compared to the internally oxidized Fe-16Cr-0.2Al alloy with the UTS of 193 MPa. However, the difference between the two was not substantial. The observed UTS values of reference and internally oxidized samples are summarized in Table 12. The reported values highlighted that the tensile strengths of internally oxidized samples were improved than the sample without any internal oxidation.

Table 12. The summary of recorded UTS values for a reference sample and internally oxidized samples.

Alloy designation	Description	Recorded UTS value (MPa)
Fe-16Cr-0.2Al	Reference tensile sample (not internally oxidized)	179
Fe-16Cr-0.2Al	Internally oxidized at 1450 °C for 5 hours with VO/V_2O_3 buffer	193
Fe-16Cr-0.2Al-0.05Y	Internally oxidized at 1450 °C for 5 hours with VO/V_2O_3 buffer	205

To quantify the number of particles in the internally oxidized samples, after Böhm et al. [136], the number of oxide particles per unit volume (Z) has an inverse cubic relationship with the particle spacing (L). This can be for each distance (Δx) within the internal oxidation zone noted as:

$$Z \approx \frac{1}{L^3} \qquad (89)$$

The average particle spacing, obtained after three measurements at each distance, for both alloys (Fe-16Cr-0.2Al and Fe-16Cr-0.2Al-0.05Y), was approximated and presented in Fig. 45 and Fig. 62. Based on that, Z values for each measurement could be calculated. The results, including the average particle numbers per volume and their corresponding standard errors along with the linear fit, are given in Fig. 67. It is observed that at a distance of approximately 412 µm, the calculated average Z values for both alloys approached each other. Specifically, the calculated average Z values for Fe-16Cr-0.2Al and Fe-16Cr-0.2Al-0.05Y alloys at 400 µm were $2.9 \times 10^5\ mm^{-3}$ and $3.1 \times 10^5\ mm^{-3}$, respectively. Beyond approximately 412 µm, the Z value in the Fe-16Cr-0.2Al-0.05Y alloy surpassed that in the Fe-16Cr-0.2Al alloy.

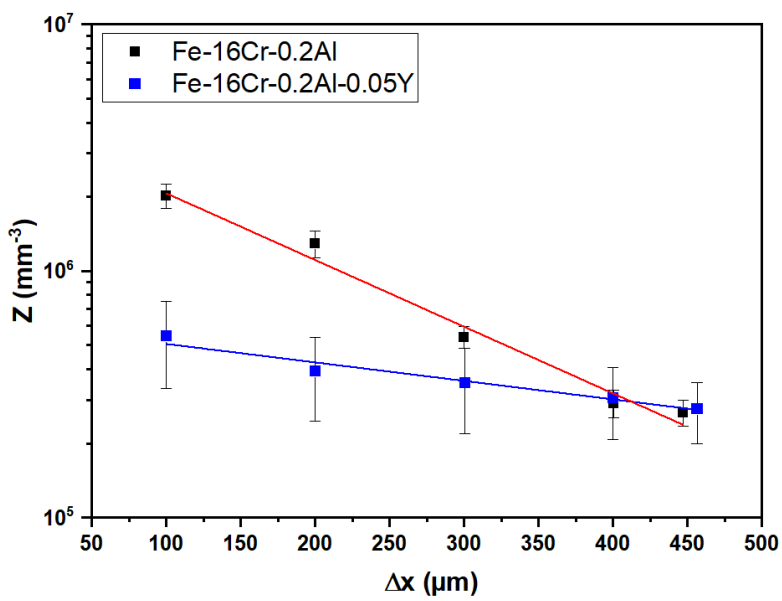

Fig. 67 Particle numbers per unit volume (mm^{-3}) and their standard error as a function of distance within the internal oxidation zone (Δx) for Fe-16Cr-0.2Al and Fe-16Cr-0.2Al-0.05Y alloys after internal oxidation at 1450 °C.

According to Smallman et al. [40], even when the dispersion of the precipitate is coarse, a greater applied stress is necessary to force a dislocation past the obstacles than

would be the case if the obstruction were not present. Based on this and the calculated Z values for both alloys in Fig. 67, it could be inferred at least why higher UTS values were observed for the internally oxidized samples compared to non-internally oxidized sample in this study (see again Table 12).

To argue the mechanical properties of ODS steels produced by the classical powder metallurgy route and compare them to the results in this work, some previous works on ODS steels were studied (Table 13). The works of Gräning et al. [137], Kumar et al. [138], Hoffmann et al. [139] and Gong et al. [140] were reviewed to obtain the UTS values at room temperature.

Table 13. The reported UTS values of ODS steels produced with powder metallurgy route in the literature.

Published work	Chemical composition of steel (wt.%) (most important elements were noted here)	Temperature of mechanical testing (°C)	UTS (MPa)
Gräning et al. [137]	Fe-16.1Cr-14.0Ni-0.15Ti-0.19Y-1.6W-0.7V	20	~ 800
Kumar et al. [138]	Fe-18Cr-2W-0.2Ti-0.3Y_2O_3	Room Temperature	~ 657
Hoffmann et al. [139]	Fe13Cr-1W-0.3Ti-0.3 Y_2O3	20	~ 1211
Gong et al. [140]	Fe-14Cr-0.5Ti-1W-0.35Y_2O_3	25	~ 1016

The achieved UTS values in this work were found to be about 17% to 31% of the reported UTS values for ODS steels at room temperature. To explain this deviation, the following factors must be considered:

a) Size distribution of the particles: The size distribution of the oxide particles in this work was studied earlier and mentioned that the minimum size of oxides was around 0.6 µm (600 nm). In Fe-16Cr-0.2Al-0.05Y alloy, the majority (about 95%) of particles had diameters ranging from 0.6 µm to 5 µm. In comparison, the size of the particles in ODS steels produced with the powder metallurgy route was much finer. For instance, in the work of Gräning et al. [137], almost above 95% of the particles were smaller than 50 nm. In the work Gong et al. [140], all particles were less than 33 nm in size.

b) Role of alloying elements: The alloys in this study primarily consisted of Cr as the alloying element. In contrast, ODS steels produced via powder metallurgy method often incorporate additional alloying elements such as W, Ti, and Ni, which can contribute to improved mechanical properties. This could explain the enhanced UTS values of ODS steels reported in literature compared to the alloys examined in this work.

According to the above argument, it could be explained why UTS values in the current work were comparatively lower than those in other ODS steels produced with powder metallurgy route. One primary strategy to advance the mechanical properties of internally oxidized steels would be refining the oxide particle sizes. This might be done by adding less noble metals like Ti or Zr.

The phase diagram of Fe-Ti in the iron-rich side was calculated using Thermo-Calc software with the database developed by Hu et. al [141]. The maximum solubility of Ti in Fe was then calculated and shown in Fig. 68. The maximum molar fraction of Ti dissolved in Fe at 1293 °C is about 0.096 or 9.6 at.% (8.3 wt.%).

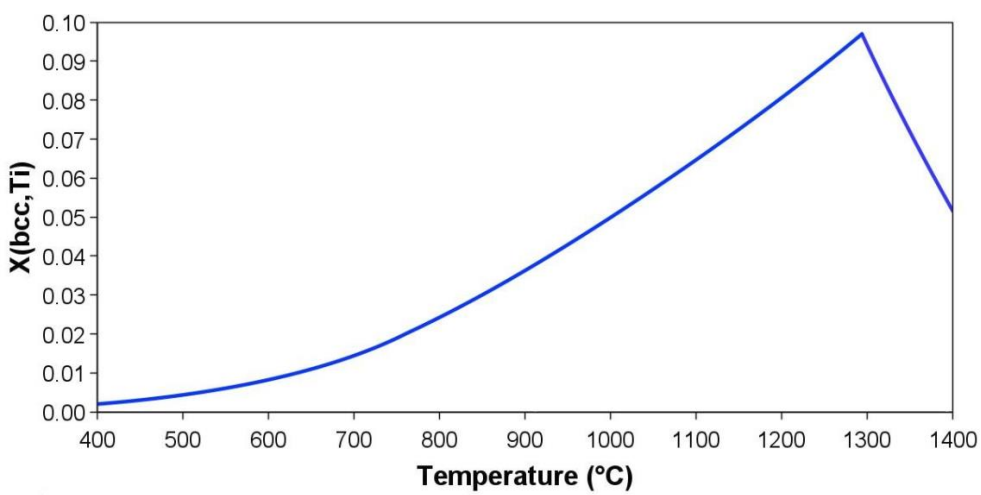

Fig. 68 The calculated maximum solubility of Ti in iron in molar fraction shown as X(bcc, Ti) at different temperatures using the database developed by Hu et al. [141].

The addition of this element (Ti) into steel might lead to the formation of very stable and complex oxides (Al-Ti-O or Y-Ti-O) and may refine the oxide sizes. Therefore, enhanced mechanical properties would be expected. However, the extension of the obtained results in this work to the elements like Ti might need comprehensive study on

complex systems such as Fe-Cr-Al-Y-Ti-O. Understanding the thermodynamics and kinetics of this system becomes crucial for accurately predicting the behavior and performance of Ti-containing alloys, regarding the oxide formation and mechanical properties.

Chapter 5. Conclusions and Outlook

The objective of this study was to investigate an alternative route of production (i.e. internal oxidation method) for ODS steel with the help of computational thermodynamics and kinetics, and how successful selective oxidation of Cr-steel would be. In the first step of the project, different alloys of Fe-Cr-Al-(Y) were prepared through arc-melting and subsequently subjected to oxidation using metal/oxide or oxide/oxide powder mixtures, known as buffer system. The oxidation step was carefully planned and optimized based on simulations conducted with Thermo-Calc and DICTRA software. The oxidation experiments were performed either within a quartz glass ampoule (no contact between sample and buffer) or in a vertical high temperature furnace (direct contact between sample and buffer). The main findings of this work can be summarized as follows:

1) The oxidation of Fe-16Cr-0.2Al and Fe-9Cr-0.2Al alloys (in wt.%) in quartz glass ampoule after seven days of exposure to Fe/FeO buffer at 1000 °C led to the external oxidation of alloy (supplied oxygen activity was $10^{-14.9}$). The oxides formed were FeO and Fe/Cr spinels emphasizing the impact of increased oxygen activity on the studied alloys. The presented thermodynamic modelling in this step was consistent with the obtained results.
2) A further oxidation experiment was conducted under the same conditions in quartz glass ampoule with V_2O/VO buffer for both alloys with oxygen activity of $10^{-24.5}$. This experiment successfully resulted in the formation of discrete Al-O oxide particles. The internally oxidized zone (IOZ) in both alloys was limited to a narrow range, varying from a few dozen micrometers to a few hundred micrometers. To achieve a greater oxidation depth, higher temperatures and direct contact of buffers and samples were employed in the next set of experiments.
3) By employing VO/V_2O_3 buffer system, a higher oxygen activity ($10^{-15.0}$) at 1300 °C was provided. In Fe-16Cr-0.2Al, after 20 hours, an IOZ depth of about 100 µm was detected, whereas the calculated IOZ depth was about 42 µm. Subsequently, in a further experiment performed at 1450 °C under the same conditions, an IOZ depth of approximately 2000 µm was obtained, with the

presence of Al-O based particles. The theoretical IOZ depth based on Wagner's theory was approximately 647 µm. The average diameter of particles was 4.1 µm, with sizes ranging between 0.9 µm and 12.2 µm. Notably, around 70% of the particles had a diameter of 5 µm or less. This analysis revealed that the formation of relatively larger oxide particles occurred through internal oxidation, when only Al was present as the oxide-forming element.

4) The disparity between the calculated internally oxidized zone (IOZ) based on Wagner's theory and the observed results in this experiment could be attributed to the presence of an additional alloying element (Cr) that deviated from the assumption of Wagner's theory, which considered the existence of one base metal and one less noble metal. The introduction of Cr into the system caused changes in the solubility value of oxygen, as well as the diffusion coefficients of aluminum and oxygen.
5) To provide insights into the locations of the particles within the grains or grain boundaries, one internally oxidized sample was etched and optically imaged. It was observed that the oxide particles were mainly formed inside the grains rather than at the grain boundaries. The reason for this observation could be explained by the fact that the diffusion through grains was the primary mechanism at the elevated temperature of experiments (1450 °C).
6) Experiments with VO/V_2O_3 under identical conditions for Fe-16Cr-0.2Al-0.05Y alloy also showed IOZ with approximately 2000 µm depth. The mean value of the whole oxide particles was calculated to be 1.9 µm. The particle sizes ranged from 0.6 µm to 20.8 µm, with approximately 95% of the particles having a diameter less than or equal to 5 µm. This experiment indicated that adding a trace amount of Y (nominally 0.05 wt.%) caused an average size reduction of the oxide particles by approximately 54% compared to Fe-16Cr-0.2Al alloy. The presence of Y into the alloy and its strong affinity for oxygen enhances the nucleation sites, and the generation of finer oxide particles is therefore promoted.
7) Mechanical testing was performed on internally oxidized samples of Fe-16Cr-0.2Al and Fe-16Cr-0.2Al-0.05Y alloys that were subjected to a temperature of 1450 °C for 5 hours. The internally oxidized samples exhibited higher ultimate

tensile strength (UTS) values compared to the reference sample that did not undergo internal oxidation. The highest recorded tensile strength for the internally oxidized alloys was approximately 205 MPa. It is worth noting that the UTS values obtained in this study ranged from 17% to 31% of the typical UTS values observed for oxide dispersion strengthened (ODS) steels at room temperature. To account for this deviation, two aspects had to be taken into consideration: Firstly, the size distribution of particles played a significant role. In this study, the minimum particle size achieved was approximately 600 nm. For example, in Fe-16Cr-0.2Al-0.05Y alloy, about 95% of particles had diameters ranging from 0.6 µm to 5 µm. In contrast, other ODS steels produced using the powder metallurgy route had particles that were mostly finer than 100 nm. This difference in particle size distribution could contribute to the variation in mechanical properties. Secondly, the role of alloying elements was another factor to consider. In this study, only chromium (Cr) existed as an alloying element, while other ODS steels typically contained additional elements such as tungsten (W), titanium (Ti), and nickel (Ni). The lack of these elements in the studied Fe-16Cr-0.2Al-(0.05Y) alloys could also account for the observed deviation in mechanical properties compared to other ODS steels.

8) In conclusion, internal oxidation can be regarded as an alternative production route for ODS steels. This approach offers the advantage of minimal agglomeration of oxide particles within the matrix. However, to optimize the process, progress is necessary in terms of mechanical properties and oxide sizes. One potential path for further development is the addition of alloying elements such as Ni and W to improve the fundamental mechanical properties of the steel itself. Another strategy to enhance mechanical properties is the incorporation of oxide-forming elements like Ti into the alloy, along with calculation of the proper oxygen activity to achieve a finer mixed oxide particles. Through the implementation of these approaches, it is anticipated that the mechanical properties of ODS steels produced with internal oxidation can be advanced.

Appendix

A1. Publications

1. M. Sarma, S. Miran, I. Grants, G. Gerbeth, Dispersion of nanoparticles in steel melt by superimposed steady and alternating magnetic fields, Conference paper, International conference on heating by electromagnetic sources, 24th – 27th May, (2016), Padova, Italy.
2. S. Miran, P. Franke, A. Möslang, H. J. Seifert, Casting technology for ODS steels - the internal oxidation approach, IOP Conf. Series: Materials Science and Engineering, (2017) 228.

A2. Posters

1. S. Miran, P. Franke, H. J. Seifert, Casting technology for ODS steels, project C4, Poster, Summer school of LIMTECH Alliance, 30th Jun.– 1st Jul., (2015), Karlsruhe.
2. S. Miran, P. Franke, T. Gräning, A. Möslang, H. J. Seifert, Casting technology for ODS steels, project C4, Poster, Mid-term evaluation for LIMTECH Alliance, 28th – 30th Sep., (2015), Dresden.
3. S. Miran, P. Franke, H. J. Seifert, Thermodynamic modelling and experimental investigation of internal oxidation of Fe-Cr-Al alloys, Poster, Annual meeting of LIMTECH Alliance, 16th – 17th Nov. (2015), Hannover.
4. S. Miran, P. Franke, H. J. Seifert, Thermodynamic modelling and experimental investigation of internal oxidation of Fe-Cr-Al alloys, Poster, Summer school of LIMTECH Alliance, 12th – 13th July. (2016), Ilmenau.
5. S. Miran, P. Franke, H. J. Seifert, Thermodynamic modelling and experimental investigation of internal oxidation of Fe-Cr-Al-(Y) alloys, Project: C4 (Casting technology for ODS steels), Annual meeting of LIMTECH Alliance, 3rd – 4th Nov. (2016), Freiberg.
6. S. Miran, P. Franke, H. J. Seifert, Preparation of stainless ODS steels by internal oxidation, 4th International workshop on ODS materials, 26th- 28th Jun. (2017), Dresden.

7. S. Miran, P. Franke, H. J. Seifert, Thermodynamic modelling and experimental investigation of internal oxidation of Fe-Cr-Al-(Y) alloys, Poster, LIMTECH symposium, 19th – 20th Sep. (2017), Dresden.

A3. Presentations

1. S. Miran, P. Franke, H. J. Seifert, Casting technology for ODS steels, 30th Annual meeting Meeting, International Seminar on Heterogeneous Multicomponent Equilibria, 31st Jan.– 5th Feb. (2016), Ringberg castle, Tegernsee.
2. S. Miran, P. Franke, H. J. Seifert, Experimental investigation and thermodynamic calculation of internal oxidation of Fe-Cr-Al alloys, Materials Science and Engineering (MSE), 27th – 29th Sep., (2016), Darmstadt.
3. P. Franke, S. Miran, H. S. Seifert, Preparation of ODS steels by internal oxidation, 4th International Workshop on ODS Materials, 26th -28th June (2017), Dresden.
4. S. Miran, P. Franke, H. J. Seifert, Thermodynamic calculation and experimental investigation of internal oxidation of Fe-Cr-Al-(Y) alloys, Thermo-Calc Anwendertreffen, 31st Aug. – 01st Sep. (2017), Aachen.

A4. Published MSIT (Materials Science International Team) database

1. K. Kumar, S. Miran, N. Kovalenko, I. Bajenova, M. Record, Al-Cr-O Ternary Phase Diagram Evaluation, MSI Eureka Effenberg, G. (Ed.), MSI, Materials Science International, Stuttgart (2016), Document ID: 10.15070.1.2 .

A5. Calculated oxygen activity versus temperature in Fe-O system

Fig. 69 shows the calculated oxygen activity versus temperature in Fe-O system based on database developed by Kjellqvist et al. [89]. The iron oxides can be categorized into $Fe_{1-x}O$ (Halite), Fe_3O_4 (Spinel) and Fe_2O_3 (Corundum). Fe-O system is particularly important in steel making industries because iron ore is normally mixture of hematite (corundum) and magnetite (spinel).

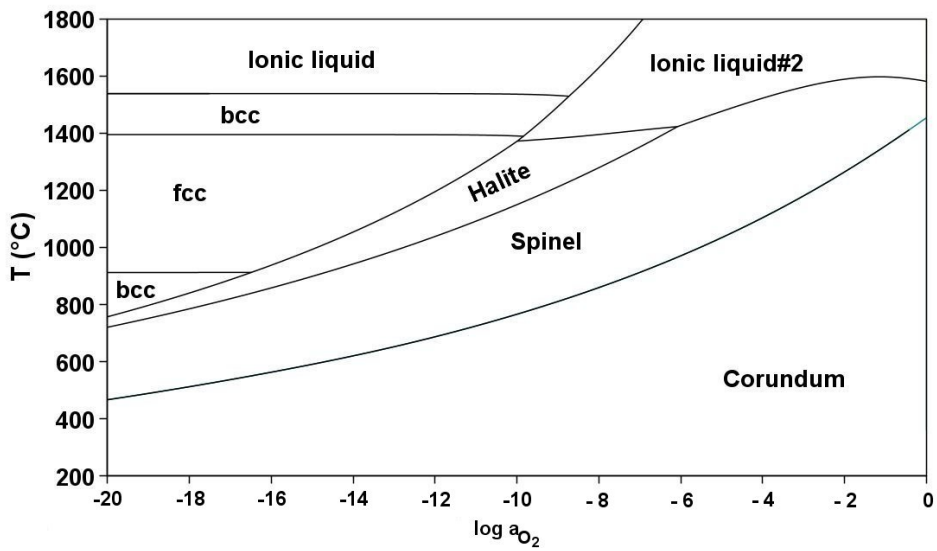

Fig. 69 The calculated oxygen activity versus temperature in Fe-O system using the database developed by Kjellqvist et al. [89].

A6. Calculated Standard Gibbs energy of formation for relevant equilibria in V-O system

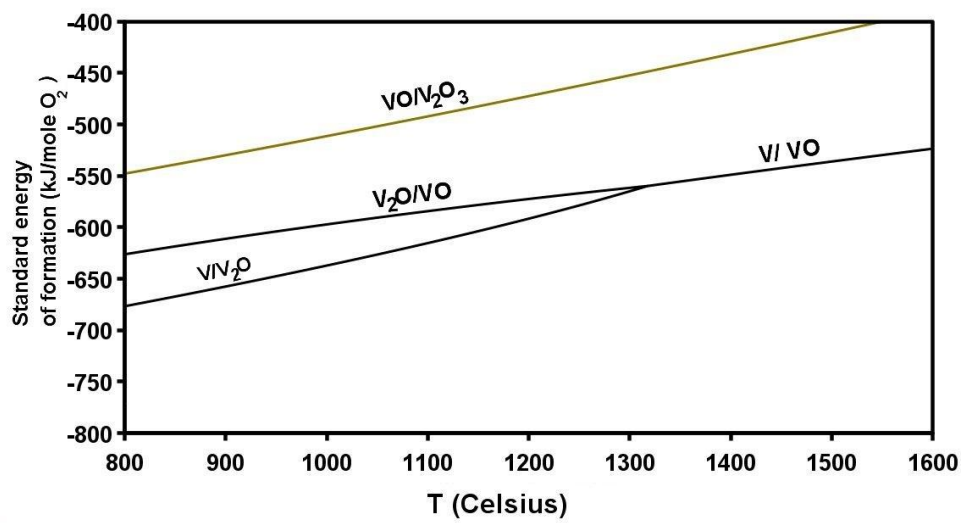

Fig. 70 Calculated standard Gibbs energy of formation for relevant equilibria in this work using the database of Yang et al. [92].

A7. The results of EDX analyses for impurities

A typical EDX spectrum for the analyses for as-cast alloys is shown in Fig. 71.

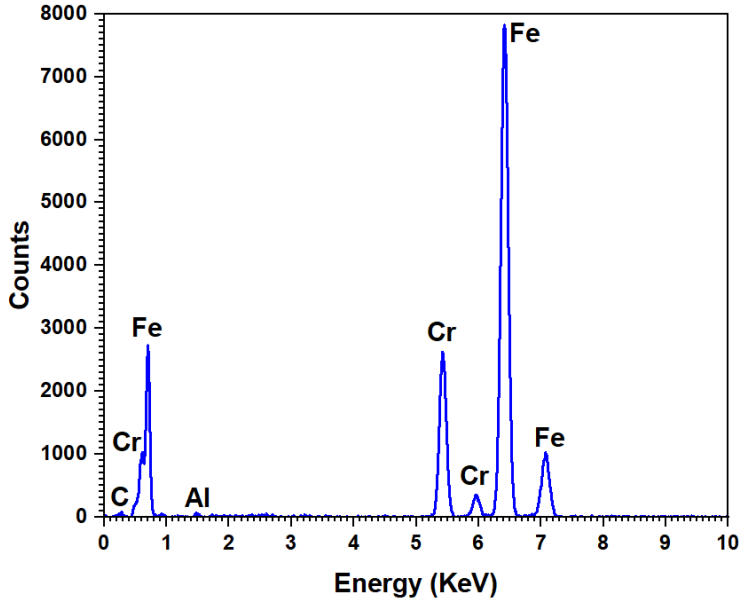

Fig. 71 A typical EDX spectrum for as-cast alloys.

In the quantitative results of EDX analyses, only C and O were considered as impurities, and the calculated results (in wt.%) are given in Table 14. It is noteworthy to mention that the carbon results can originate from contamination within the SEM chamber, potential organic materials on the surface, etc., and may not necessarily reflect the true carbon content of the alloy.

Table 14. The quantitative results of EDX analyses for impurities.

Spot Number	C (wt.%)	O (wt.%)
01	2.66	0.00
02	2.73	0.00
03	3.20	0.00
04	3.63	0.00

A8. The interstitial diffusion coefficients in Fe

The diffusion coefficients of oxygen, carbon and nitrogen in Fe are given by Heumann et al. [128] and shown in Fig. 72. This data was used to approximate the diffusion coefficient of O in Fe at 1450 °C.

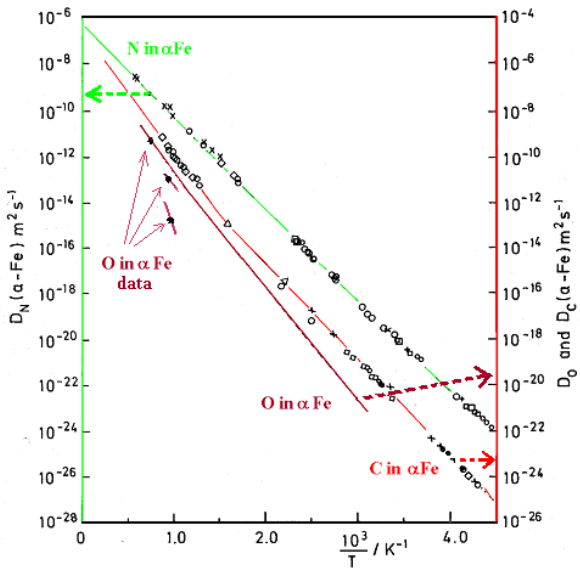

Fig. 72 The reported data for interstitial diffusion coefficients in Fe after Heumann et al. [128]

A9. The substitutional diffusion coefficients in bcc-iron

The substitutional diffusion coefficients in bcc-iron are given by H. Oikawa [129] (Fig. 73). This data was used to approximate the diffusion coefficient of Al in Fe at 1450 °C.

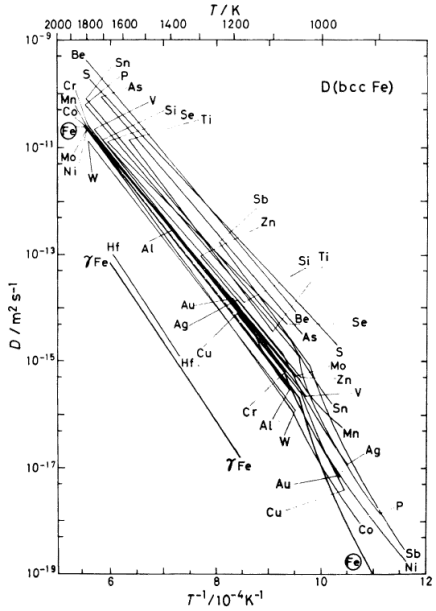

Fig. 73 The reported substitutional diffusion coefficients in Fe after H. Oikawa [129].

A10. The reliability of buffer system for the distribution of non-metallic particles on steel matrix

The appendix presents a comparative study that was conducted as part of a scientific collaboration between the current Ph.D. work at KIT (Karlsruhe Institute of Technology) and HZDR (Helmholtz-Zentrum Dresden-Rossendorf). The purpose of this study was to examine the reliability of internal oxidation in terms of particle distribution or agglomeration within a steel matrix. To address this issue, an example of the distribution of non-metallic particles (TiN particles) in a steel matrix processed using another method was presented, and its distribution pattern was compared to that achieved through the internal oxidation method.

A sample was prepared by a researcher (Martin Sarma) in HZDR by mixing steel powder and TiN nano-powders, followed by melting with induction heating and a parallel application of strong axial magnetic field. The principle of this route was based on the occurrence of cavitation phenomena in molten metal, where the collapse of bubbles could produce micro-scale jets to prevent the agglomeration of non-metallic particles and to trigger their dispersion in metallic matrices. The distribution of non-metallic particles in non-steel matrices using a magnetic field was reported by some researchers mostly for light metals like the work of Kaldre et al. [142] for SiC particles dispersion on Al-6Mg (wt.%) alloy, and SiC dispersion on pure magnesium and its alloys (Mg-2Al-1Si, Mg-4Zn) published by Cao et al. [143].

The theoretical background of magnetic excitation of acoustic cavitations in molten metals were reported by Grants et al. [144] and Li et al. [145]. The non-metallic particles intended for dispersion in the metallic matrix, had to have ideally zero solubilities in the matrix at elevated temperatures. Therefore, phase diagram calculations must be precisely done for the selected systems. In this study, the microstructure analyses, and thermodynamic calculations for the experiments for steel matrix were performed. A steel powder with diameter size of 5-20 µm and a defined chemical composition (Table 15), along with 2 wt.% TiN with diameter size of 800 nm were used in this experiment.

Table 15. The chemical composition of the used steel powder.

Element	C	Si	Mn	Ni	Cr	Mo	P	S	O	Fe
wt. (%)	0.020	0.479	0.075	12.380	16.503	2.629	0.010	0.003	0.337	Bal

The provided sample was examined, and it was observed that the particles were not distributed in the matrix of steel and they were segregated as an agglomerated phase (Fig. 74). This highlighted that the magnetic excitation method was not successful in dispersing non-metallic particles on the matrix of examined steel and agglomeration was a challenge for this method.

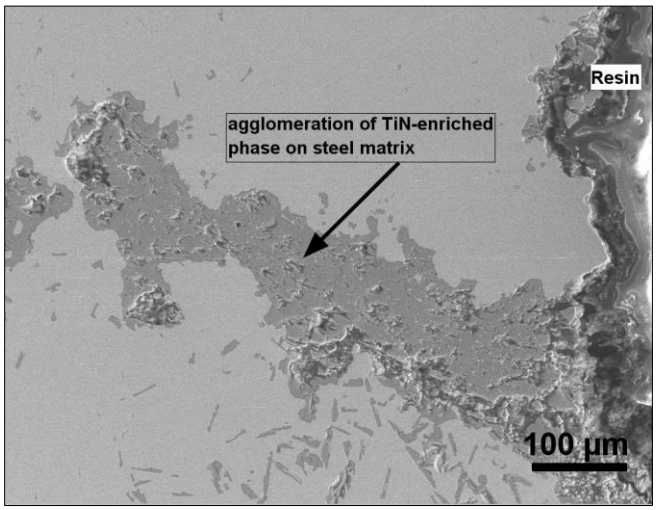

Fig. 74 The agglomeration of particles on steel matrix (SE micrograph using SEM method).

One typical EDX line analysis obtained for the segregated phase revealed the Ti-enriched phase agglomerated on the matrix (Fig. 75). The number of counts for Ti at some spots was decreased and instead the numbers of counts for Mn and S were increased (Fig. 75 b).

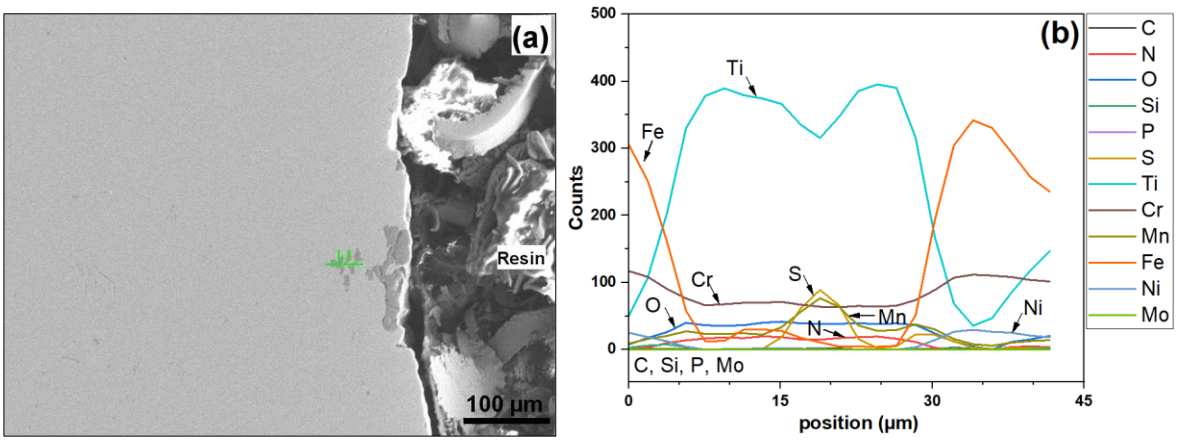

Fig. 75 The segregated phase on steel matrix: (a) SE-micrograph using SEM method, (b) an EDX line scan profile. This result was included in a conference paper (2016) presented in Italy [146].

The presence of Mn and S in EDX profiles could be explained by the fact that in some other spots of the examined steel, MnS (Manganese sulfide) was already clearly found like the one shown in Fig. 76. The formation of MnS in steels was not an extraordinary phenomenon and it had occurred during the production of samples. This could explain why Mn and S elements in the EDX profile of TiN-enriched agglomerated phases in this steel existed (see again Fig. 75 b).

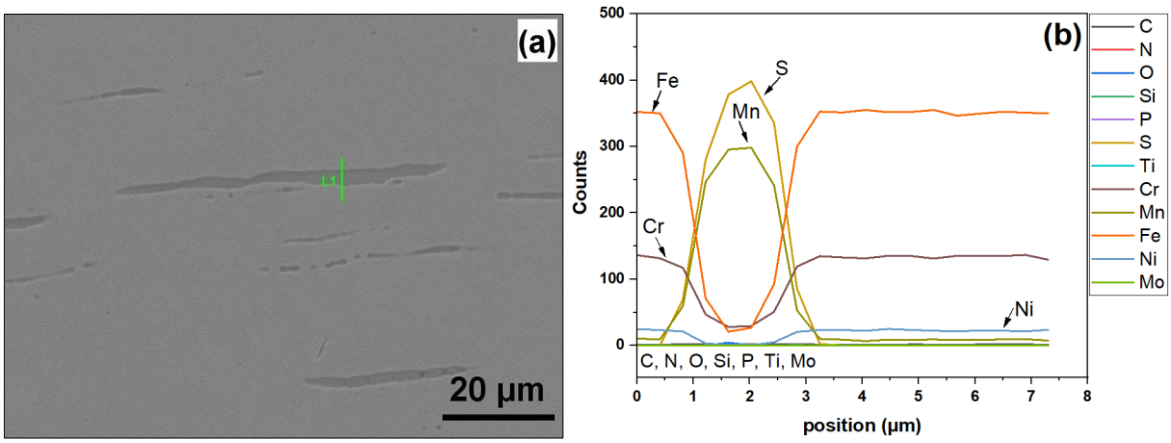

Fig. 76 The segregated phases in other spots of the sample: (a) A SE-micrograph for segregated phases and indicated path for EDX scan (SEM method), (b) The recorded profile suggested the formation of MnS (Manganese sulfide).

In addition to the above characterizations, thermodynamic calculations for the solubility of TiN in the above steel were performed. These calculations were very decisive since the non-metallic particles had to have almost zero solubility in the steel matrix. For example, carbide particles like TiC, WC, and W_2C had some solubility in pure iron, which meant that these types of particles were not suitable candidates for magnetic excitation of acoustic cavitations in steel (see Appendix 11 for the calculated TiC-Fe phase diagram).

To simplify the equilibria calculations for TiN, the phase diagram was initially calculated using TCFE7 [88]. This calculation considered only metallic elements of the steels in this work (listed in Table 15): Fe as the base metal, Cr (16.503 wt.%), Ni (12.380 wt.%), Mn (0.075 wt.%), and Mo (2.629 wt.%).

The resulting phase diagram is illustrated in Fig. 77.

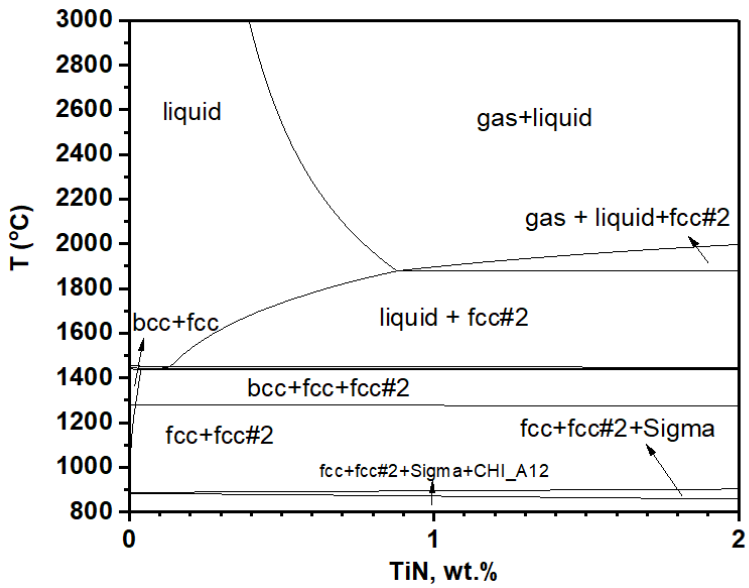

Fig. 77 The calculated phase diagram of stainless steel-TiN up to 2 wt.% TiN. To calculate the phase diagram only the metallic elements (Fe-base, Cr 16.503 wt.%, Ni 12.380 wt.%, Mn 0.075 wt.%, Mo 2.629 wt.%) in stainless steel were considered.

As the phase diagram (Fig. 77) suggested, only one liquid phase with negligible solubility for TiN existed, and almost no solubility at lower temperatures in the steel matrix was seen. Bcc and fcc were ferrite and austenite, respectively. (The description of Sigma, CHI_A12 and fcc#2 is given in Table 16 as well).

Table 16. Sigma, CHI_A12 and fcc#2 and their constituents.

Phase description (SGTE notation)	Phase constituents
Sigma	$(Fe, Cr, Ni, Mn, Mo)_{10}$ $(Cr, Mo, Ti)_4$ $(Fe, Cr, Mn, Mo, Ni, Ti)_{16}$
CHI_A12	$(Fe, Cr, Ni)_{24}$ $(Cr, Mo)_{10}$ $(Fe, Cr, Mo, Ni)_{24}$
fcc#2	$(Fe, Al, Ni, Ti)_{0.75}$ $(Fe, Al, Ni, Ti)_{0.25}$ $(N, VA)_1$

In addition, the phase diagram of TiN up to 2 wt.% into the provided stainless steel, by considering all the elements present in the datasheet (see Table 15 again) was calculated. The calculated phase diagram was extraordinarily complex and included several phases. This is depicted on the next page in Fig. 78.

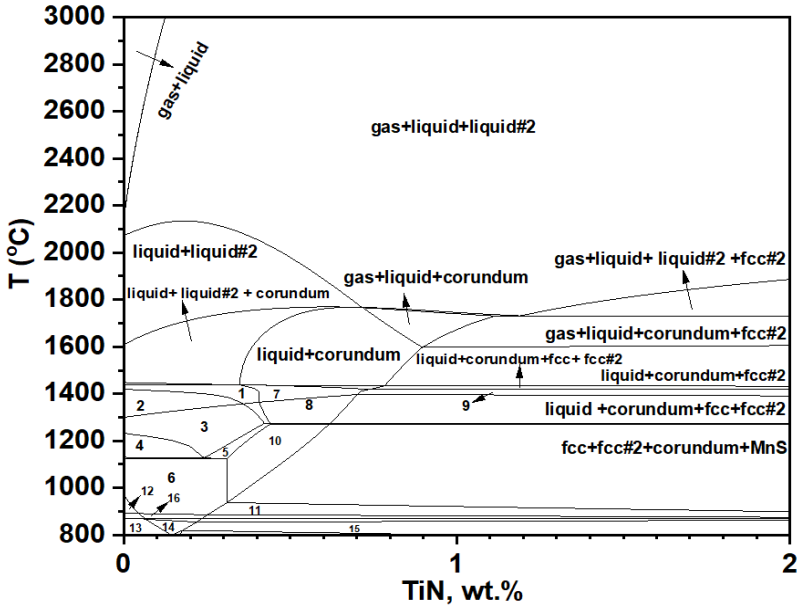

Fig. 78 The calculated phase diagram up to 2 wt.% TiN. To calculate the phase diagram, all the elements present in the datasheet were considered (see Table 15).

The distinct regions of the phase diagram in Fig. 78 were labeled with ID numbers and the stable phases in these regions were noted (see Table 17). In this table, SGTE notations were used to represent each phase.

Table 17. Region IDs and the corresponding phases in shown in Fig. 78.

Region ID	Present phases (SGTE notations for each phase was used)
1	liquid + liquid#2 + bcc + corundum + fcc
2	liquid#2 + bcc + corundum + fcc
3	liquid#2 + corundum + fcc
4	liquid#2 + corundum + fcc + tridymite
5	liquid#2 + corundum + fcc + MnS
6	corundum + fcc + MnS + Tridymite
7	liquid + bcc + corundum + fcc
8	liquid + corundum + fcc
9	liquid + bcc + corundum + fcc + fcc#2
10	corundum + fcc + MnS
11	corundum + fcc + fcc#2 + MnS + Tridymite
12	corundum + fcc + MnS + Tridymite + spinel
13	corundum + fcc + MnS + quartz + spinel + CHI_A12 + $M_{23}C_6$
14	corundum + fcc + MnS + quartz + CHI_A12 + $M_{23}C_6$
15	corundum + fcc + MnS + fcc#2 + quartz + CHI_A12 + $M_{23}C_6$
16	corundum + fcc + MnS + Tridymite + $M_{23}C_6$

To simplify the readability and interpretation of the phase diagram shown in Fig. 78, the SGTE phases in this phase diagram and their phase constituents were given in Table 18. The complex phase diagram shown in Fig. 78 showed almost zero solubility of TiN in the above steel similar to the phase diagram shown in Fig. 77. Both calculated phase diagrams (Fig. 77 and Fig. 78) could then state that TiN was a proper candidate for the distribution within the matrix of the examined steel.

Table 18. The present phases in Table 17 with their SGTE notations and their constituents.

Phase description (SGTE notation)	Phase constituents
liquid	(Fe, FeO, $FeO_{3/2}$, FeS, Al, AlN, $AlO_{3/2}$, Cr, $CrO_{3/2}$, Mn, MnO, $MnO_{3/2}$, MnS, Mo, N, Ni, NiO, NiS, P, S, Si, SiO_2, Ti, TiO, TiO_2, $TiO_{3/2}$)
liquid#2 or Ionic liquid	$(Fe^{+2}, Al^{+3}, Cr^{+3}, Mn^{+2}, Mo^{+2}, Ni^{+2}, Si^{+4})_p$ $(O^{-2}, S^{-2}, SiO_4^{-4}$, AlN, $AlO_{3/2}$, $FeO_{3/2}$, $MnO_{3/2}$, N, P, S, $SiN_{4/3}$, SiO_2, $VA)_q$
bcc	$(Fe, Al, Cr, Mn, Mo, Ni, P, S, Si, Ti)_1$ $(N, C, O, VA)_3$
corundum	$(Fe^{+2}, Fe^{+3}, Al^{+3}, Cr^{+2}, Cr^{+3}, Mn^{+3}, Ti^{+3})_2$ $(Cr^{+3}, Fe^{+3}, Ni^{+2}, VA)_1$ $(O^{-2})_3$
fcc	$(Fe, Al, Cr, Mn, Mo, Ni, P, S, Si, Ti)_1$ $(C, N, O, VA)_1$
tridymite	SiO_2
MnS	$(Mn, Fe)_1$ $(S)_1$
fcc#2	$(Fe, Al, Ni, Ti)_{0.75}$ $(Fe, Al, Ni, Ti)_{0.25}$ $(N, VA)_1$
spinel	$(Fe^{+2}, Fe^{+3}, Al^{+3}, Cr^{+2}, Cr^{+3}, Mn^{+2}, Ni^{+2})_1$ $(Fe^{+2}, Fe^{+3}, Al^{+3}, Cr^{+3}, Mn^{+2}, Mn^{+3}, Mn^{+4}, Ni^{+2}, VA)_2$ $(O^{-2})_4$
quartz	SiO_2
CHI_A12	$(Fe, Cr, Ni)_{24}$ $(Cr, Mo)_{10}$ $(Fe, Cr, Mo, Ni)_{24}$
$M_{23}C_6$	$(Fe, Cr, Mn, Ni)_{20}$ $(Fe, Cr, Mn, Mo, Ni)_3$ $(C)_6$

It was here interesting to compare the distribution of non-metallic particles in the above steel with the obtained distribution of particles in the alloys presented in earlier sections. Non-metallic particles with negligible solubility in the steel (as shown in Fig. 74) were agglomerated using magnetic excitation of acoustic cavitations but the particles using internal oxidation were distributed in the matrix of steel (see again for example Fig. 43 or Fig. 60). It might be argued that the direct comparison of the distribution of nitride particles using the magnetic field with the distribution of oxide particles with internal oxidation would be weird. To resolve this issue, it had to be considered that the distribution of particles with magnetic excitation method depended directly on the solubilities of particles in the steel matrix, and not the type of particles

(oxides, nitrides, …). Therefore, the comparison of the two methods (magnetic excitation and internal oxidation) with distribution view of the point was here explanatory. This study highlighted that almost no agglomeration using oxygen buffer system could be expected and would be one advantage of the internal oxidation method.

A11. TiC-Fe phase diagram

The calculated TiC-Fe phase diagram using TCFE7 [88] database is given in Fig. 79. Some solubility of TiC in iron at higher temperatures can be seen.

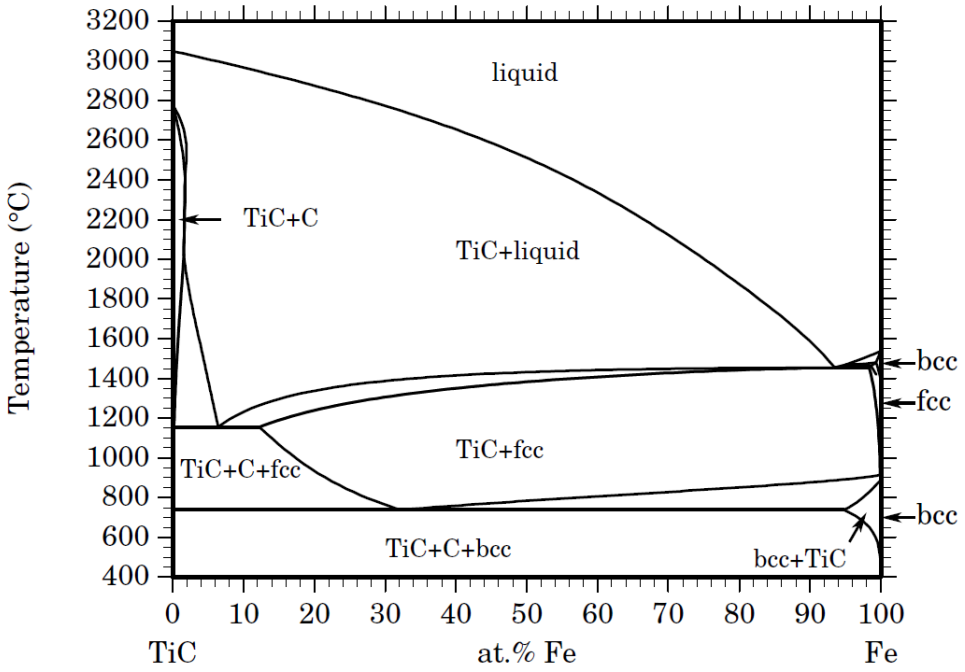

Fig. 79 The calculated TiC-Fe phase diagram using TCFE7 [88] database.

References

1. R.F. Mattas, B.A. Loomis, D.L. Smith, Vanadium alloys for fusion reactor applications, The Journal of The Minerals, Metals & Materials Society. 44 (1992) 26-29.
2. R. Pampin, A. Davis, J. Izquierdo, D. Leichtle, M.J. Loughlin, J. Sanz, A. Turner, R. Villari, P.P.H. Wilson, Developments and needs in nuclear analysis of fusion technology, Fusion Engineering and Design. 88 (2013) 454-460.
3. T. Hamacher, M. Huber, J. Dorfner, K. Schaber, A.M. Bradshaw, Nuclear fusion and renewable energy forms: Are they compatible?, Fusion Engineering and Design. 88 (2013) 657-660.
4. V. Glukhikh, O. Filatov, B. Kolbasov, Fundamentals of magnetic thermonuclear reactor design. (2018) Woodhead Publishing.
5. Z. Soti, J. Magill, R. Dreher, Karlsruhe nuclide chart – new 10th edition 2018, EPJ Nuclear Sci. Technol. 5 (2019) 1-11.
6. F. Dobran, Fusion energy conversion in magnetically confined plasma reactors, Progress in Nuclear Energy. 60 (2012) 89-116.
7. A. Bouhaddane, V. Slugen, S. Sojak, J. Veterníková, M. Petriska, I. Bartošová, Investigation of materials for fusion power reactors, Journal of Physics: Conference Series. 516 (2014).
8. E.E. Bloom, R.W. Conn, J.W. Davis, R.E. Golo, R. Little, K.R. Schultz, D.L. Smith, F.W. Wiffen, Low activation materials for fusion applications. Journal of Nuclear Materials. 122 (1984) 17-26.

9. E. E. Bloom, The challenge of developing structural materials for fusion power systems, Journal of Nuclear Materials. 258-263 (1998) 7-17.

10. T. Muroga, M. Gasparotto, S.J. Zinkle, Overview of materials research for fusion reactors, Fusion Engineering and Design. 61-62 (2002) 13-25.

11. R.H. Jones, H.L. Heinisch, K.A. McCarthy, Low activation materials, Journal of Nuclear Materials. 271-272 (1999) 518-525.

12. K. Ehrlich, Materials research towards a fusion reactor, Fusion Engineering and Design. 56-57 (2001) 71-82.

13. D.L. Smith, M.C. Billone, K. Natesan, Vanadium-base alloys for fusion first-wall/blanket applications, International Journal of Refractory Metals & Hard Materials. 18 (2000) 213-224.

14. T. Muroga, J.M. Chen, V.M. Chernov, R.J. Kurtz, M. Le Flem, Present status of vanadium alloys for fusion applications, Journal of Nuclear Materials. 455 (2014) 263-268.

15. T. Muroga, Vanadium for nuclear systems, Reference Module in Materials Science and Materials Engineering. (2016).

16. M. Li, X. Zhou, H. Yang, S. Du, Q. Huang, The critical issues of SiC materials for future nuclear systems, Scripta Materialia. 143 (2017) 149-153.

17. Y. Katoh, L.L. Snead, C.H. Henager, T. Nozawa, T. Hinoki, A. Ivekovic´, S. Novak, S.M. Gonzalez de Vicente, Current status and recent research achievements in SiC/SiC composites, Journal of Nuclear Materials. 455 (2014) 387-397.

18. K. Shiba, H. Tanigawa, T. Hirose, H. Sakasegawa, S. Jitsukawa, Long-term properties of reduced activation ferritic/martensitic steels for fusion reactor blanket system, Fusion Engineering and Design. 86 (2011) 2895-2899.

19. L. Tan, Y. Yang, J.T. Busby, Effects of alloying elements and thermomechanical treatment on 9Cr Reduced Activation Ferritic–Martensitic (RAFM) steels, Journal of Nuclear Materials. 442 (2013) S13-S17.

20. M. Okada, T. Noda, F. Abe, On the development of low-activation materials for fusion reactors, Journal of Nuclear Materials. 169 (1989) 249-256.

21. K. Laha, S. Saroja, A. Moitra, R. Sandhya, M.D. Mathew, T. Jayakumar, E. Rajendra Kumar, Development of India-specific RAFM steel through optimization of tungsten and tantalum contents for better combination of impact, tensile, low cycle fatigue and creep properties, Journal of Nuclear Materials. 439 (2013) 41-50.

22. T. Hasegawa, Y. Tomita, A. Kohyama, Influence of tantalum and nitrogen contents, normalizing condition and TMCP process on the mechanical properties of low-activation 9Cr-2W-0.2V-Ta steels for fusion application, Journal of Nuclear Materials. 258-263 (1998) 1153-1157.

23. S. Chen, L. Rong, Effect of silicon on the microstructure and mechanical properties of reduced activation ferritic/martensitic steel, Journal of Nuclear Materials. 459 (2015) 13-19.

24. M. Tamura, H. Hayakawa, M. Tanimura, A. Hishinuma, T. Kondo, Development of potential low activation ferritic and austenitic steels, Journal of Nuclear Materials. 141-143 (1986) 1067-1073.

25. B. van der Schaaf, D.S. Gelles, S. Jitsukawa, A. Kimura, R.L. Klueh, A. Möslang, G.R. Odette, Progress and critical issues of reduced activation ferritic/martensitic steel development, Journal of Nuclear Materials. 283-287 (2000) 52-59.

26. A. Kohyama, A. Hishinuma, D.S. Gelles, R.L. Klueh, W. Dietz, K. Ehrlich, Low-activation ferritic and martensitic steels for fusion application, Journal of Nuclear Materials. 233-237 (1996) 138-147.

27. R.L. Klueh, D.J. Alexander, M. Rieth, The effect of tantalum on the mechanical properties of a 9Cr-2W-0.25V-0.07Ta-0.1C steel, Journal of Nuclear Materials. 273 (1999) 146-154.

28. A.V. Panin, V.M. Chernov, M.V. Leontieva-Smirnova, E.A. Melnikova, Strengthening of the RAFMS RUSFER-EK181 through nanostructuring surface layers, Journal of Nuclear Materials. 386-388 (2009) 466-470.

29. J. Yu, Q. Huang, F. Wan, Research and development on the China low activation martensitic steel (CLAM), Journal of Nuclear Materials. 367-370 (2007) 97-101.

30. A. Kimura, Current status of reduced-activation ferritic/martensitic steels R&D for fusion energy, Materials Transactions. 46 (2005) 394-404.

31. X. Mao, T.K. Kim, S.S. Kim, Y.S. Han, K.H. Oh, J. Jang, Crystallographic relationship of YTaO4 particles with matrix in Ta-containing 12Cr ODS steel, Journal of Nuclear Materials. 461 (2015) 329–335.

32. H.L. Ding, R. Gao, T. Zhang, X.P. Wang, Q.F. Fang, C.S. Liu, Annealing effect on the microstructure and magnetic properties of 14%Cr-ODS ferritic steel, Fusion Engineering and Design. 100 (2015) 371–377.

33. C. Lu, Z. Lu, C. Liu, Microstructure of nano-structured ODS CLAM steel by mechanical alloying and hot isostatic pressing, Journal of Nuclear Materials. 442 (2013) S148-S152.

34. J. Knaster, A. Moeslang, T. Muroga, Materials research for fusion, Nature Physics. 12 (2016) 424-434.

35. R.L. Klueh, J.P. Shingledecker, R.W. Swindeman, D.T. Hoelzer, Oxide dispersion-strengthened steels: A comparison of some commercial and experimental alloys, Journal of Nuclear Materials. 341 (2005) 103-114.

36. M. Bruchhausen, K. Turba, F. de Haan, P. Hähner, T. Austin, Y. de Carlan, Characterization of a 14Cr ODS steel by means of small punch and uniaxial testing with regard to creep and fatigue at elevated temperatures, Journal of Nuclear Materials. 444 (2014) 283-291.

37. T. Balakrishna Bhat, V.S. Arunachalam, Strengthening mechanisms in alloys, Prec. Indian Acad. Sci. (Engineering. Sciences). 3 (1980) 275-296.

38. R.B. Ellis, Dispersion strengthening of metals, American Scientist. 52 (1964) 476-487.

39. G.E. Dieter, Mechanical metallurgy, McGraw-Hill Book Company. (1988).

40. R.E. Smallman, A.H.W. Ngan, Physical metallurgy and advanced materials, 7th edition, Elsevier. (2007).

41. R.E. Smallman, R.J. Bishop, Modern physical metallurgy and materials engineering, 6th edition, Reed Educational and Professional Publishing Ltd. (1999).

42. R. Abbaschian, L. Abbaschian, R.E. Reed-Hill, Physical metallurgy principles, 4th edition, Cengage Learning. (2009).

43. L. Raman, K. Gothandapani, B. S. Murty, Austenity oxide dispersion strengthened steels: a review, Defence Science Journal. 66 (2016) 316-322.

44. C. Capdevila, H.K.D.H. Bhadeshia, Manufacturing and microstructural evolution of mechanuically alloyed oxide dispersion strengthened superalloys, Advanced Engineering Materials. 3 (2001) 647-656.

45. J.S. Benjamin, Dispersion strengthened superalloys by mechanical alloying, Metallurgical Transactions. 1 (1970) 2943-2951.

46. N.L. Loh, K.Y. Sia, An overview of hot isostatic pressing, Journal of Materials Processing Technology. 30 (1992) 45-65.

47. Ch.Ch. Eiselt, M. Klimenkov, R. Lindau, A. Möslang, G.R. Odette, T. Yamamoto, D. Gragg, Tensile and fracture toughness properties of the nanostructured oxide dispersion strengthened ferritic alloy 13Cr–1W–0.3Ti–0.3Y_2O_3, Journal of Nuclear Materials. 417 (2011) 193-196.

48. M.A. Auger, T. Leguey, A. Munoz, M.A. Monge, V. de Castro, P. Fernandenz, G. Garces, R. Pareja, Microstructure and mechanical properties of ultrafine-grained Fe–14Cr and ODS Fe–14Cr model alloys, Journal of Nuclear Materials. 417 (2011) 213-216.

49. V. de Castro, T. Leguey, A. Munoz, M.A. Monge, R. Pareja, E.A. Marquis, S. Lozano-Perez, M.L. Jenkins, Microstructural characterization of Y_2O_3 ODS–Fe–Cr model alloys, Journal of Nuclear Materials. 386-388 (2009) 449-452.

50. J.R. Rieken, I.E. Anderson, M.J. Kramer, G.R. Odette, E. Stergar, E. Haney, Reactive gas atomization processing for Fe-based ODS alloys, Journal of Nuclear Materials. 428 (2012) 65–75.

51. R. Xie, Z. Lu, C. Lu, C. Liu, Effects of mechanical alloying time on microstructure and properties of 9Cr–ODS steels, Journal of Nuclear Materials. 455 (2014) 554-560.

52. L. Guo, C. Jia, B. Hu, H. Li, Microstructure and mechanical properties of an oxide dispersion strengthened ferritic steel by a new fabrication route, Materials Science and Engineering A. 527 (2010) 5220–5224.

53. Q. Sun, T. Zhang, X. Wang,Q. Fang,J. Hu, C. Liu, Synthesis and characterization of oxide dispersion strengthened ferritic steel via a sol-gel route, Plasma Science and Technology. 14 (2012) 661-664.

54. C. Chen, Z. Guo, J. Luo, W. Yang, J. Hao, J. Yang, Self-propagating combustion synthesis and characterization of ODS Fe-base superalloy powders, Materials Science Forum. 747-748 (2013) 641-646.

55. M. Sarma, I. Grants, I. Kaldre, A. Bojarevics, G. Gerbeth, Casting technology for ODS steels – dispersion of nanoparticles in liquid metals, IOP Conf. Series: Materials Science and Engineering. 228 (2017).

56. C.H. Konrad, R. Völkl, U. Glatzel, Determination of oxygen diffusion along nickel/zirconia phase boundaries by internal oxidation, Oxid Met. 77 (2012) 149–165.

57. F.H. Stott, Y. Shida, D.P. Whittle, G.C. Wood, B.D. Bastow, The morphological and structural development ot internal oxides in nickel-aluminum alloys at high temperatures, Oxidation of Metals. 18 (1982) 127-146.

58. A. Madeshia, An amendment to the classical model of internal oxidation: Model-inherent transition characteristics, Corrosion Science. 68 (2013) 111-118.

59. C. Wagner, Reaktionstypen bei der Oxidation von Legierungen, Zeitschrift für Elektrochemie. 63 (1959) 772–782.

60. R.A. Rapp, Kinetics, microstructures and mechanism of internal oxidation - its effect and prevention in high temperature alloy oxidation, Corrosion. 21 (1965) 382-401.

61. C. Xu, D. Yi, Y. Jiang, C. Wu, H. Zhang, S. Peng, The kinetics and interface microstructure evolution in the internal oxidation of Ag–3at.%Sn alloy, Corrosion Science. 94 (2015) 392–400.

62. R. Mertel, C.H. Konrad, M. Terock, R. Völkl, U. Glatzel, Internal oxidation of ternary alloys forming a high oxygen conductive oxide, Oxid Met. 86 (2016) 193–203.

63. A.T. Allen, D.L. Douglass, Internal-nitriding behavior of Ni-V and Ni-3Nb alloys, Oxidation of Metals. 51 (1999) 1-22.

64. H.-J. Christ, S.-Y. Chang, U. Krupp, Thermodynamic characteristics and numerical modelling of internal nitridation of nickel base alloys, Materials and Corrosion. 54 (2003) 887-984.

65. M. Udyavar, D.J. Young, Precipitate morphologies and growth kinetics in the internal carburisation and nitridation of Fe-Ni-Cr alloys, Corrosion Science. 42 (2000) 861-883.

66. C.P. Wu, D.Q. Yi, J. Li, L.R. Xiao, B. Wang, F. Zheng, Investigation on microstructure and performance of Ag/ZnO contact material, Journal of Alloys and Compounds. 457 (2008) 565–570.

67. C. Xu, D. Yi, C. Wu, H. Liu, W. Li, Microstructures and properties of silver-based contact material fabricated by hot extrusion of internal oxidized Ag–Sn–Sb alloy powders, Materials Science and Engineering A. 538 (2012) 202-209.

68. E. Romhanji, M. Filipovic, Z. Kamberovic, Kinetics of internal oxidation in Ag-6Sn-2In-1Te-0.2Ni and Ag-6Sn-0.6Cu-1Bi-0.2Ni type alloys, Metals and Materials International. 18 (2012) 171-176.

69. J.-K. Kim, D.-J. Jang, G.-B. Kwon, D.-H. Cho, S.-Y. Um, J.-K. Kim, T.-W. Nam, The effects of Te and misch metal additions on the microstructure and properties of rapidly solidified Ag-Sn-In alloy for electrical contact applications, Metals and Materials International. 14 (2008) 403-409.

70. L. Ruihua, S. Kexing, J. Shuguo, X. Xiaofeng, G. Jianxin, G. Xiuhua, Morphology and frictional characteristics under electrical currents of Al2O3/Cu composites prepared by internal oxidation, Chinese Journal of Aeronautics. 21 (2008) 281-288.

71. L. Guobin, S. Jibing, Guo Quanmei, Wang Ru, Fabrication of the nanometer Al_2O_3/Cu composite by internal oxidation, Journal of Materials Processing Technology. 170 (2005) 336-340.

72. F. Ren, A. Zhi, D. Zhang, B. Tian, A.A. Volinsky, X. Shen, Preparation of Cu–Al2O3 bulk nano-composites by combining Cu–Al alloy sheets internal oxidation with hot extrusion, Journal of Alloys and Compounds. 633 (2015) 323-328.

73. J.H. Schneibel, S. Shim, Nano-scale oxide dispersoids by internal oxidation of Fe–Ti–Y intermetallics, Materials Science and Engineering A. 488 (2008) 134-138.

74. J.R. Rieken, I.E. Anderson, M.J. Kramer, G.R. Odette, E. Stergar, E. Haney, Reactive gas atomization processing for Fe-based ODS alloys, Journal of Nuclear Materials. 428 (2012) 65-67.

75. H. Tang, X. Chen, M. Chen, L.i Zuo, B. Hou, Z. Wang, Microstructure and mechanical property of in-situ nano-particle strenghened ferrite steel by novel internal oxidation, Materials Science & Engineering A. 609 (2014) 293-299.

76. S.J. Kachur, B.A. Webler, Effect of microstructure on the internal oxidation of two-phase Fe–Y alloys, Oxidation of Metals. 85 (2016) 343–355.

77. M.A. Moghadasi, M. Nili Ahmadabadi, F. Forghani, H.S. Kim, Development of an oxidedispersion-strengthened steel by introducing oxygen carrier compound into the melt aided by a general thermodynamic model, Scientific Reports. 8 (2016) 1-9.

78. W. Wang, E. Wu, S. Liu, Y. Wang and Y. Li, Segregation and precipitation formation for in situ oxidised 9Cr steel powder, Materials Science and Technology. 33 (2017) 104-113.

79. M. Klimenkov, R. Lindau, A. Möslang, TEM study of internal oxidation in an ODS-Eurofer alloy, Journal of Nuclear Materials. 386-388 (2009) 557–560.

80. H.L. Lukas, S.G. Fries, Computational thermodynamics: the CALPHAD method. Cambrdige University Press. (2007).

81. G. Eriksson, Thermodynamic studies of high temperature equilibria. III. SOLGAS, a computer program for calculating the composition and heat condition of an equilibrium mixture, Acta Chem. Scand. 25 (1971) 2651-2658.

82. M. Hillert, Some viewpoints on the use of a computer for calculating phase diagrams, Physica B+C. 103 (1981) 31-40.

83. C.W. Bale, P. Chartrand, S.A. Degterov, G. Eriksson, K. Hack, R. Ben Mahfoud, J. Melanqon, A.D. Pelton, S. Petersen, FactSage thermochemical software and databases, CALPHAD. 26 (2002) 189-228.

84. S.-L. Chen, S. Daniel, F. Zhang, Y.A. Chang, X.-Y. Yan, F.-Y. Xie, R. Schmid-Fetzer, W.A. Oates, The Pandat software package and its applications, CALPHAD. 26 (2002) 175-188.

85. J.O. Andersson, T. Helander, L. Höglund, P. Shi, B. Sundman, Thermo-Calc and DICTRA, computational tools for materials science, CALPHAD. 26 (2002) 273-312.

86. B. Sundamn, B. Jansson, J.O. Andersson, The Thermo-Calc databank system, CALPHAD. 9 (1985) 153-190.

87. D.R. Gaskell, Introduction to the thermodynamics of materials, 4th Edition, Taylor and Francis. (2003).

88. [TCFE7], TCS Steels/Fe-Alloys Database v7.0, Thermo-Calc software AB. (2012).

89. L. Kjellqvist, M. Selleby, B. Sundman, Thermodynamic modelling of the Cr–Fe–Ni–O system, CALPHAD. 32 (2008) 577–592.

90. [TCBIN], TC Binary Solutions Database v1.1, Thermo-Calc software AB. (2011).

91. V. Swamy, H.J. Seifert, F. Aldinger, Thermodynamic properties of Y_2O_3 phases and the yttrium–oxygen phase diagram, Journal of Alloys and Compounds. 269 (1998) 201-207.

92. Y. Yang, H. Mao, M. Selleby, Thermodynamic assessment of the V–O system, CALPHAD. 51 (2015) 144–160.

93. [MOBFE2] TCS Steels/Fe-Alloys Mobility Database v2, Thermo-Calc software AB. (2012).

94. E. Airiskallio, E. Nurmi, M.H. Heinonen, I.J. Väyrynen, K. Kokko, M. Ropo,M.P.J. Punkkinen, H. Pitkänen, M. Alatalo, J. Kollár, B. Johansson, L. Vitos, High temperature oxidation of Fe–Al and Fe–Cr–Al alloys: The role of Cr as a chemically active element, Corrosion Science. 52 (2010) 3394-3404.

95. B. Lesage, L. Marechal, A.-M. Huntz, R. Molins, Aluminium depletion in FeCrAl alloys during oxidation, Defect and Diffusion Forum. 194-199 (2001) 1707-1712.

96. B.A. Pint, I.G. Wright, Oxidation behavior of ODS Fe–Cr alloys, Oxidation of Metals. 63 (2005) 193-213.

97. H. Götlind, F. Liu, J.-E. Svensson, M. Halvarsson, L.-G. Johansson, The effect of water vapor on the initial stages of oxidation of the FeCrAl alloy Kanthal AF at 900 °C, Oxidation of Metals. 67 (2007) 251-266.

98. J. Jedlinski, Application of O2 exposure–based approach to study the failure mechanisms of oxide scales on alumina formers, Materials Science Forum. 513 (2006) 149-164.

99 X. Hou, R.S. Amais, B.T. Jones, G.L. Donati, Inductively coupled plasma optical emission spectrometry, in Encyclopedia of Analytical Chemistry. Editor: R.A. Meyers. (2016) 1-25.

100. W. Gruner, Determination of oxygen in oxides by carrier gas hot extraction analysis with simultaneous COx detection, Fresenius J. Anal Chem. 365 (1999) 597-603.

101. A. Reimschuessel, LXVI. Scanning electron microscopy-part I, Journal of Chemical Education. 49 (1972) A413-A419.

102. M. Abd Mutalib, M.A. Rahman, M.H.D. Othman, A.F. Ismail, J. Jaafar, Scanning Electron Microscopy (SEM) and Energy-Dispersive X-Ray (EDX) Spectroscopy, Membrance characterization. (2017) 161-179.

103. D.B. Williams, C.B. Carter, Transmission electron microscopy, a textbook for materials science, Springer. (2009).

104. C.Y. Tang, Z. Yang, Transmission electron microscopy (TEM), Membrance Characterization. (2017) 145-159.

105. D. Stojakovic, Electron backscatter diffraction in materials characterization, Processing and Application of Ceramics. 6 (2012) 1-13.

106. T. Maitland, S. Sitzman, Backscattering detector and ebsd in nanomaterials characterization, in scanning microscopy for nanotechnology, Z. L. Wang, W. Zhou, Springer. (2006).

107. F. Klocke, L. Hensgen, A. Klink, J. Mayer, A.Schwedt, EBSD-Analysis of Flexure Hinges Surface Integrity Evolution via Wire-EDM Main and Trim Cut Technologies, Procedia CIRP. 13 (2014) 237-242.

108. D.A. Porter, K.E. Easterling, Phase transformations in metals and alloys. (1992) Chapman & Hall Publishing.

109. F.G. Wilson, T. Gladman, Aluminium nitride in steel, International Materials Reviews. 33 (1988) 221-286.

110. M.P. Brady, Y. Yamamoto, M.L. Santella, P.J. Maziasz, B.A. Pint, C.T. Liu, Z.P. Lu, H. Bei, The development of alumina-forming austenitic stainless steels for high-temperature structural use, J. Minerals, Metals and Materials Society. 60 (2008).

111. T. Jozaghi, C. Wang, R. Arroyave, I. Karaman, Design of alumina-forming austenitic stainless steel using genetic algorithms, Materials and Design. 186 (2020).

112. R. Hazen, R. Jeanloz, Wüstite ($Fe_{1-x}O$): a review of its defect structure and physical properties, Reviews of Geo. and Space Physics. 22 (1984) 37-46.

113. J. Zurek, G.H. Meier, E. Wessel, L. Singheiser, W. J. Quadakkers, Temperature and gas composition dependence of internal oxidation kinetics of an Fe–10%Cr alloy in water vapour containing environments, Materials and Corrosion. 62 (2011) 504-513.

114. K. Hirose, G. Morard, R. Sinmyo, K. Umemoto, J. Hernlund, G. Helffrich, S. Labrosse, Crystallization of silicon dioxide and compositional evolution of the Earth’s core, Nature. 543 (2017) 99-102.

115. S.S. Shibaev, K.V. Grigorovich, Solubility of oxygen in iron-silicon melts, Journal of Physics: Conference Series. 98 (2008).

116. M.T. Hepworth, R.P. Smith, E.T. Turkdogan, Permeability, Solubility, and diffusivity of oxygen in bcc iron, Trans. AIME. 236 (1966) 1278-1283.

117. J. Takada, M. Adachi, Determination of diffusion coefficient of oxygen in α-iron from internal oxydation measurements in Fe-Si alloys, Journal of Materials Science. 21 (1986) 2133-2137.

118. J. Takada, S. Yamamoto, M. Adachi, Diffusion coefficient of oxygen in α-iron determined by internal oxidation technique, Zeitschrift für Metallkunde. 77 (1986) 6-11.

119. P. Franke, Karlsruhe Institute of Technology (KIT), A part of personal communication, Karlsruhe (2018).

120. J.L. Meijering, On the diffusion of oxygen through solid iron, Acta Metallurgica. 3 (1955) 157-162.

121. A. Prillieux, D. Jullian, J. Zhang, D. Monceau, D. J. Young, Internal oxidation in dry and wet conditions for oxygen permeability of Fe–Ni Alloys at 1150 and 1100 °C, Oxidation of Metals. 87 (2017) 273-283.

122. S. Nasrazadani, S. Hassani, Modern analytical techniques in failure analysis of aerospace, chemical, and oil and gas industries, in Handbook of materials failure analysis with case studies from the oil and gas industry. A.S.H. Makhlouf, M. Aliofkhazraei (2015).

123. C.A. Schneider, W.S. Rasband, K.W.Eliceiri, NIH images to ImageJ: 25 years of imaging analysis. Nature Methods. 9 (2012) 671-675.

124. T.W. Ridler, S. Calvard, Picture thresholding using an iterative selection method, IEEE Transactions on Systems, Man, and Cybernetics. 8 (1978) 630 - 632.

125. J.N. Kapur, P.K. Sahoo, A.K.C. Wong, A new method for gray-level picture thresholding using the entropy of the histogram, Computer Vision, Graphics, and Image Processing. 29 (1985) 273-285.

126. C.H. Li, P.K.S. Tam, An iterative algorithm for minimum cross entropy thresholding, Pattern Recognition Letters. 19 (1998) 771-776.

127. G.W. Zack, W.E. Rogers, S.A. Latt, Automatic measurement of sister chromatid exchange frequency, Journal of Histochemistry & Cytochemistry. 25 (1977) 741-753.

128. T. Heumann, H. Mehrer, Diffusion in Metallen, Springer Berlin. (1992).

129. H. Oikawa, Lattice diffusion in iron - a review, Tetsu-to-Hagane. 68 (1982) 1489-1497.

130. P. Saltykov, O. Fabrichnaya, J. Golczewski, F. Aldinger, Thermodynamic modelling of oxidation of Al-Cr-Ni alloys, J. Alloys Compd. 381 (2004) 99-113.

131. K. Atarashiya, R. Nagasaki, K. Nishida, Interdiffusion in Al_2O_3-Cr_2O_3 Quasi-binary System, Journal of Japan Institute of Metals. 51 (1987) 1018-10222.

132. D.P. Field, Recent advances in the application of orientation imaging, Ultramicroscopy. 67 (1997) 1-9.

133. S. Kardellass, C. Servant, N. Selhaoui, A. Iddaoudi, M. Ait Amar, L. Bouirden, A thermodynamic assessment of the iron–yttrium system, Journal of Alloys and Compounds. 583 (2014) 598-606.

134. L. Li, Z. Xing, Solubilities of Ce, Nd and Y in α-Fe, Acta Metall. Sin. 29 (1993) A136-A141.

135. M. Klimiankou, R. Lindau, A. Möslang, J. Schröder, TEM study of PM2000 steel, Powder Metallurgy. 48 (2005) 277-287.

136. G. Böhm, M. Kahlweit, Über die innere Oxidation von Metallegierungen, Acta Metallurgica. 12 (1964) 641-648.

137. T. Gräning, M. Rieth, J. Hoffmann, A. Möslang, Production, microstructure and mechanical properties of two different austenitic ODS steels, Journal of Nuclear Materials. 487 (2017) 348-361.

138. D. Kumar, U. Prakash, V.V. Dabhade, K. Laha, T. Sakthivel, Influence of yttria on oxide dispersion strengthened (ODS) ferritic steel, Material Today: Proceedings. 5 (2018) 3909-3913.

139. J. Hoffmann, M. Rieth, R. Lindau, M. Klimenkov, A. Möslang, H. Ricardo, Z. Sandim, Investigation on different oxides as candidates for nano-sized ODS particles in reduced-activation ferritic (RAF) steels, Journal of Nuclear Materials. 442 (2013) 444-448.

140. M. Gong, Z. Zhou, H. Hu, G. Zhang, S. Li, M. Wang, Effects of aluminum on microstructure and mechanical behavior of 14Cr–ODS steels, Journal of Nuclear Materials. 462 (2015) 502-507.

141. X. Hu, L. Chen, C. Zhan, K. Xu, M. Lou, K. Chang, Thermodynamic assessment of the Fe–Ni–Rh–Ti system, CALPHAD. 76 (2022).

142. I. Kaldre, A. Bojarevics, I. Grants, T. Beinerts, M. Kalvans,M. Milgravis, G. Gerbeth, Nanoparticle dispersion in liquid metals by electromagnetically induced acoustic cavitation, Acta Materialia. 118 (2016) 253-259.

143. G. Cao, H. Konishi, X. Li, Recent developments on ultrasonic cavitation based solidification processing of bulk magnesium nanocomposites, International Journal of Metalcasting. 2 (2008) 57-65.

144. I. Grants, G. Gerbeth, A. Bojarevics, Contactless magnetic excitation of acoustic cavitation in liquid metals, Journal of Applied Physics. 117 (2015).

145. X. Li, Y. Yang, D. Weiss, Theoretical and experimental study on ultrasonic dispersion of nanoparticles for strengthening cast aluminum alloy A356, Metallurgical Science and Technology. 26 (2008) 12-20.

146. M. Sarma, S. Miran, I. Grants, G. Gerbeth, Dispersion of nanoparticles in steel melt by superimposed steady and alternating magnetic fields, in International conference on heating by electromagnetic sources. Padova, Italy (2016).